



HAL
open science

Structure of iso-scalar sets

M. Gauding, F. Thiesset, E. Varea, Luminita Danaila

► **To cite this version:**

M. Gauding, F. Thiesset, E. Varea, Luminita Danaila. Structure of iso-scalar sets. *Journal of Fluid Mechanics*, 2022, 942, pp.A14. 10.1017/jfm.2022.367 . hal-03670518

HAL Id: hal-03670518

<https://hal.science/hal-03670518>

Submitted on 17 May 2022

HAL is a multi-disciplinary open access archive for the deposit and dissemination of scientific research documents, whether they are published or not. The documents may come from teaching and research institutions in France or abroad, or from public or private research centers.

L'archive ouverte pluridisciplinaire **HAL**, est destinée au dépôt et à la diffusion de documents scientifiques de niveau recherche, publiés ou non, émanant des établissements d'enseignement et de recherche français ou étrangers, des laboratoires publics ou privés.

Banner appropriate to article type will appear here in typeset article

Structure of iso-scalar sets

M. Gauding¹, F. Thiesset^{1†}, E. Varea¹, L. Danaila²

¹CORIA, UMR 6614, CNRS, Normandy Univ., UNIROUEN, INSA Rouen, 76000 Rouen, France

²M2C, UMR 6143, CNRS, Normandy Univ., UNIROUEN, 76000 Rouen, France

(Received xx; revised xx; accepted xx)

An analytical framework is proposed to explore the structure and kinematics of iso-scalar fields. It is based on a two-point statistical analysis of the phase indicator field which is used to track a given iso-scalar volume. The displacement speed of the iso-surface, i.e. the interface velocity relative to the fluid velocity, is explicitly accounted for, thereby generalizing previous two-point equations dedicated to the phase indicator in two-phase flows. Although this framework applies to many transported quantities, we here focus on passive scalar mixing. Particular attention is paid on the effect of Reynolds (the Taylor based Reynolds number is varied from 88 to 530) and Schmidt numbers (in the range 0.1 to 1), together with the influence of flow and scalar forcing. It is first found that diffusion in the iso-surface tangential direction is predominant, emphasizing the primordial influence of curvature on the displacement speed. Second, the appropriate normalizing scales for the two-point statistics at either large, intermediate and small scales are revealed and appear to be related to the radius of gyration, the surface density and the standard deviation of mean curvature, respectively. Third, the onset of an intermediate 'scaling range' for the two-point statistics of the phase indicator at sufficiently large Reynolds numbers is observed. The scaling exponent complies with a fractal dimension of $8/3$. A scaling range is also observed for the transfer of iso-scalar fields in scale-space whose exponent can be estimated by simple scaling arguments and a recent closure of the Corrsin equation. Fourth, the effects of Reynolds and Schmidt numbers together with flow or scalar forcing on the different terms of the two-point budget are highlighted.

Key words:

1. Introduction

There exist a large variety of physical situations in which a description in terms of curved surfaces or interfaces instinctively emerges. Leaving aside some fields of physics such as soft-matter physics (De Gennes *et al.* 2013), heterogeneous materials (Torquato 2002) or biological/chemical-physics (Garcia-Ruiz *et al.* 2012),

† Email address for correspondence: thiesset@coria.fr

35 this concept applies naturally to fluid flows. A two-phase flow is the first case
 36 that comes to mind since the surface formed by the liquid-gas interface can
 37 even be observed with the naked eye (Dumouchel 2008). A description in terms
 38 of curved surfaces is also widely encountered in reacting flows (diffusion and
 39 premixed flames), where the chemical reactions occur in thin layers. This has
 40 inspired the flamelet model (Peters 1988) which considers reacting zones as a
 41 collection of thin layers, whose inner structure is identical to a laminar flame,
 42 propagating normal to themselves in the direction of the unburned turbulent
 43 mixture. In single-phase non-reacting flows, there are situations where a thin
 44 interface separates some zones of irrotational motion to some zones of strong
 45 vortical intensity (da Silva *et al.* 2014). This layer, which can be observed in
 46 many archetypal flow configurations such as wakes, jets or boundary layers, is
 47 referred to as the *turbulent/non-turbulent interface*, abbreviated TNTI. Mixing
 48 can also be treated using some geometric measures of iso-scalar surfaces (Catrakis
 49 & Dimotakis 1996; Dimotakis & Catrakis 1999). There are also a variety of
 50 natural situations, related to e.g. clouds and precipitations, dunes, coasts erosion,
 51 ocean mixing, ice melting, aquifers which can properly be described through a
 52 morphological analysis of moving interfaces.

53 For all such situations, the macroscale features of the interface are of great
 54 interest. In two-phase flows, the surface area or surface density (surface area per
 55 unit volume) of the liquid-gas interface is generally the parameter one seeks to
 56 optimize by resorting to the creation of a spray (Ashgriz 2011). This parameter
 57 also controls the evaporation rate in flows with phase change (Lebas *et al.* 2009;
 58 Jay *et al.* 2006). It is also a key parameter in climate change studies for which
 59 the processes taking place at the air-sea interface are primordial (Liss & Johnson
 60 2014). In premixed flames, the flame surface area is an important parameter
 61 as it appears in the expression of the volume integrated burning rate and heat
 62 release (e.g. Trouvé & Poinso 1994). For the TNTI, the surface area allows the
 63 rate of entrainment of irrotational zones into the turbulent flow to be estimated
 64 (Sreenivasan *et al.* 1989; Krug *et al.* 2015).

65 The versatility of the notion of curved surface finds its foundation on some
 66 mathematical grounds. Given any field variable ξ (e.g. temperature, concen-
 67 tration, enstrophy, etc) that varies in space, one can take any iso-value ξ_0 to
 68 define an interface which separates the regions where $\xi(\mathbf{x}) > \xi_0$ from the regions
 69 where $\xi(\mathbf{x}) < \xi_0$. The kinematic equations for both the interface position and
 70 its geometrical features (surface density, curvatures) are known (Pope 1988;
 71 Drew 1990; Vassilicos & Hunt 1996) thereby embedding in a single mathematical
 72 framework single- or two-phase, reacting or non-reacting flows, in presence or
 73 absence of phase change.

74 The wrinkling of the interface is related to intrinsic instabilities and to in-
 75 homogeneities (specifically the turbulence) of the carrier environment which
 76 itself reveals some multi-scale fluctuations. This means, not only the macroscale
 77 features (i.e. measured at scales larger than a typical integral correlation length-
 78 scale) are important, but also the microstructural characteristics (measured at
 79 a scale r) are worth being explored. In this respect, it is now well known that
 80 interfaces that one may find in turbulence and turbulent mixing (Sreenivasan &
 81 Meneveau 1986; Sreenivasan *et al.* 1989; Catrakis & Dimotakis 1996; de Silva *et al.*
 82 2013), turbulent premixed flames (Gouldin 1987; Gouldin *et al.* 1989), two-phase
 83 flows (Le Moyne *et al.* 2008; Dumouchel & Grout 2009; Grout *et al.* 2007), and
 84 material lines evolving in turbulent flows (Villermaux & Gagne 1994) reveal some

85 "fractal facets". The fractal dimension of interfaces was predicted analytically
86 (Mandelbrot 1975; Constantin *et al.* 1991; Grossmann & Lohse 1994; Iyer *et al.*
87 2020). For instance, Mandelbrot (1975) proved that the fractal dimension of iso-
88 scalars is 2.5 for Burgers turbulence and $8/3$ for Kolmogorov turbulence. Using
89 tools from geometric measure theory, Constantin *et al.* (1991) showed that the
90 fractal dimension of iso-scalars might evolve between $7/3$ near the TNTI to $8/3$
91 in fully turbulent regions. Later, Constantin (1994*b,a*) showed that a value of
92 $8/3$ holds for iso-scalars in the limit of small molecular diffusivities (high Schmidt
93 numbers) while flame fronts exhibit a fractal dimension of $7/3$. The dimensional
94 analysis of Hawkes *et al.* (2012); Thiesset *et al.* (2016*a*) showed that premixed
95 flame fronts have a fractal dimension of $7/3$ ($8/3$) in low (high) Karlovitz number
96 combustion regimes. The Prandtl (or Schmidt) number dependence of the fractal
97 dimension of iso-scalars is predicted by Grossmann & Lohse (1994). The fractal
98 dimension of clouds were also investigated (Lovejoy 1982; Hentschel & Procaccia
99 1984). Using numerical data of scalar mixing with an imposed mean gradient
100 at relatively high Reynolds numbers, Iyer *et al.* (2020) recently showed that the
101 fractal dimension is 2 ($8/3$) for scalar iso-values far away from (close to) the mean.
102 Note that we omitted here the possibility that the fractal dimension might be
103 scale-dependent as argued in the review by Dimotakis & Catrakis (1999). Note
104 also that what is here simply referred to as a fractal dimension may recover
105 different mathematical definitions (Hausdorff dimension, Kolmogorov capacity
106 (Vassilicos & Hunt 1991; Vassilicos 1992)).

107 Characterizing and predicting the microscopic scale-dependent features (= the
108 microstructure) of interfaces requires the coupling between the interface and the
109 surrounding medium to be well understood. In this goal, one needs to identify
110 the range of scales over which some characteristic physical parameters (e.g.
111 surface tension, fluid viscosity, scalar diffusivity, etc) or some physical processes
112 (turbulent straining, production by mean scalar gradient or interface reactivity,
113 etc), have an influence. It is also worth drawing the connections between the
114 typical length-scales of the dynamical or scalar field (integral, Taylor, Corrsin,
115 Kolmogorov, Batchelor, Obukhov length-scales) to those of the interface (inner
116 and outer cutoff scales, radius of curvature, surface density length-scale). All
117 these questions necessitate a scale-by-scale description of the processes at play
118 in the kinematic evolution of contorted iso-surfaces or iso-volumes. To the best
119 of our knowledge, there does not exist such a theoretical framework that may
120 be valid at all scales, irrespectively of the flow configuration and flow regime.
121 The present study is an attempt to fill this gap. We propose an analytical
122 description that relies on a two-point statistical analysis (correlation and/or
123 structure functions) of the phase indicator function. The latter field variable
124 is used as a 'marker' or 'localizer' of the fluid iso-volume formed by a given
125 iso-scalar value. Such two-point statistics are employed in different branches
126 of physics, generally to gain information about the morphological content (the
127 microstructure) of heterogeneous materials (Adler *et al.* 1990; Torquato 2002;
128 Teubner 1990; Kirste & Porod 1962; Frisch & Stillinger 1963; Berryman 1987)
129 or fractal aggregates (Sorensen 2001; Morán *et al.* 2019). In fluid mechanics,
130 there are only few papers dealing with these aspects (Hentschel & Procaccia
131 1984; Vassilicos & Hunt 1991; Vassilicos 1992; Vassilicos & Hunt 1996; Lu &
132 Tryggvason 2018, 2019; Elsas *et al.* 2018).

133 Here, the main originality of the present work is that this morphological
134 descriptor is supplemented by an exact transport equation which allows the

135 different physical process acting on the iso-scalar volumes to be characterized. It
 136 generalizes the equation proposed by Thiesset *et al.* (2020, 2021) firstly dedicated
 137 to two-phase flows, to cases where the interface possesses an intrinsic displacement
 138 speed (as for premixed flames or diffusive scalars). The machinery for obtaining
 139 two-point statistical equations is the same as the one used to derive the scale-by-
 140 scale budgets of the dynamical or scalar field (see Hill 2002; Danaila *et al.* 2004,
 141 among others). We will also resort to some analytical studies emanating from the
 142 fields of heterogeneous materials (Adler *et al.* 1990; Torquato 2002; Teubner 1990;
 143 Kirste & Prood 1962; Frisch & Stillinger 1963; Berryman 1987) and aggregates
 144 (Sorensen 2001; Morán *et al.* 2019) allowing the phase indicator structure function
 145 to be related to some integral geometric measures of the interface (surface den-
 146 sity, mean and Gaussian curvatures) and some fractal characteristics. Although
 147 the proposed theory may apply to very different situations, we focus here on
 148 passive scalar mixing which is explored using Direct Numerical Simulation data
 149 covering a wide range of Reynolds and Schmidt numbers. By doing so, we expect
 150 emphasizing the key physics that ought to be accounted for e.g. a geometrical
 151 closure to the turbulent scalar flux in the equation for the mean scalar.

152 The present study has four objectives. Firstly, it aims at generalizing the
 153 equations firstly derived by Thiesset *et al.* (2020, 2021) to the case of diffusive
 154 scalars. The new set of equations reveals the importance of the interface displace-
 155 ment speed which embeds different physics depending on the flow configuration.
 156 The second objective of our work is to characterize the influence of some non-
 157 dimensional numbers (Reynolds and Schmidt numbers) and some geometrical
 158 features (e.g. the mean curvature) on the different components of the interface
 159 displacement speed. Thirdly, it aims at identifying the characteristic length-scales,
 160 asymptotic scaling and normalizing quantities of the phase indicator structure
 161 functions. Fourthly, it intends to explore the effect of Reynolds and Schmidt
 162 numbers together with other effects (decay, mean scalar/velocity gradient) on the
 163 different processes revealed by the scale-by-scale budgets of the phase indicator
 164 field.

165 The paper is organized as follows. The equations for the transport of the
 166 iso-scalar surface and the corresponding phase indicator structure functions are
 167 derived in section 2. We also derive the asymptotic limits at either large or small
 168 scales revealing the link between two-point statistics of the phase indicator and
 169 some integral geometric measures of the iso-surface (volumes, surface area, mean
 170 and Gaussian curvature). The numerical database and post-processing procedures
 171 are portrayed in section 3. Results are presented in 4. Technicalities are gathered
 172 in the Appendix. Conclusions are drawn in a last section.

173 2. Analytical considerations

174 2.1. Kinematics of iso-scalar excursion sets

175 Consider the scalar field $\xi(\mathbf{x}, t)$ whose transport equation is

$$176 \quad \partial_t \xi + \nabla_{\mathbf{x}} \cdot \mathbf{u} \xi = \nabla_{\mathbf{x}} \cdot D \nabla_{\mathbf{x}} \xi + \Xi + \dot{\omega}_{\xi}. \quad (2.1)$$

177 Here, \mathbf{u} is the fluid velocity, D the scalar diffusivity and $\dot{\omega}_{\xi}$ is the scalar reaction
 178 rate. Ξ represents any other source term such as production by a mean gradient.
 179 The iso-scalar ξ_0 forms an interface which separates the zones where $\xi(\mathbf{x}, t) > \xi_0$
 180 and $\xi(\mathbf{x}, t) < \xi_0$. It is then worth defining the phase indicator function $\phi =$

181 $H(\xi - \xi_0)$, where H denotes the Heaviside function. We then simply have:

$$182 \quad \phi(\mathbf{x}, t) = \begin{cases} 1 & \text{when } \xi > \xi_0 \\ 0 & \text{elsewhere.} \end{cases} \quad (2.2)$$

183 $\phi(\mathbf{x}, t)$ is sometimes referred to as the excursion set of $\xi(\mathbf{x}, t) > \xi_0$, i.e. the
184 probability that $\xi(\mathbf{x}, t) > \xi_0$ (Elsas *et al.* 2018). The transport equation for $\phi(\mathbf{x}, t)$
185 writes (Hirt & Nichols 1981; Drew 1990; Vassilicos & Hunt 1996):

$$186 \quad \partial_t \phi + \mathbf{u} \cdot \nabla_{\mathbf{x}} \phi = S_d |\nabla_{\mathbf{x}} \phi|. \quad (2.3)$$

187 $|\nabla_{\mathbf{x}} \bullet|$ denotes the norm of the gradient of any quantity \bullet and S_d is known as
188 intrinsic displacement speed of the interface. Note that Eq. (2.3) is valid only in
189 the sense of distributions (Drew 1990), i.e. outside from the interface both $\partial_t \phi$ and
190 $\nabla_{\mathbf{x}} \phi$ are zero, while they are equal to the Dirac delta function at the interface.
191 Similarly, S_d is defined only at the surface $\xi(\mathbf{x}) = \xi_0$. Eq. (2.3) shows that in the
192 laboratory coordinate system, the observer sees the interface moving at a speed
193 $\mathbf{w} = \mathbf{u} + S_d \mathbf{n}$ where $\mathbf{n} = -\nabla_{\mathbf{x}} \xi / |\nabla_{\mathbf{x}} \xi|$ is the unit vector normal to the iso-scalar
194 surface. When $S_d = 0$ (as in two-phase flows in absence of phase change), the
195 velocity of the interface \mathbf{w} is equal to the fluid velocity at the interface \mathbf{u} .

196 The displacement speed S_d is defined by (Gibson 1968; Pope 1988; Gran *et al.*
197 1996; Peters *et al.* 1998):

$$198 \quad S_d = \underbrace{\frac{\nabla_{\mathbf{x}} \cdot D \nabla_{\mathbf{x}} \xi}{|\nabla_{\mathbf{x}} \xi|}}_{S_d^d} + \underbrace{\frac{\Xi}{|\nabla_{\mathbf{x}} \xi|}}_{S_d^s} + \underbrace{\frac{\dot{\omega}_{\xi}}{|\nabla_{\mathbf{x}} \xi|}}_{S_d^r}. \quad (2.4)$$

199 Recall that S_d is defined only at $\xi(\mathbf{x}) = \xi_0$. Eq. (2.4) shows that the displacement
200 speed can be decomposed into a scalar diffusion component S_d^d , a scalar reaction
201 rate contribution S_d^r , and a scalar source term part S_d^s . Gran *et al.* (1996); Peters
202 *et al.* (1998) further showed that the diffusion component of the displacement
203 speed S_d^d can be further decomposed by projecting the diffusion term along the
204 iso-scalar surface normal and tangential directions:

$$205 \quad S_d^d = \underbrace{\frac{\mathbf{n} \cdot \nabla_{\mathbf{x}} (\mathbf{n} \cdot D \nabla \xi)}{|\nabla_{\mathbf{x}} \xi|}}_{S_d^n} + \underbrace{2D\mathcal{H}}_{S_d^c}, \quad (2.5)$$

206 where S_d^n and S_d^c are the normal and tangential diffusion contributions to the
207 displacement speed. $\mathcal{H} = \nabla_{\mathbf{x}} \cdot \mathbf{n} / 2$ is the mean curvature of the iso-surface.
208 It is negative when the surface is concave in the direction of $\xi(\mathbf{x}) > \xi_0$ and
209 convex in the opposite case. The rightmost term in Eq. (2.5) reveals that S_d^c
210 depends linearly on the mean curvature of the scalar iso-surface. In presence
211 of heat release, it may be more convenient to define S_d in a density weighted
212 formulation (Giannakopoulos *et al.* 2019; Gran *et al.* 1996; Peters *et al.* 1998).
213 Yu *et al.* (2021) derived the transport equations for the different components of
214 the displacement speed.

215 2.2. General two-point equations

216 The machinery for obtaining the two-point equations of the phase indicator field
217 when $S_d = 0$ is described in details by Thiasset *et al.* (2020, 2021). Here, we
218 aim at generalizing such equations for cases where the displacement speed is

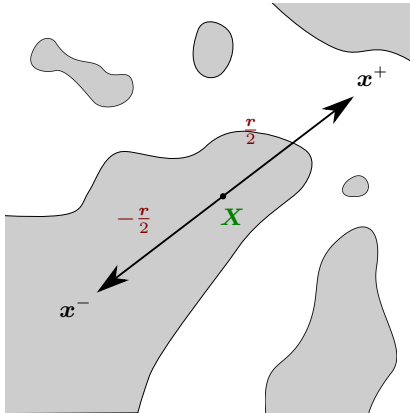


Figure 1: Schematic representation of two points \mathbf{x}^+ and \mathbf{x}^- , the midpoint $\mathbf{X} = (X, Y, Z)$ and the separation vector $\mathbf{r} = (r_x, r_y, r_z)$.

219 not zero. In this goal, we start by writing the transport equations for $\phi(\mathbf{x}, t)$
 220 at a point \mathbf{x}^+ and \mathbf{x}^- , arbitrarily separated in space (Fig. 1). Hereafter, the +
 221 and - superscripts denote the quantity at the point \mathbf{x}^+ and \mathbf{x}^- , respectively.
 222 Multiplying the equation at \mathbf{x}^+ by ϕ^- and the one at \mathbf{x}^- by ϕ^+ , yields:

$$223 \quad \phi^- \partial_t \phi^+ + \mathbf{u}^+ \cdot \phi^- \nabla_{\mathbf{x}^+} \phi^+ = \phi^- S_d^+ |\nabla_{\mathbf{x}} \phi|^+, \quad (2.6a)$$

$$224 \quad \phi^+ \partial_t \phi^- + \mathbf{u}^- \cdot \phi^+ \nabla_{\mathbf{x}^-} \phi^- = \phi^+ S_d^- |\nabla_{\mathbf{x}} \phi|^-. \quad (2.6b)$$

225 Since for any quantity $[\bullet]$, we have $\nabla_{\mathbf{x}^+} [\bullet]^- = \nabla_{\mathbf{x}^-} [\bullet]^+ = 0$, one obtains:

$$226 \quad \phi^- \partial_t \phi^+ + \mathbf{u}^+ \cdot \nabla_{\mathbf{x}^+} \phi^+ \phi^- = \phi^- S_d^+ |\nabla_{\mathbf{x}} \phi|^+, \quad (2.7a)$$

$$227 \quad \phi^+ \partial_t \phi^- + \mathbf{u}^- \cdot \nabla_{\mathbf{x}^-} \phi^- \phi^+ = \phi^+ S_d^- |\nabla_{\mathbf{x}} \phi|^-. \quad (2.7b)$$

228 Summing up these two equations gives,

$$229 \quad \partial_t \phi^+ \phi^- + \mathbf{u}^+ \cdot \nabla_{\mathbf{x}^+} \phi^+ \phi^- + \mathbf{u}^- \cdot \nabla_{\mathbf{x}^-} \phi^- \phi^+ \\
 230 \quad = \phi^- S_d^+ |\nabla_{\mathbf{x}} \phi|^+ + \phi^+ S_d^- |\nabla_{\mathbf{x}} \phi|^-. \quad (2.8)$$

231 We now define the mid-point $\mathbf{X} = (\mathbf{x}^+ + \mathbf{x}^-)/2$ and separation vector $\mathbf{r} = \mathbf{x}^+ - \mathbf{x}^-$
 232 (see Fig. 1). Using the relations $\nabla_{\mathbf{x}^+} = \frac{1}{2} \nabla_{\mathbf{X}} + \nabla_{\mathbf{r}}$ and $\nabla_{\mathbf{x}^-} = \frac{1}{2} \nabla_{\mathbf{X}} - \nabla_{\mathbf{r}}$ (Hill
 233 2002; Danaila *et al.* 2004), we obtain:

$$234 \quad \partial_t \phi^+ \phi^- = - \nabla_{\mathbf{X}} \cdot (\sigma \mathbf{u}) \phi^+ \phi^- - \nabla_{\mathbf{r}} \cdot (\delta \mathbf{u}) \phi^+ \phi^- \\
 + \phi^- S_d^+ |\nabla_{\mathbf{x}} \phi|^+ + \phi^+ S_d^- |\nabla_{\mathbf{x}} \phi|^+ \\
 + 2 \phi^+ \phi^- (\sigma \{ \nabla_{\mathbf{x}} \cdot \mathbf{u} \}) \quad (2.9)$$

235 Eq. (2.9) is the transport equation for the correlation function of the phase
 236 indicator field where S_d can take any values. $(\sigma \bullet) = (\bullet^+ + \bullet^-)/2$ and $(\delta \bullet) =$
 237 $(\bullet^+ - \bullet^-)$. Note that Eq. (2.9) also considers flows in which the velocity divergence
 238 may not be zero. This is accounted for in the rightmost term on right-hand side of
 239 Eq. (2.9) which reads as the product of $\phi^+ \phi^-$ and the average of $\nabla_{\mathbf{x}} \cdot \mathbf{u}$ between
 240 the two-points \mathbf{x}^+ and \mathbf{x}^- .

241 The squared increment of ϕ , i.e. $(\delta\phi)^2 = (\phi^+ - \phi^-)^2$ is related to $\phi^+ \phi^-$ by

$$\begin{aligned}
 242 \quad \phi^+ \phi^- &= \left(\frac{\phi^+ + \phi^-}{2} \right)^2 - \left(\frac{\phi^+ - \phi^-}{2} \right)^2 \\
 243 \quad &= (\sigma\phi)^2 - \frac{(\delta\phi)^2}{4} \\
 244 \quad &= \frac{1}{2} \left((\phi^+)^2 + (\phi^-)^2 \right) - \frac{(\delta\phi)^2}{2} \\
 245 \quad &= (\sigma\phi) - \frac{1}{2}(\delta\phi)^2. \tag{2.10}
 \end{aligned}$$

246 For obtaining Eq. (2.10), use was made of the relation $\phi^2 = \phi$ as ϕ can take
 247 only 0 or 1 values. Substituting Eq. (2.10) into Eq. (2.9), and noting that the
 248 transport equation for $(\sigma\phi)$ is

$$\begin{aligned}
 249 \quad \partial_t(\sigma\phi) &= -\nabla_{\mathbf{X}} \cdot (\sigma\mathbf{u})(\sigma\phi) - \nabla_{\mathbf{r}} \cdot (\delta\mathbf{u})(\sigma\phi) \\
 &\quad + \sigma\{S_d|\nabla\phi|\} + 2(\sigma\phi)(\sigma\{\nabla_{\mathbf{x}} \cdot \mathbf{u}\}), \tag{2.11}
 \end{aligned}$$

250 we end up with the transport equation for $(\delta\phi)^2$

$$\begin{aligned}
 \partial_t(\delta\phi)^2 &= -\nabla_{\mathbf{X}} \cdot (\sigma\mathbf{u})(\delta\phi)^2 - \nabla_{\mathbf{r}} \cdot (\delta\mathbf{u})(\delta\phi)^2 \\
 251 \quad &\quad + 2(\sigma\{S_d|\nabla\phi|\}) - 2(\phi^- S_d^+ |\nabla_{\mathbf{x}}\phi|^+ + \phi^+ S_d^- |\nabla_{\mathbf{x}}\phi|^-) \\
 &\quad + 2(\delta\phi)^2(\sigma\{\nabla_{\mathbf{x}} \cdot \mathbf{u}\}). \tag{2.12}
 \end{aligned}$$

252 Eq. (2.12) is the general expression for the unaveraged squared increments
 253 $(\delta\phi)^2$. It generalizes the equation derived by Thiesset *et al.* (2020, 2021) to the
 254 case where $S_d \neq 0$ and/or $\nabla_{\mathbf{x}} \cdot \mathbf{u} \neq 0$. Compared to the equations detailed by
 255 Thiesset *et al.* (2020, 2021), where only the unsteady and the two transfer terms
 256 (in \mathbf{r} and \mathbf{X} space) were present, Eq. (2.12) reveals an additional source term
 257 which notably depends on the correlation between a quantity related to the bulk
 258 phase ϕ and a surface quantity, namely $S_d|\nabla_{\mathbf{x}}\phi|$. When estimated numerically,
 259 this type of correlation requires a specific treatment which will be described later.
 260 The right-hand side of Eq. (2.12) also contains an additional non-linear forcing
 261 term which depends on the velocity divergence. In incompressible flows, this term
 262 vanishes.

263 Eq. (2.12) can be applied to very different types of scalar, either passive, active
 264 or reacting, in either decaying or forced turbulence, representative of either single
 265 or two-phase flows:

266 • In two-phase flows with no phase change, $S_d = 0$ and one recovers the
 267 equation first derived by Thiesset *et al.* (2020, 2021). Material surfaces share
 268 also the property $S_d = 0$ (Pope *et al.* 1989).

269 • In case of a passive scalar with no forcing, only S_d^d contributes to S_d . When
 270 e.g. a scalar mean gradient G_ξ in a given direction α is superimposed, then another
 271 contribution emerges from $S_d^s = u_\alpha G_\xi / |\nabla_{\mathbf{x}}\xi|$.

272 • The present framework also applies to premixed flames. Then, ξ can be
 273 associated to the fuel or oxidizer mass fraction or to the temperature field. In this
 274 situation, S_d incorporates both S_d^d and S_d^r . Diffusion flames can also be analyzed
 275 using the present framework. In either premixed or diffusion flames, one generally
 276 define S_d in the density weighted manner (Giannakopoulos *et al.* 2019). Note also

277 that due to heat release, one should also account for the additional term due to
278 $\nabla_{\mathbf{x}} \cdot \mathbf{u}$.

279 • In two-phase flows with phase change, ξ can for instance represent the liquid
280 volume fraction and S_d^r relates to the evaporation rate. Here again, one should
281 account for the term due to non-zero velocity divergence. The velocity jump
282 across the interface that originates from the evaporation rate and the density
283 jump between the two-phase should also be accounted for.

284 • Eq. (2.12) also applies to the enstrophy field. In this situation, S_d contains
285 a contribution due to diffusion effects and an additional forcing term due to
286 vortex stretching (Krug *et al.* 2015). The present framework is thus likely to help
287 scrutinizing the structure and kinematics of the turbulent/non-turbulent interface
288 which is often defined through a given iso-enstrophy value.

289 To summarize, the new framework proposed here is very general and enables
290 to treat a variety of different scalars (passive or reacting scalars, with or with-
291 out forcing) in different flow situations (single or two-phase flows, in forced or
292 decaying turbulence, in presence of phase change).

293 Because the flows under consideration can be turbulent, it is worth supplement-
294 ing Eqs. (2.9) and (2.12) by some averaging operators. The choice of a specific
295 average generally depends on the flow situations (Hill 2002; Thiesset *et al.* 2020,
296 2021). One can simply apply an ensemble average operator, noted $\langle \bullet \rangle_{\mathbb{E}}$, which
297 has the advantage of commuting with time t , spatial \mathbf{X} and scale \mathbf{r} derivatives.
298 Hence, the ensemble average of Eq. (2.12) is:

$$299 \quad \begin{aligned} \partial_t \langle (\delta\phi)^2 \rangle_{\mathbb{E}} &= -\nabla_{\mathbf{X}} \cdot \langle (\sigma\mathbf{u})(\delta\phi)^2 \rangle_{\mathbb{E}} - \nabla_{\mathbf{r}} \cdot \langle (\delta\mathbf{u})(\delta\phi)^2 \rangle_{\mathbb{E}} \\ &+ 2\langle \sigma \{S_d | \nabla\phi| \} \rangle_{\mathbb{E}} - 2(\langle \phi^- S_d^+ | \nabla_{\mathbf{x}}\phi|^+ \rangle_{\mathbb{E}} + \langle \phi^+ S_d^- | \nabla_{\mathbf{x}}\phi|^- \rangle_{\mathbb{E}}) \\ &+ 2\langle (\delta\phi)^2 (\sigma \{ \nabla_{\mathbf{x}} \cdot \mathbf{u} \}) \rangle_{\mathbb{E}}. \end{aligned} \quad (2.13)$$

300 In the present study, we further exploit the statistical symmetry of the flow (see
301 section 3.2) and we will consider a spatial average over a periodic domain of
302 volume V_{box} :

$$303 \quad \langle \bullet \rangle_{\mathbb{R}} = \frac{1}{V_{\text{box}}} \iiint_{\mathbf{X}} \bullet \, d\mathbf{X}. \quad (2.14)$$

304 Spatial averages commute with time t and \mathbf{r} derivatives, but not with the
305 \mathbf{X} divergence operator. However, by periodicity, the fluxes $(\sigma\mathbf{u})(\delta\phi)^2$ normal
306 to the domain boundaries vanish (Hill 2002; Thiesset *et al.* 2020). Hence, the
307 transfer term with respect to spatial position \mathbf{X} is zero. Assuming a divergence
308 free flow yields $\langle (\delta\phi)^2 (\sigma \{ \nabla_{\mathbf{x}} \cdot \mathbf{u} \}) \rangle_{\mathbb{E}, \mathbb{R}} = 0$. Statistical homogeneity leads to
309 $2\langle \sigma \{S_d | \nabla\phi| \} \rangle_{\mathbb{E}, \mathbb{R}} = \langle S_d | \nabla\phi| \rangle_{\mathbb{E}, \mathbb{R}}$ and $\langle \phi^- S_d^+ | \nabla_{\mathbf{x}}\phi|^+ \rangle_{\mathbb{E}} = \langle \phi^+ S_d^- | \nabla_{\mathbf{x}}\phi|^- \rangle_{\mathbb{E}}$. With
310 these simplifications, Eq. (2.12) then writes as:

$$311 \quad \underbrace{\partial_t \langle (\delta\phi)^2 \rangle_{\mathbb{R}}}_{\text{Unsteady}} = \underbrace{-\nabla_{\mathbf{r}} \cdot \langle (\delta\mathbf{u})(\delta\phi)^2 \rangle_{\mathbb{R}}}_{\text{Transfer-r}} + \underbrace{2\langle S_d \rangle_s \Sigma - 4\langle \phi^+ S_d^- | \nabla_{\mathbf{x}}\phi|^- \rangle_{\mathbb{R}}}_{S_d\text{-Term}}. \quad (2.15)$$

312 where $\Sigma = \langle | \nabla_{\mathbf{x}}\phi | \rangle_{\mathbb{R}}$ is the surface density of the iso-scalar surface, i.e. the area
313 of the iso-scalar surface divided by V_{box} . $\langle \bullet \rangle_s$ denotes the area weighted average.
314 At this stage, Eq. (2.15) depends on time t and the separation vector \mathbf{r} (a 4D
315 space). The problem can further be reduced supposing isotropy, i.e. statistical
316 invariance by rotation of the separation vector \mathbf{r} , i.e. $\langle \bullet \rangle_{\mathbb{R}}(\mathbf{r}) = \langle \bullet \rangle_{\mathbb{R}}(|\mathbf{r}|)$. In
317 case of anisotropic flows, one can apply an angular average, noted $\langle \bullet \rangle_{\Omega}$, over all

318 orientations of the vector \mathbf{r} (Thiesset *et al.* 2021):

$$319 \quad \langle \bullet \rangle_{\Omega} = \frac{1}{4\pi} \iint_{\Omega} \bullet \sin \theta d\theta d\varphi, \quad (2.16)$$

320 where the set of solid angles $\Omega = \{\varphi, \theta \mid 0 \leq \varphi \leq \pi, 0 \leq \theta \leq 2\pi\}$ with
 321 $\varphi = \arctan(r_y/r_x)$ and $\theta = \arccos(r_z/|\mathbf{r}|)$ (r_x, r_y, r_z denotes the components of
 322 the \mathbf{r} vector in x, y, z directions, respectively). Spatially and angularly averaged
 323 statistics depend on time t and scale r , i.e. the four dimensional problem was
 324 reduced to two dimensions.

325 2.3. Asymptotic limits at large and small scales

326 At this stage, it is worth recalling that employing two-point statistics of the phase
 327 indicator field is not new. It is widely employed for characterizing the micro-
 328 structure of heterogeneous material such as porous media, composite material,
 329 fractal aggregates, and colloids. The reader can refer to the book by Torquato
 330 (2002) who discusses in great details these aspects.

331 Among this wide corpus of literature, it is worth mentioning the work by
 332 Kirste & Porod (1962); Frisch & Stillinger (1963) who proved that for isotropic-
 333 homogeneous media, and by further assuming that the interface separating the
 334 two phases is of class C^2 , the limit of $\langle (\delta\phi)^2 \rangle_{\mathbb{R}}$ at small scales is given by:

$$335 \quad \lim_{r \rightarrow 0} \langle (\delta\phi)^2 \rangle_{\mathbb{R}} = \frac{\Sigma r}{2} \left[1 - \frac{r^2}{8} \left(\langle \mathcal{H}^2 \rangle_s - \frac{\langle \mathcal{G} \rangle_s}{3} \right) \right]. \quad (2.17)$$

336 Here, \mathcal{H} and \mathcal{G} are the mean and Gaussian curvatures, respectively. $\langle \bullet \rangle_s$ is used
 337 to denote the surface area weighted average. Berryman (1987); Thiesset *et al.*
 338 (2021) proved that Eq. (2.17) remains valid in anisotropic media by applying an
 339 additional angular average to $\langle (\delta\phi)^2 \rangle_{\mathbb{R}}$. When $|\mathbf{r}| \rightarrow \infty$, Thiesset *et al.* (2020,
 340 2021) showed that:

$$341 \quad \lim_{r \rightarrow \infty} \langle (\delta\phi)^2 \rangle_{\mathbb{R}} = 2\langle \phi \rangle_{\mathbb{R}}(1 - \langle \phi \rangle_{\mathbb{R}}). \quad (2.18)$$

342 The limit of $\langle \phi^+ |\nabla_{\mathbf{x}} \phi|^- \rangle_{\mathbb{R}}$ as $|\mathbf{r}|$ tends to zero can be expressed as follows (Teubner
 343 1990):

$$344 \quad \lim_{r \rightarrow 0} \langle \phi^+ |\nabla_{\mathbf{x}} \phi|^- \rangle_{\mathbb{R}} = \frac{\Sigma}{2} \left[1 + \frac{r}{2} \langle \mathcal{H} \rangle_s \right]. \quad (2.19)$$

345 As far as we are aware, the next terms of the small scale expansion of $\langle \phi^+ |\nabla_{\mathbf{x}} \phi|^- \rangle_{\mathbb{R}}$
 346 are not known. In the limit of large separations, we have (Teubner 1990)

$$347 \quad \lim_{r \rightarrow \infty} \langle \phi^+ |\nabla_{\mathbf{x}} \phi|^- \rangle_{\mathbb{R}} = \langle \phi \rangle_{\mathbb{R}} \Sigma. \quad (2.20)$$

348 The special case $\langle \phi \rangle_{\mathbb{R}} = 0.5$ yields $\langle \phi^+ |\nabla_{\mathbf{x}} \phi|^- \rangle_{\mathbb{R}}(r) = \Sigma/2$. Eq. (2.19) suggests
 349 that, when $|\mathbf{r}| \rightarrow 0$, $\langle \phi^+ S_d^- |\nabla_{\mathbf{x}} \phi|^- \rangle_{\mathbb{R}}$ writes:

$$350 \quad \lim_{r \rightarrow 0} \langle \phi^+ S_d^- |\nabla_{\mathbf{x}} \phi|^- \rangle_{\mathbb{R}} = \frac{\Sigma}{2} \left[\langle S_d \rangle_s + \frac{r}{2} \langle \mathcal{H} S_d \rangle_s \right], \quad (2.21)$$

351 while at large scales one may write:

$$352 \quad \lim_{r \rightarrow \infty} \langle \phi^+ S_d^- |\nabla_{\mathbf{x}} \phi|^- \rangle_{\mathbb{R}} = \langle \phi \rangle_{\mathbb{R}} \langle S_d \rangle_s \Sigma. \quad (2.22)$$

353 As discussed by Thiesset *et al.* (2021), Eq. (2.17) and similarly Eqs. (2.19) and
 354 (2.21) apply up to a separation r , which is twice the 'reach' of surface. The
 355 'reach' is a notion that pertains to non-convex bodies. It is defined as the minimal
 356 normal distance between the surface and its medial axis (see e.g. Federer 1959).
 357 The medial axis of a given body is the set of all points having more than one
 358 closest point on the object's boundary. It can also be seen as the location of
 359 centers of all bi-tangent spheres, i.e. the spheres that are tangent to the surface
 360 in at least two points on the surface. The reach is thus given by the minimal
 361 radius of these bi-tangent spheres. In some special situations (in absence of
 362 narrow throats or necks), it can be related to the minimal radius of curvature.
 363 Otherwise, it relates to the smallest narrow throat or neck. For scales larger than
 364 the reach, $\langle(\delta\phi)^2\rangle_{\mathbb{R}}$ contains information about the morphology of the structures
 365 under hand. In this respect, Adler *et al.* (1990); Torquato (2002); Thiesset *et al.*
 366 (2021) showed that the scale distribution $\langle\phi^+\phi^-\rangle_{\mathbb{R}}$ or $\langle(\delta\phi)^2\rangle_{\mathbb{R}}$ widens when the
 367 morphological content (or its tortuousness) of a given set increases. Similarly, the
 368 fractal facets of aggregates are often appraised by use of correlation function of
 369 the phase indicator at intermediate scales (see e.g. Sorensen 2001). In particular,
 370 Morán *et al.* (2019) showed that when increasing the ratio between the largest
 371 scales (the aggregate radius of gyration) and the smallest scales (the radius of
 372 the primary particle), the correlation function reveals an increasing range of
 373 scales complying with a fractal scaling (a power law). Vassilicos & Hunt (1991);
 374 Vassilicos (1992); Vassilicos & Hunt (1996) showed that $\langle(\delta\phi)^2\rangle_{\mathbb{E}}$ might reveal
 375 a power law behavior whose exponent is related to the fractal dimension (more
 376 precisely the Kolmogorov capacity) of iso-scalar surfaces. This was investigated
 377 in great details by Elsas *et al.* (2018) for the enstrophy, dissipation and velocity
 378 gradient invariants. When several structures are present, $\langle(\delta\phi)^2\rangle_{\mathbb{E},\mathbb{R}}$ also depends
 379 on the way the different fluid structures are organized in space. The reach of
 380 the surface plays an important role here since it is the scale which separates the
 381 zones in scale space where $\langle(\delta\phi)^2\rangle_{\mathbb{R}}$ depends only on integral geometric measures
 382 (Σ , $\langle\mathcal{H}^2\rangle_s$, $\langle\mathcal{G}\rangle_s$) and the range of scales for which two-point statistics become
 383 a morphological descriptor (Torquato 2002) for which both the geometry and
 384 the additional information about the medial axis is required for the structure to
 385 be characterized. For scales larger than the reach, the separation r cannot be
 386 interpreted as the size of the structure under consideration (as it will be seen
 387 later the correlation $\langle\phi^+\phi^-\rangle_{\mathbb{R}}$ tends to 0 when the scale r is similar to the size of
 388 the structure), but should rather be referred to as the morphological parameter
 389 as it is generally done in morphological analysis using e.g. integral geometrical
 390 measures (the Minkowski functional) of parallel sets (Arns *et al.* 2004; Dumouchel
 391 *et al.* 2022).

392 Given the asymptotic limits detailed in previous section, it seems natural to
 393 examine the limit at small and large-scales of Eq. (2.12) (or Eq. (2.9)). In Thiesset
 394 *et al.* (2021), it was demonstrated that Eq. (2.12) naturally converge to the
 395 transport equation for the surface density when $|\mathbf{r}| \rightarrow 0$. The latter can be written
 396 in the form (Pope 1988; Candel & Poinot 1990; Drew 1990; Blakeley *et al.* 2019):

$$397 \quad \partial_t \Sigma + \nabla_{\mathbf{x}} \cdot \langle \mathbf{u} \rangle_s \Sigma = (\mathbb{K}_T + \mathbb{K}_C) \Sigma, \quad (2.23)$$

398 where the stretch rate $\mathbb{K} = \mathbb{K}_T + \mathbb{K}_C$ measures the relative time increase of surface
 399 density. \mathbb{K}_T denotes the tangential strain rate that may include compressibility
 400 effect, and $\mathbb{K}_C = -2\langle S_d \mathcal{H} \rangle_s$ is the curvature component of the stretch rate.

401 Thiesset *et al.* (2021) considered the case where $S_d = 0$ (a material surface

402 as in two-phase flows) and showed that, in the limit of small separations, the
 403 \mathbf{X} -transport term in Eq. (2.12) asymptotes the convection process of the surface
 404 density Σ (the rightmost term on LHS Eq. (2.23)) while the unsteady term in Eq.
 405 (2.12) obviously tends to the unsteady term in Eq. (2.23). Thiesset *et al.* (2021)
 406 argued that by difference, the \mathbf{r} -transfer term is proportional to the strain rate
 407 \mathbb{K}_T , viz.

$$408 \quad \lim_{r \rightarrow 0} [-\nabla_{\mathbf{r}} \cdot \langle (\delta \mathbf{u})(\delta \phi)^2 \rangle_{\mathbb{R}}] = \mathbb{K}_T \Sigma \frac{r}{2}. \quad (2.24)$$

409 Note that here again, this holds true in anisotropic configuration by using an
 410 additional angular average. When the interface displacement speed is not zero,
 411 the RHS in Eq. (2.12) has the following asymptotic limit:

$$412 \quad \lim_{r \rightarrow 0} [2 \langle \sigma \langle S_d | \nabla \phi \rangle_{\mathbb{R}} \rangle - 2 \langle \langle \phi^- S_d^+ | \nabla_{\mathbf{x}} \phi |^+ \rangle_{\mathbb{R}} + \langle \phi^+ S_d^- | \nabla_{\mathbf{x}} \phi |^- \rangle_{\mathbb{R}}] \\
 413 \quad \quad \quad = 2 \langle S_d \rangle_s \Sigma - 2 \Sigma \left(\langle S_d \rangle_s + \langle S_d \mathcal{H} \rangle_s \frac{r}{2} \right) \\
 414 \quad \quad \quad \quad \quad \quad = -2 \langle S_d \mathcal{H} \rangle_s \Sigma \frac{r}{2} \\
 415 \quad \quad \quad \quad \quad \quad = \mathbb{K}_C \Sigma \frac{r}{2}. \quad (2.25)$$

416 Consequently, the additional term in the two-point budget due to the presence
 417 of an interface displacement speed asymptotes, in the limit of small separations,
 418 to the curvature component of the stretch rate.

419 Similarly, given that at large scales, the r -transfer term tends to zero, Eq. (2.12)
 420 should provide insights into the excursion set volume equation. We indeed obtain
 421 that at large scales, the budget simplifies to

$$422 \quad \lim_{r \rightarrow \infty} \partial_t \langle (\delta \phi)^2 \rangle_{\mathbb{R}} = 2(1 - 2 \langle \phi \rangle_{\mathbb{R}}) \partial_t \langle \phi \rangle_{\mathbb{R}} \\
 423 \quad \quad \quad = 2(1 - 2 \langle \phi \rangle_{\mathbb{R}}) \langle S_d \rangle_s \Sigma, \quad (2.26)$$

424 where use was made of the equation for the volume (Drew 1990):

$$425 \quad \partial_t \langle \phi \rangle_{\mathbb{R}} = \langle S_d \rangle_s \Sigma. \quad (2.27)$$

426 Note that the volume of the excursion set $\langle \phi \rangle_{\mathbb{R}}$ reads as the probability that
 427 $\xi(\mathbf{x}) > \xi_0$. It is thus related to the cumulative distribution of $\xi(\mathbf{x})$. Assuming a
 428 Gaussian distribution for the scalar field $\xi(\mathbf{x}, t)$, $\langle \phi \rangle_{\mathbb{R}}$ can be written analytically
 429 as

$$430 \quad \langle \phi \rangle_{\mathbb{R}} = \frac{1}{2} \left(1 - \operatorname{erf} \left(\frac{\xi_0}{\sqrt{2} \xi_{\text{rms}}} \right) \right) \quad (2.28)$$

431 where the subscript "rms" stands for the standard deviation of the considered
 432 quantity. To dig a little deeper in the interpretation of $\langle (\delta \phi)^2 \rangle_{\mathbb{R}}$, we can resort to
 433 some tools from mathematical morphology. This analysis is carried in Appendix
 434 A, where we provide a handy demonstration that at intermediate scales, $\langle (\delta \phi)^2 \rangle_{\mathbb{R}}$
 435 measures the morphological content of the sets under consideration. The *structure*
 436 *function* is thus here aptly named since it is a function that depends on the
 437 structure (actually the micro-structure) of the fluid elements. It allows some
 438 geometrical features of iso-scalar sets to be inferred such as its volume, the
 439 surface area, mean and Gaussian curvatures and its transport equation naturally
 440 approaches the transport equations of surface density and volume at respectively

441 small and large scales. Note that by virtue of the Gauss-Bonnet theorem, the
 442 presence of $\langle \mathcal{G} \rangle_s$ in Eq. (2.17) indicates that $\langle (\delta\phi)^2 \rangle_{\mathbb{R}}$ depends also on the topology
 443 (the Euler characteristic) of the field under consideration.

444 Consequently, the present set of equations allows not only the morphology of
 445 scalar excursion sets to be described, it also accounts for its kinematic evolution
 446 through Eqs. (2.9) or (2.12). The interface retains through its geometry and
 447 kinematics the signature of the flow dynamics and, in some instances (e.g. two-
 448 phase flows, TNTI), may even influence the whole flow dynamics. Therefore, we
 449 like referring this framework to as a morphodynamical theory since it is likely to
 450 provide insights into the morphological evolution of fluid elements.

451 3. Numerical database and post-processing

452 3.1. Direct Numerical Simulation of scalar mixing in decaying turbulence

453 The present analytical framework is appraised using data from Direct Numerical
 454 Simulations (DNS). We studied two flow configurations, i.e. forced turbulence
 455 (denoted by the "F" letter in Table 1) and decaying turbulence (denoted by the
 456 letter "D" in Table 1). We have also one case, noted "T", which was used for tests
 457 and validation purposes. Table 1 gathers all important simulation parameters and
 458 related statistical quantities, where N denotes the number of grid points along
 459 one coordinate axis, ν is the kinematic viscosity, and

$$460 \quad R_\lambda = \frac{u_{\text{rms}}\lambda}{\nu} \quad (3.1)$$

461 is the Reynolds number based on the Taylor micro-scale $\lambda = \sqrt{15\nu u_{\text{rms}}^2 / \langle \epsilon \rangle}$,
 462 where u_{rms} is the root-mean-square velocity, $\langle k \rangle = \langle u_i u_i \rangle / 2$ is the mean kinetic
 463 energy, and $\langle \epsilon \rangle = 2\nu \langle \mathcal{S}_{ij} \mathcal{S}_{ij} \rangle$ is the mean energy dissipation rate, with the strain
 464 rate tensor given by $\mathcal{S}_{ij} = (\partial u_i / \partial x_j + \partial u_j / \partial x_i) / 2$. Further, $\langle \xi^2 \rangle$ denotes the mean
 465 scalar variance, $\langle \epsilon_\xi \rangle = 2D \langle (\partial \xi / \partial x_i)^2 \rangle$ is the mean scalar dissipation rate and $\lambda_\xi =$
 466 $\sqrt{6D \langle \xi^2 \rangle / \langle \epsilon_\xi \rangle}$ denotes the Corrsin length-scale. L_t and L_ξ denote the integral
 467 length scales of the velocity and scalar fields, respectively. The Kolmogorov and
 468 the Batchelor length scales are defined as

$$469 \quad \eta = \left(\frac{\nu^3}{\langle \epsilon \rangle} \right)^{1/4} \quad \text{and} \quad \eta_B = \left(\frac{\nu D^2}{\langle \epsilon \rangle} \right)^{1/4} = \frac{\eta}{Sc^{1/2}}, \quad (3.2)$$

470 respectively. The turbulent Péclet number Pe_{λ_ξ} is defined in Section 4.5.

471 • The forced turbulence database encompasses 6 different values of Taylor
 472 based Reynolds numbers R_λ (cases F0 to F5 in Table 1) from 88 to 530. For the
 473 lowest Reynolds number (F0, $R_\lambda = 88$), we carried out another simulation with
 474 four different scalar fields with different diffusion coefficients D , which correspond
 475 to Schmidt number variations from $Sc = 0.1$ to 1.0. The numerical database for
 476 case F0 ($Sc = 1.0$) to F5 is the same as the one used in Gauding *et al.* (2015,
 477 2017). To maintain a statistically steady state, an external stochastic forcing is
 478 applied to the velocity field (Eswaran & Pope 1988). The forcing is statistically
 479 isotropic and limited to low wave-numbers to avoid the small scales to be affected
 480 by the forcing scheme. The passive scalar field is fed by a uniform mean scalar
 481 gradient G_ξ which is applied on the y -direction. Hence, the scalar field $\tilde{\xi}$ can be

482 decomposed into a mean field $G_\xi y$ and a fluctuating field ξ , i.e.,

$$483 \quad \tilde{\xi} = G_\xi y + \xi. \quad (3.3)$$

484 The value of the mean scalar gradient G_ξ is set to unity without loss of generality.
 485 The indicator function is defined on the fluctuating field ξ , which is statistically
 486 homogeneous but not isotropic. The statistical anisotropy that is induced by the
 487 mean scalar gradient is further discussed in appendix F. A resolution condition
 488 of $\kappa_{\max}\eta > 2.5$ (where κ_{\max} is the maximum wavenumber achievable on the
 489 numerical grid and η the Kolmogorov length-scale) is maintained for all cases. As
 490 a consequence, the number of grid points has been increased to as high as $N =$
 491 4096^3 for case F5. The statistics presented in Table 1 and throughout the paper
 492 correspond to spatial and ensemble averages over M statistically independent
 493 snapshots. M varies between 6 for case F5 to 106 for case F0. We have checked
 494 that the number of independent snapshots M was sufficient for two-point statistics
 495 to be converged. Some tests are reported in Appendix G

496 • For the decaying turbulence case, we explored two distinct situations, the
 497 first where the uniform imposed mean scalar gradient is maintained (case D0)
 498 and another where both the velocity and scalar field are decaying (case D1).
 499 For both D0 and D1, we have carried out DNS for two values for the Schmidt
 500 number (0.2 and 1.0). The initial velocity field is generated in spectral space to
 501 be random and statistically isotropic. It satisfies incompressibility and obeys a
 502 prescribed energy spectrum, i.e.,

$$503 \quad E(\kappa, t = 0) \propto \kappa^4 \exp\left(-2\left(\frac{\kappa}{\kappa_p}\right)^2\right), \quad (3.4)$$

504 where κ_p is the wave-number at which the initial energy spectrum has its peak.
 505 We chose $\kappa_p = 15$ as a compromise between limiting confinement effects and the
 506 goal of reaching a high Reynolds number. The initial mean kinetic energy $\langle k \rangle$
 507 equals 10 leading to an initial Reynolds number, defined as $u_{\text{rms}}(t = 0)/(\nu\kappa_p)$,
 508 as large as 689. For case D0, the scalar field is initialized to zero, allowing scalar
 509 structures to develop naturally from the injection of energy through the imposed
 510 mean scalar gradient. For case D1, the scalar field decays freely from a prescribed
 511 spectrum, which is identical to the energy spectrum of the velocity field given by
 512 Eq. (3.4) with the same initial peak wave-number κ_p . Values reported in Table
 513 1 and throughout the paper were obtained at time $t = 10$, which is about one
 514 decade after the onset of the exponential decay of the kinetic energy. At this time,
 515 turbulence is highly resolved with a resolution condition $\kappa_{\max}\eta = 12.5$. For more
 516 details on the setup of the simulations, see Gauding *et al.* (2019).

517 • The test case T0 corresponds to decaying turbulence, but with a mesh
 518 size of 512^3 . This allowed us to test the appropriateness of the post-processing
 519 procedures. These validations are presented in the Appendix B and C and
 520 discussed hereafter in the paper.

521 The present DNS data were obtained by solving the Navier-Stokes equations
 522 and a scalar advection-diffusion equation using a dealiased pseudo-spectral ap-
 523 proach. For dealiasing, a filter procedure proposed by Hou & Li (2007) is used,
 524 which ensures stability and inhibits spurious oscillations in real space. For cases
 525 F0-F5, a second order semi-implicit Adams-Bashforth/Crank-Nicolson method is
 526 used for temporal integration. For the decaying turbulence simulations D0-D1,
 527 a low-storage, stability preserving, third-order Runge-Kutta scheme is employed,

528 where for stability, the viscous and diffusive terms are treated by an integrating
 529 factor technique. For all cases, the numerical domain is a triply periodic box with
 530 length $L_{\text{box}} = 2\pi$. The simulations have been carried out with an in-house hybrid
 531 MPI/OpenMP parallelized simulation code on the supercomputer JUQUEEN at
 532 research center Jülich, Germany.

533 We show some typical snapshots of the $\xi(\mathbf{x}) = 0$ iso-surface for different values
 534 for the Schmidt and Reynolds numbers in Fig. 2. We show only a $2\pi \times 2\pi \times \pi/2$
 535 subset of the simulated domain. The interface is colored by the displacement
 536 speed S_d which is normalized by the velocity standard deviation $u_{\text{rms}} = 2\langle k \rangle/3$.
 537 The color scale covers the range $-1 \leq S_d/u_{\text{rms}} \leq 1$. Note that although Fig. 2
 538 gives another impression (remember that only a subset of the domain is presented
 539 here), the volume fraction formed by the iso-scalar $\xi(\mathbf{x}) = 0$ is the same for all
 540 cases and is equal to 0.5. We note that while keeping R_λ constant (the three
 541 leftmost figures in Fig. 2), a Schmidt number variation from 1 to 0.1 yields a
 542 substantial decrease of surface density. The interface is less wrinkled and the
 543 corrugation covers a narrower range of scales. This highlights the role of diffusion
 544 on the iso-surface geometrical quantities. On the other hand, an increase of the
 545 Reynolds number from (the four rightmost figures in Fig. 2) is followed by the
 546 creation of smaller and smaller wrinkles and an increase of the morphological
 547 content of the iso-scalar volume. $\langle(\delta\phi)^2\rangle_{\mathbb{R},\mathbb{E}}$ is thus believed to widen with R_λ .
 548 Fig. 2 also reveals that the displacement speed S_d varies mostly in zones of high
 549 curvature. This suggests that the curvature of the interface might play a crucial
 550 role for understanding the variations of the displacement speed and its different
 551 components.

3.2. Post-processing procedure

553 The computation of two-point statistics is challenging as it involves the execution
 554 of a convolution operation. We compute two-point statistics accurately in real
 555 space by a hybrid MPI/OpenMP parallelization employing the two-dimensional
 556 pencil domain decomposition of the DNS code. The partial angular average is
 557 approximated by averaging over the r_x -, r_y -, and r_z -directions. Special attention
 558 is required for the transfer term, which involves the divergence of a two-point
 559 quantity. To avoid the assumption of isotropy, the transfer term is approximated
 560 by a second-order finite difference scheme. For instance, in r_x -direction, the
 561 transfer term reads

$$\begin{aligned}
 \nabla_{\mathbf{r}} \cdot \langle(\delta\mathbf{u})(\delta\phi)^2\rangle_{\mathbb{R}}(r_x, 0, 0) &\approx \\
 &\frac{1}{2\Delta r_x} \left[\langle(\delta u_x)(\delta\phi)^2\rangle_{\mathbb{R}}(r_x + \Delta r_x, 0, 0) - \langle(\delta u_1)(\delta\phi)^2\rangle_{\mathbb{R}}(r_x - \Delta r_x, 0, 0) \right] + \\
 562 &\frac{1}{2\Delta r_y} \left[\langle(\delta u_y)(\delta\phi)^2\rangle_{\mathbb{R}}(r_x, \Delta r_y, 0) - \langle(\delta u_2)(\delta\phi)^2\rangle_{\mathbb{R}}(r_x, -\Delta r_y, 0) \right] + \\
 &\frac{1}{2\Delta r_z} \left[\langle(\delta u_z)(\delta\phi)^2\rangle_{\mathbb{R}}(r_x, 0, \Delta r_z) - \langle(\delta u_3)(\delta\phi)^2\rangle_{\mathbb{R}}(r_x, 0, -\Delta r_z) \right], \tag{3.5}
 \end{aligned}$$

563 where Δr_i is the grid spacing and u_x , u_y , u_z are the velocity component in x ,
 564 y , and z directions, respectively. The transfer terms in r_y - and r_z -directions are
 565 obtained by a similar procedure.

566 Some two-point statistics were also computed over the whole \mathbf{r} space using
 567 the routines available through the `increments` library of the project `pyarcher`
 568 (Thiesset & Poux 2020). Because six nested loops are needed to cover the

569 whole (\mathbf{X}, \mathbf{r}) -space, we make use of an openMP parallelization for enhancing
570 the calculation speed. Full 3D two-point distributions were estimated only for
571 case F0 and T0 and limited to the range of scales $-96dx \leq (r_x, r_y, r_z) \leq 96dx$
572 where most of the processes take place. By doing so, we are able to check that the
573 partial angular average operated only over r_x -, r_y -, and r_z -directions was leading
574 to similar results than those obtained from the full angular average over whole
575 set of solid angles. These tests are presented in Appendix C and show that the
576 partial angular average yields similar results as the full angular average. In what
577 follows, only the results for the partial angular average will be presented.

578 Compared to the equation derived by Thiesset *et al.* (2020), the influence of
579 the interface displacement results in an additional source term in Eq. (2.12).
580 The latter highlights a correlation of the bulk phase ϕ with the surface quantity
581 $S_d |\nabla_{\mathbf{x}} \phi|$. Hence, this term requires a special treatment. Here, we adapt and
582 develop a procedure inspired by the method of Seaton & Glandt (1986). The
583 reader is advised to refer to Appendix B for a description and a validation of the
584 method.

585 The geometrical properties of the iso-surface (local surface area, mean and
586 Gaussian curvatures, surface conditional statistics) are extracted using the
587 `surface_operators` routines of `pyarcher`. These are earlier versions of the
588 routines described by Essadki *et al.* (2019); Di Battista *et al.* (2019), now
589 available through the project `Mercur(v)`.

	F0	F1	F2	F3	F4	F5	D0	D1	T0
N	512^3	1024^3	1024^3	2048^3	2048^3	4096^3	3072^3	3072^3	512^3
R_λ	88	121	184	218	331	529	45	45	11
M	106	87	40	10	10	6	3	3	1
ν	0.01	0.0055	0.0025	0.0019	0.0010	0.00048	0.00025	0.00025	0.003
$\kappa_{\max}\eta$	3.90	4.94	2.78	4.37	2.66	2.50	13.6	13.6	11.0
Sc	1.0	0.4	0.2	0.1	1.0	1.0	1.0	0.2	1.0
G_ξ		1.00					1.00	0.00	0.00
$\langle k \rangle$	11.12	11.58	11.42	12.70	14.35	23.95	0.01	0.01	0.016
$\langle \epsilon \rangle$	10.75	11.06	10.30	11.87	12.55	28.51	0.0015	0.0015	0.0046
λ	0.32	0.24	0.17	0.14	0.11	0.06	0.13	0.13	0.33
L_t	0.82	0.80	0.79	0.78	0.81	0.78	0.46	0.46	0.59
$\langle \xi^2 \rangle$	1.90	1.61	1.39	1.16	2.25	2.41	0.26	5.46×10^{-4}	1.37×10^{-3}
$\langle \epsilon_\xi \rangle$	3.93	3.84	3.72	3.52	4.01	6.78	0.04	7.97×10^{-5}	4.06×10^{-4}
λ_ξ	0.17	0.25	0.33	0.44	0.07	0.03	0.096	0.10	0.25
L_ξ	0.49	0.49	0.55	0.60	0.64	0.51	0.38	0.47	0.46
Pe_{λ_ξ}	12.0	18.0	27.1	46.0	114.9	164.7	26.6	10.5	12.4
η_B	0.018	0.028	0.039	0.055	0.005	0.003	0.010	0.023	0.023

Table 1: Physical parameters and typical one-point statistics of the DNS database used in the present work

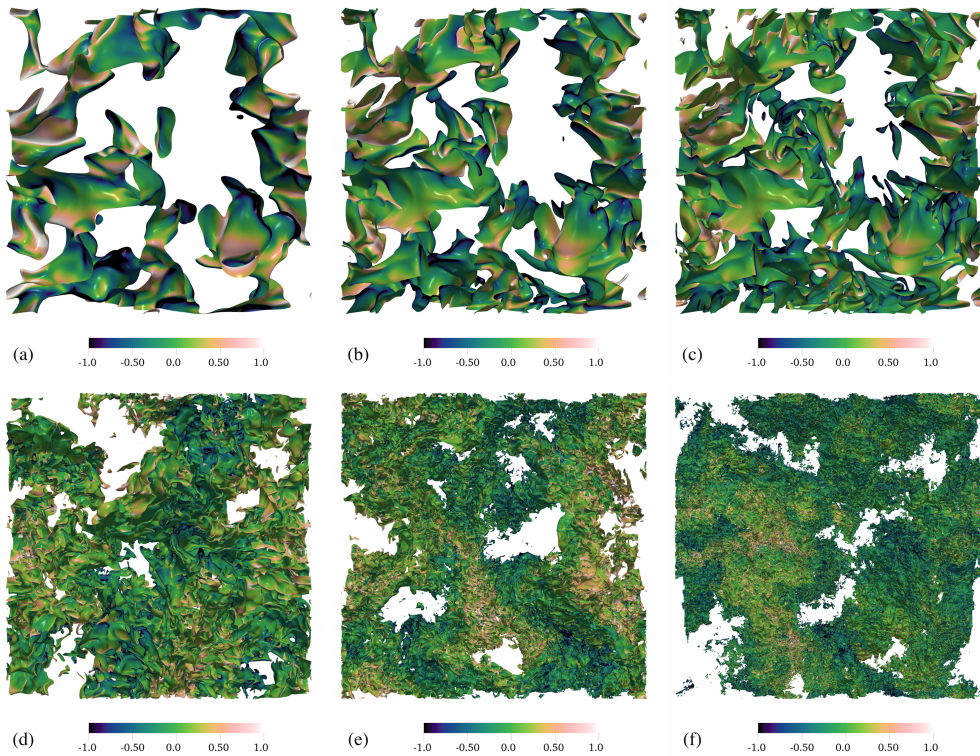


Figure 2: Iso-surface colored by the displacement speed S_d for increasing Schmidt numbers or Reynolds numbers. (a) F0, $Sc = 0.1$, (b) F0, 0.4 , (c) F0, 1.0 , (d) F2, (e) F4, (f) F5.

590 4. Results

591

4.1. Surface conditional statistics

592 The analytical section presented above reveals that the displacement speed S_d
 593 contains many of the key physics in the behavior of iso-scalar surfaces. Depending
 594 on the situation, it may incorporate different processes such as diffusion, chemical
 595 reactions or any other source terms acting on the scalar field. It is thus important
 596 to understand how S_d evolves along the iso-surface when R_λ and/or Sc are varied.
 597 In our situation, the displacement speed contains up to three components, one
 598 due to diffusion in the normal direction noted S_d^n , another due to diffusion in
 599 the tangential direction $S_d^c = 2D\mathcal{H}$ and a last contribution associated with
 600 the imposed mean scalar gradient noted S_d^s . Their respective expressions are
 601 summarized in Table 2.

602 As it is generally done in reacting flows (Gran *et al.* 1996; Peters *et al.* 1998),
 603 the variations of S_d along the surface $\xi(\mathbf{x}, t) = \xi_0$ are analyzed through surface
 604 weighted average of its different components conditioned on the mean curvature
 605 \mathcal{H} . These surface conditioned statistics are noted $\langle S_d^i | \mathcal{H} \rangle_s$ ($i = \{c, n, s\}$ denotes the
 606 contribution to the displacement speed). Such conditional statistics are relevant
 607 notably for providing insights into the curvature component of the stretch rate
 608 \mathbb{K}_C , which reads as the mean product of the displacement speed S_d by the mean
 609 curvature \mathcal{H} .

610 We first analyze the effect of R_λ on S_d and its components. Surface conditioned

$$\begin{aligned}
\text{Total } S_d &= S_d^s + S_d^d \\
&= \text{Source} \quad S_d^s = \frac{u_y G_\xi}{|\nabla_{\mathbf{x}} \xi|} \\
&+ \text{Diffusion} \quad S_d^d = S_d^c + S_d^n = \frac{\nabla_{\mathbf{x}} \cdot D \nabla_{\mathbf{x}} \xi}{|\nabla_{\mathbf{x}} \xi|} \\
&= \text{Tangential diffusion} \quad S_d^c = 2D\mathcal{H} \\
&+ \text{Normal diffusion} \quad S_d^n = \frac{\mathbf{n} \cdot \nabla_{\mathbf{x}} (\mathbf{n} \cdot D \nabla_{\mathbf{x}} \xi)}{|\nabla_{\mathbf{x}} \xi|}
\end{aligned}$$

Table 2: Expression of the different components of the displacement speed in forced turbulence with a mean scalar gradient G_ξ .

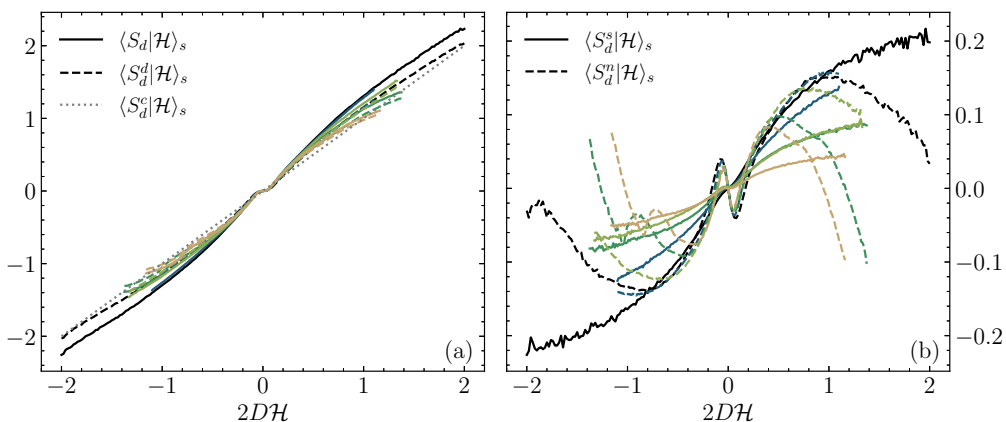


Figure 3: Surface averaged displacement speed and its components conditioned on the mean curvature \mathcal{H} for $\xi_0 = 0$. From dark to light, case F0 ($Sc = 1.0$) to F4. In (a) S_d (full lines), S_d^d (dashed lines) and S_d^c (dotted lines) are portrayed while S_d^n (dashed lines) and S_d^s (full lines) are displayed in (b).

611 statistics of S_d , S_d^d and S_d^c are portrayed in Fig. 3(a), while those of S_d^n and S_d^s are
612 displayed in Fig. 3(b). We consider here an iso-value of $\xi_0 = 0$. Note that in Fig.
613 3(a), the ordinate axis is ten times larger than the one of Fig. 3(b), which shows
614 that the source term and normal diffusion contributions of S_d are much smaller
615 than the tangential diffusion component. Therefore, assuming $S_d \approx 2D\mathcal{H}$ appears
616 as a reasonable assumption irrespectively of the Reynolds number. In Fig. 3(b),
617 we also note that variations of S_d^s decrease in amplitude when R_λ increases. This
618 suggests that the contribution due to the mean scalar gradient might become
619 negligible at sufficiently large R_λ . It is worth noting that the normal diffusion
620 component of the displacement speed S_d^n reveals a non-monotonic evolution with
621 respect to the mean curvature \mathcal{H} . When the surface is only slightly curved ($|\mathcal{H}|$
622 is small), S_d^n is negative (positive) for positive (negative) values of \mathcal{H} , while the
623 contrary is observed for highly curved regions. The variations of S_d^n with the
624 mean curvature does not depend on the Reynolds number for small values of \mathcal{H} .

625 The results for different Schmidt number are displayed in Fig. 4. One notes
626 again that the tangential diffusion component of the displacement speed S_d^c ,

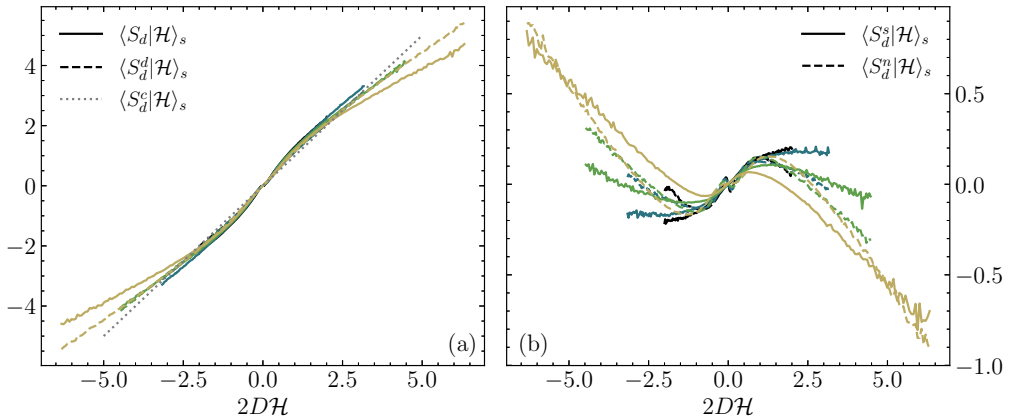


Figure 4: Surface averaged displacement speed and its components conditioned by the mean curvature \mathcal{H} for $\xi_0 = 0$. From dark to light, case F0, $Sc = 1.0$ to $Sc = 0.1$. In (a) S_d (full lines), S_d^d (dashed lines) and S_d^c (dotted lines) are portrayed while S_d^n (dashed lines) and S_d^s (full lines) are displayed in (b).

627 is predominant thereby emphasizing the role played by curvature. All curves
 628 collapse relatively well when the mean curvature is scaled by the scalar diffusivity
 629 D . When the Schmidt number decreases, the contribution due to the source term
 630 S_d^s increases and so does the normal diffusion contribution S_d^n .

631 The different components of the displacement speed $\langle S_d^i | \mathcal{H} \rangle_s$ for a different iso-
 632 scalar value $\xi_0 = \xi_{\text{rms}}$ are plotted in Figs. 5 and 6, respectively. We note here
 633 again that S_d^s and S_d^n are about 3 to 10 times smaller in amplitude than S_d^d
 634 and S_d^c . In contrast with $\xi_0 = 0$, S_d^n appears positive for all values of curvature
 635 and irrespective of the Schmidt and Reynolds numbers. Although the trends are
 636 quantitatively different from what was observed for $\xi_0 = 0$, we note that S_d
 637 remains strongly dependent to \mathcal{H} . In addition, a careful examination of Fig. 5
 638 reveals that when R_λ increases, the contribution of S_d^s and S_d^n decreases which
 639 leads to a better correlation between S_d and $2DH$. We can speculate that at
 640 asymptotically large R_λ , the assumption $S_d \approx 2DH$ holds true irrespective of
 641 the iso-scalar value. At constant R_λ , the contribution of S_d^s and S_d^n increases
 642 when the scalar diffusivity increases (Fig. 6). This suggests that the different
 643 contributions to S_d for different iso-level ξ_0 , should be better be studied in terms
 644 of Péclet number. In this context, we expect $S_d \approx 2DH$ to hold with better
 645 accuracy when the Péclet number increases.

646 It is worth finally stressing that our conclusion that the tangential diffusion
 647 dominates over the other components of the displacement speed, is built upon
 648 the observations of surface weighted averaged values conditioned by the mean
 649 curvature \mathcal{H} . This observable cannot reveal how S_d and its components are
 650 statistically distributed for a given \mathcal{H} . There is nothing precluding that locally,
 651 for a given value of mean curvature, the normal diffusion and/or the source term
 652 contributions to S_d dominate over the tangential diffusion. This is likely to be
 653 observed for low amplitudes of \mathcal{H} where the probability density function of \mathcal{H}
 654 is generally concentrated. More insights into this aspect could be provided by
 655 studying the joint probability density function of S_d^i and \mathcal{H} . This is far beyond
 656 the scope of the present work and is left of future investigations.

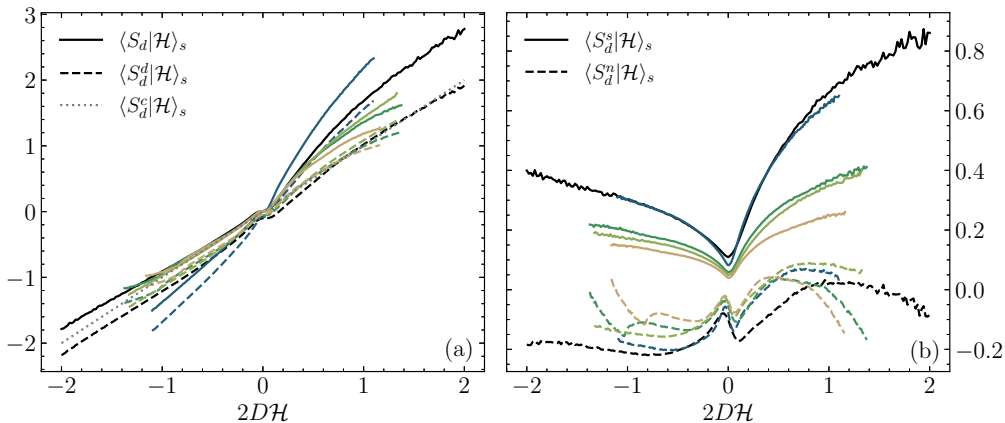


Figure 5: Surface averaged displacement speed and its components conditioned on the mean curvature \mathcal{H} for $\xi_0 = \xi_{\text{rms}}$. From dark to light, case F0 ($Sc = 1.0$) to F4. In (a) S_d (full lines), S_d^d (dashed lines) and S_d^c (dotted lines) are portrayed while S_d^n (dashed lines) and S_d^s (full lines) are displayed in (b).

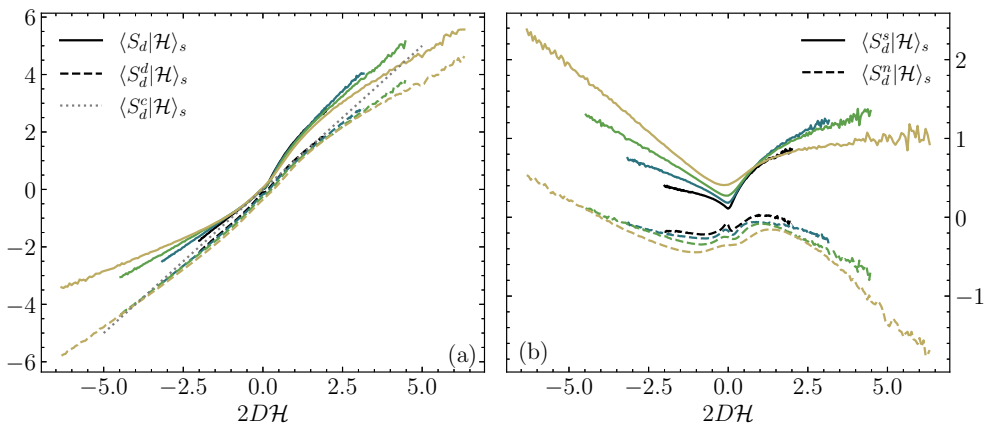


Figure 6: Surface averaged displacement speed and its components conditioned by the mean curvature \mathcal{H} for $\xi_0 = \xi_{\text{rms}}$. From dark to light, case F0, $Sc = 1.0$ to $Sc = 0.1$. In (a) S_d (full lines), S_d^d (dashed lines) and S_d^c (dotted lines) are portrayed while S_d^n (dashed lines) and S_d^s (full lines) are displayed in (b).

657

4.2. Second-order structure functions

658 The present framework is first invoked to explore the dynamics of iso-scalars
 659 with an imposed mean scalar gradient in stochastically forced turbulence. In this
 660 situation, both the flow and scalar characteristics are statistically stationary and
 661 the displacement speed has two components, one arising from the diffusive term
 662 S_d^d , and one due to the imposed mean gradient S_d^s . We focus on the particular
 663 effect of the Reynolds and Schmidt numbers.

664 The Reynolds number dependence of $\langle(\delta\phi)^2\rangle_{\mathbb{R},\mathbb{E},\Omega}$ for different values of the
 665 iso-scalar is first considered. Results are presented in Fig. 7 for R_λ ranging
 666 from 88 to 530 and for two values for the iso-scalar, i.e. $\xi_0 = 0$ (Fig. 7(a))
 667 and $\xi_0 = \xi_{\text{rms}}$ (Fig. 7(b)). $\langle(\delta\phi)^2\rangle_{\mathbb{R},\mathbb{E},\Omega}$ is normalized by its asymptotic value at
 668 large scales, i.e. $2\langle\phi\rangle_{\mathbb{R}}(1 - \langle\phi\rangle_{\mathbb{R}})$ while the separation r is normalized by $L_\Sigma =$

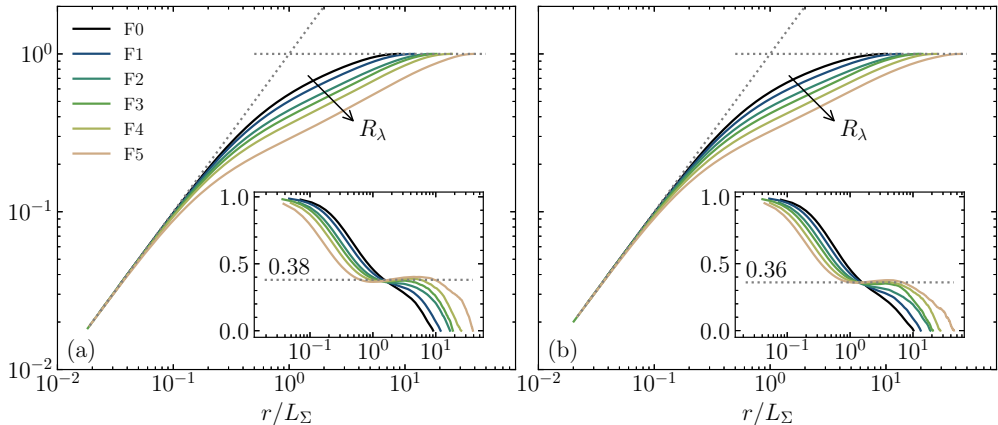


Figure 7: Evolution of $\langle(\delta\phi)^2\rangle_{\mathbb{E},\mathbb{R},\Omega}/2\langle\phi\rangle_{\mathbb{E},\mathbb{R}}(1-\langle\phi\rangle_{\mathbb{E},\mathbb{R}})$ with increasing R_λ . The separation r is normalized by $L_\Sigma = 4\langle\phi\rangle_{\mathbb{E},\mathbb{R}}(1-\langle\phi\rangle_{\mathbb{E},\mathbb{R}})/\Sigma$. The local scaling exponent is also plotted in the inset. The dotted gray lines represent the asymptotic theoretical limits at large and small scales. (a) $\xi_0 = 0$, (b) $\xi_0 = \xi_{\text{rms}}$.

669 $4\langle\phi\rangle_{\mathbb{E},\mathbb{R}}(1-\langle\phi\rangle_{\mathbb{E},\mathbb{R}})/\Sigma$. Using the normalization with $L_\Sigma = 4\langle\phi\rangle_{\mathbb{E},\mathbb{R}}(1-\langle\phi\rangle_{\mathbb{E},\mathbb{R}})/\Sigma$,
 670 the asymptotic limits at large and small scales intersect at $r/L_\Sigma = 1$. Our
 671 definition for L_Σ finds its inspiration in Lebas *et al.* (2009); Thiesset *et al.*
 672 (2020). A somehow similar definition for L_Σ was conjectured by Peters (1992)
 673 for premixed flames. In the context of the Bray-Moss-Libby model (Bray & Moss
 674 1977; Libby & Bray 1980), L_Σ is known as the wrinkling scale (Kulkarni *et al.*
 675 2021), although the surface density is defined differently by the latter authors.

676 One observes that all curves collapse at small scales where $\langle(\delta\phi)^2\rangle_{\mathbb{R},\mathbb{E},\Omega} \rightarrow \Sigma r/2$
 677 and at large scales where $\langle(\delta\phi)^2\rangle_{\mathbb{R},\mathbb{E},\Omega} \rightarrow 2\langle\phi\rangle_{\mathbb{E},\mathbb{R}}(1-\langle\phi\rangle_{\mathbb{E},\mathbb{R}})$. The most expert
 678 readers will probably notice that this behavior is also observed when two-point
 679 statistics of the velocity (or scalar) field are normalized by the Taylor (or Corrsin)
 680 microscale (Thiesset *et al.* 2014). Speculatively, this indicates that L_Σ plays for
 681 $\langle(\delta\phi)^2\rangle_{\mathbb{R},\mathbb{E},\Omega}$ the same role as the Taylor (Corrsin) microscale for normalizing the
 682 two-point statistics of the velocity (scalar) field.

683 At intermediate scales, the influence of the Reynolds number is perceptible. It
 684 is observed that a pseudo 'inertial range' is forming whose extent increases with
 685 R_λ . The local scaling exponent $\partial \log(\langle(\delta\phi)^2\rangle_{\mathbb{R},\mathbb{E},\Omega})/\partial \log(r)$ is plotted in the inset
 686 of Fig. 7 and reveals that a power law with an exponent of about $\zeta \approx 0.36 - 0.38$
 687 applies over about one decade at $R_\lambda = 530$. As shown by Vassilicos & Hunt
 688 (1996); Elsas *et al.* (2018), the distribution of $\langle(\delta\phi)^2\rangle_{\mathbb{R},\mathbb{E}}$ at intermediate scales
 689 contains information about the fractal characteristics of iso-scalar surfaces. The
 690 scaling exponents relate to the fractal dimension of the iso-surface by $D_f =$
 691 $3 - \zeta$. The same relation is used in the community of fractal aggregates (see e.g.
 692 Sorensen 2001; Morán *et al.* 2019). Note that what we call here a fractal dimension
 693 should rather be identified to a Kolmogorov capacity (Vassilicos & Hunt 1991;
 694 Vassilicos 1992). We also exclude the possibility that the fractal dimension of
 695 the intersection of the iso-scalar volume with a line (what we actually measure
 696 using two-point statistics of the phase indicator) may be different from the fractal
 697 dimension of the iso-volume itself (Vassilicos 1992).

698 The numerical value for D_f is found to be in the range $\{2.62 - 2.64\}$, in quite
 699 good agreement with the DNS value reported by Iyer *et al.* (2020) in the exact

700 same numerical configuration (they find $D_f = 2.67$ at $R_\lambda = 650$ for $\xi_0 = 0$ using
 701 the box-counting method) and the theoretical analysis of Mandelbrot (1975) or
 702 Grossmann & Lohse (1994) (also reproduced by Iyer *et al.* (2020)) providing a
 703 value of $8/3$. When $\xi_0 = \xi_{\text{rms}}$, the value for the fractal dimension is roughly the
 704 same although Iyer *et al.* (2020) showed that the fractal dimension decreases when
 705 the threshold ξ_0 is moved away from the mean value $\xi_0 = 0$. It is also worth noting
 706 that the scale dependence of the local slope in the range $L_\Sigma \leq r \leq 10L_\Sigma$ does
 707 not exceed 5%. This is in contrast with the results presented by Iyer *et al.* (2020)
 708 (see their Fig. 2) where there is no distinct scaling range for $\xi_0 = 0$. This suggests
 709 that, in agreement with the observations of Elsas *et al.* (2018), measuring the
 710 fractal dimension using the second-order structure function of the iso-scalar field
 711 is probably more robust than the one inferred from the box counting method.

712 The flow under consideration is anisotropic due to the presence of the mean
 713 scalar gradient. We here coped with this by employing the partial angular average
 714 along three coordinates of \mathbf{r} . It is thus worth evaluating if the above features for
 715 $\langle(\delta\phi)^2\rangle_{\mathbb{E},\mathbb{R}}$ are retrieved along the different directions of the separation vector
 716 \mathbf{r} . This point is addressed in Appendix F where similar trends are observed,
 717 irrespectively of the direction. Only some small differences between the directions
 718 parallel and perpendicular to the mean scalar gradient appear at the large scales.

719 In appendix D, we also consider normalizing the separation r by the radius of
 720 gyration R_g . The latter can be computed directly from $\langle(\delta\phi)^2\rangle_{\mathbb{R},\mathbb{E},\Omega}$ by (Sorensen
 721 2001; Yon *et al.* 2021):

$$722 \quad R_g^2 = \frac{1 \int_0^\infty r^4 A(r) dr}{2 \int_0^\infty r^2 A(r) dr} \quad (4.1)$$

723 where $A(r)$ is the correlation function normalized in such a way that $A(r) = 1$ at
 724 $r = 0$ and $A(r) = 0$ at large scales, viz.

$$725 \quad A(r) = 1 - \frac{\langle(\delta\phi)^2\rangle_{\mathbb{R},\mathbb{E},\Omega}}{2\langle\phi\rangle_{\mathbb{E},\mathbb{R}}(1 - \langle\phi\rangle_{\mathbb{E},\mathbb{R}})} \quad (4.2)$$

726 The results presented in Fig. 20 of appendix D show that the radius of gyration
 727 is a characteristic scale of the distribution $\langle(\delta\phi)^2\rangle_{\mathbb{R},\mathbb{E},\Omega}$ at large scales. Hence, R_g
 728 plays for $\langle(\delta\phi)^2\rangle_{\mathbb{R},\mathbb{E}}$ the same role as the integral length-scale for normalizing the
 729 two-point statistics of the velocity (or scalar) field.

730 In Appendix E, we also test the appropriateness of using the standard deviation
 731 of mean curvature \mathcal{H}_{rms} as a similarity variable. This type of normalization is
 732 expected to hold at small scales. Indeed, going back to Eq. (2.17), and further
 733 assuming $\langle\mathcal{G}\rangle_s \ll \langle\mathcal{H}^2\rangle_s$, we have

$$734 \quad \frac{\langle(\delta\phi)^2\rangle_{\mathbb{E},\mathbb{R},\Omega}}{\Sigma\mathcal{H}_{\text{rms}}^{-1}} = \frac{1}{2}r\mathcal{H}_{\text{rms}} \left(1 - \frac{(r\mathcal{H}_{\text{rms}})^2}{8} \right), \quad (4.3)$$

735 which is thus expected to be independent of Reynolds and Schmidt numbers
 736 when plotted in terms of $r\mathcal{H}_{\text{rms}}$. The evolution of $\langle(\delta\phi)^2\rangle_{\mathbb{E},\mathbb{R},\Omega}$ for different R_λ
 737 when the separation r is normalized by $r\mathcal{H}_{\text{rms}}$ is presented in Fig. 24 of Appendix
 738 E. It appears that $r\mathcal{H}_{\text{rms}}$ plays for the phase indicator field the same role as the
 739 Kolmogorov (or Batchelor) length-scale for normalizing the two-point statistics
 740 of the velocity (scalar) field.

741 The effect of Schmidt number on $\langle(\delta\phi)^2\rangle_{\mathbb{E},\mathbb{R},\Omega}$ is plotted in Fig. 8 for $R_\lambda =$

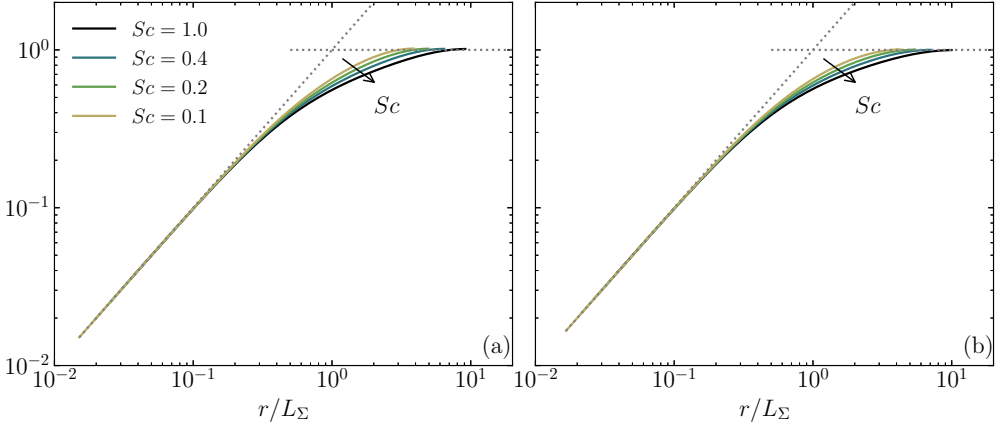


Figure 8: Evolution of $\langle(\delta\phi)^2\rangle_{\mathbb{E},\mathbb{R},\Omega}/2\langle\phi\rangle_{\mathbb{E},\mathbb{R}}(1-\langle\phi\rangle_{\mathbb{E},\mathbb{R}})$ with increasing Sc . The separation r is normalized by $L_\Sigma = 4\langle\phi\rangle_{\mathbb{E},\mathbb{R}}(1-\langle\phi\rangle_{\mathbb{E},\mathbb{R}})/\Sigma$. The dotted gray lines represent the asymptotic theoretical limits at large and small scales. (a) $\xi_0 = 0$, (b) $\xi_0 = \xi_{\text{rms}}$.

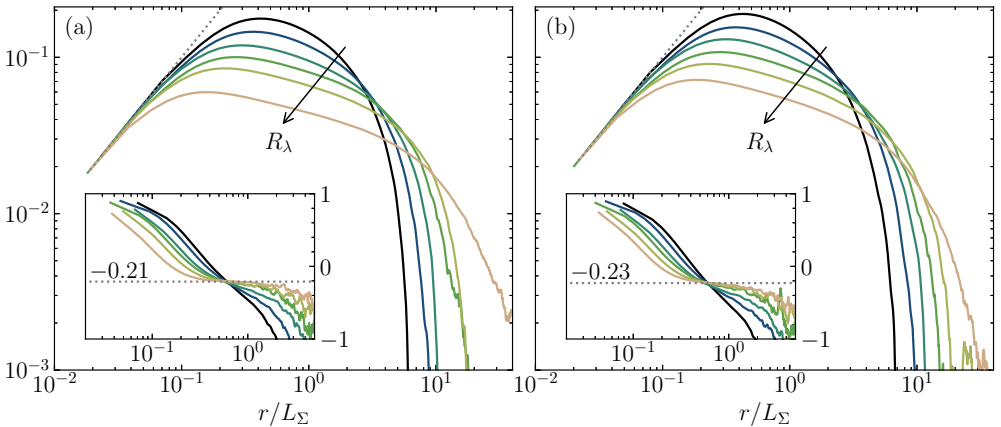


Figure 9: Evolution of the transfer term $-\langle\nabla_r \cdot \langle(\delta\mathbf{u})(\delta\phi)^2\rangle_{\mathbb{E},\mathbb{R}}\rangle_\Omega$ normalized by $2\mathbb{K}_T\langle\phi\rangle_{\mathbb{E},\mathbb{R}}(1-\langle\phi\rangle_{\mathbb{E},\mathbb{R}})$ with increasing R_λ . The separation r is normalized by L_Σ . The local scaling exponent is also plotted in the inset. The dotted gray lines represent the asymptotic theoretical limits at small scales. (a) $\xi_0 = 0$, (b) $\xi_0 = \xi_{\text{rms}}$. The color legend is the same as in Fig. 7.

742 88 and Sc ranging from 0.1 to 1 and $\xi_0 = 0$ (Fig. 8(a)) and ξ_{rms} (Fig. 8(b)).
 743 We observe again that normalizing the separation r by L_Σ and $\langle(\delta\phi)^2\rangle_{\mathbb{E},\mathbb{R},\Omega}$ by
 744 $2\langle\phi\rangle_{\mathbb{E},\mathbb{R}}(1-\langle\phi\rangle_{\mathbb{E},\mathbb{R}})$ yields a convincing collapse of the different curves at both small
 745 and large scales. The Schmidt number effects are perceptible only at intermediate
 746 scales where the scale distribution widens with increasing Sc . This means that
 747 increasing the diffusivity of the scalar tends to decrease the morphological content
 748 of the iso-scalar fields. This is the first evidence that diffusion acts as a restoration
 749 effect which counteracts the influence of turbulent straining. More details on this
 750 aspect will be given later when examining the budgets of $\langle(\delta\phi)^2\rangle_{\mathbb{E},\mathbb{R},\Omega}$.

4.3. Transfer term

751

752 We now address the influence of Reynolds and Schmidt numbers on the transfer
 753 term $-\langle \nabla_{\mathbf{r}} \cdot \langle (\delta \mathbf{u})(\delta \phi)^2 \rangle_{\mathbb{E}, \mathbb{R}} \rangle_{\Omega}$. In Fig. 9, we consider the case where R_{λ} is ranging
 754 from 88 to 530 and $Sc = 1.0$. The transfer term is normalized by $2\mathbb{K}_T \langle \phi \rangle_{\mathbb{E}, \mathbb{R}} (1 -$
 755 $\langle \phi \rangle_{\mathbb{E}, \mathbb{R}})$ while the separation is divided by L_{Σ} . This normalization is found to yield
 756 a **good** collapse of all curves at small scales. The specific evolution of the strain
 757 rate \mathbb{K}_T with respect to R_{λ} and Sc will be discussed later. Although visible, the
 758 influence of the iso-value ξ_0 is rather limited, at least when the latter is moved
 759 from $\xi_0 = 0$ to $\xi_0 = \xi_{\text{rms}}$.

760

In Fig. 21 of appendix D, we also report that the transfer term is independent
 761 of R_{λ} in the large-scales limit when the separation is normalized by R_g while $\langle \nabla_{\mathbf{r}} \cdot$
 762 $\langle (\delta \mathbf{u})(\delta \phi)^2 \rangle_{\mathbb{E}, \mathbb{R}} \rangle_{\Omega}$ is divided by a sort of turbulent strain felt at a scale R_g which
 763 can be written as $\sqrt{\langle k \rangle} / R_g$ ($\langle k \rangle$ is the turbulent kinetic energy). Consequently,
 764 R_g and $\sqrt{\langle k \rangle} / R_g$ are appropriate for normalizing the transfer term in the large
 765 scale limit. Fig. 25 of appendix E proves that the small-scale similarity variables
 766 for the transfer term are $\mathcal{H}_{\text{rms}}^{-1}$ and $\mathbb{K}_T \Sigma \mathcal{H}_{\text{rms}}^{-1}$ which plays for ϕ the same role as
 767 the Kolmogorov (Batchelor) scales for the velocity (scalar) field.

768

In Fig. 9, we also show the local scaling exponent of the transfer term. Although
 769 the scaling range appears more restricted than the one observed for second-
 770 order moments, there seems to be a plateau forming around a value of about
 771 $\{-0.21; -0.23\}$ at the larger R_{λ} . Let us naively assume that, at intermediate
 772 scales, the flux can be written as:

773

$$\langle (\delta \mathbf{u})(\delta \phi)^2 \rangle_{\mathbb{E}, \mathbb{R}} \sim \langle (\delta u_{\parallel})^2 \rangle_{\mathbb{R}, \mathbb{E}}^{1/2} \langle (\delta \phi)^2 \rangle_{\mathbb{R}, \mathbb{E}} \sim r^{\zeta_u/2 + \zeta}. \quad (4.4)$$

774

Here, $\delta u_{\parallel} = \delta \mathbf{u} \cdot \mathbf{r} / |\mathbf{r}|$ is the longitudinal increment of velocity. If we further
 775 state that ζ_u , the scaling exponent for the velocity structure function, is equal
 776 to $\zeta_u = 2/3$, we obtain that the transfer term should scale as $r^{\zeta - 2/3} = r^{7/3 - D_f}$
 777 which for $\zeta = \{0.36; 0.38\}$ gives a scaling exponent of $\{-0.29; -0.31\}$. Our
 778 numerical data indicate a value around $\{-0.21; -0.23\}$ for the transfer term
 779 scaling exponent which is in reasonable agreement with this crude scaling analysis.
 780 If we account for internal intermittency, i.e. $\zeta_u > 2/3$, the predicted exponent of
 781 the transfer term is closer to the numerical value. Note that this reasoning holds
 782 also in the small scale limit, where $\langle (\delta u_{\parallel})^2 \rangle^{1/2} \sim \langle (\delta \phi)^2 \rangle \sim r^1$ and hence the
 783 transfer term should scale as r^1 , which is numerically observed. To give this
 784 scaling analysis a bit more strength, we use the closure proposed by [de Divitiis](#)
 785 (2014, 2016, 2020) which has the advantage of not relying on a parametrized
 786 turbulent diffusion hypothesis. When adapted to $\langle (\delta \phi)^2 \rangle_{\mathbb{E}, \mathbb{R}}$, the latter writes,

787

$$-\langle \nabla_{\mathbf{r}} \cdot \langle (\delta \mathbf{u})(\delta \phi)^2 \rangle_{\mathbb{E}, \mathbb{R}} \rangle_{\Omega} = \frac{1}{2} \langle (\delta u_{\parallel})^2 \rangle_{\mathbb{E}, \mathbb{R}, \Omega}^{1/2} \partial_r \langle (\delta \phi)^2 \rangle_{\mathbb{E}, \mathbb{R}, \Omega}. \quad (4.5)$$

788

Assuming again that $\langle (\delta u_{\parallel})^2 \rangle_{\mathbb{E}, \mathbb{R}} \rangle_{\Omega}$ scales as r^2 at small scales and $r^{2/3}$ at in-
 789 termediate scales, we obtain that the transfer term should scale as r^1 and
 790 $r^{\zeta - 2/3} = r^{7/3 - D_f}$ at small and intermediate scales, respectively. This reasoning
 791 is in agreement with the numerical data.

792

While the Kolmogorov four-fifth law and Yaglom four-third law are known
 793 to provide a r^0 scaling for the transfer term of either velocity or scalar in the
 794 inertial range, the one pertaining to the phase indicator is substantially different
 795 and is proved to relate to the fractal dimension of the iso-surface. According to
 796 our elaborations, a fractal dimension of $8/3$ translates into a $r^{-1/3}$ scaling for

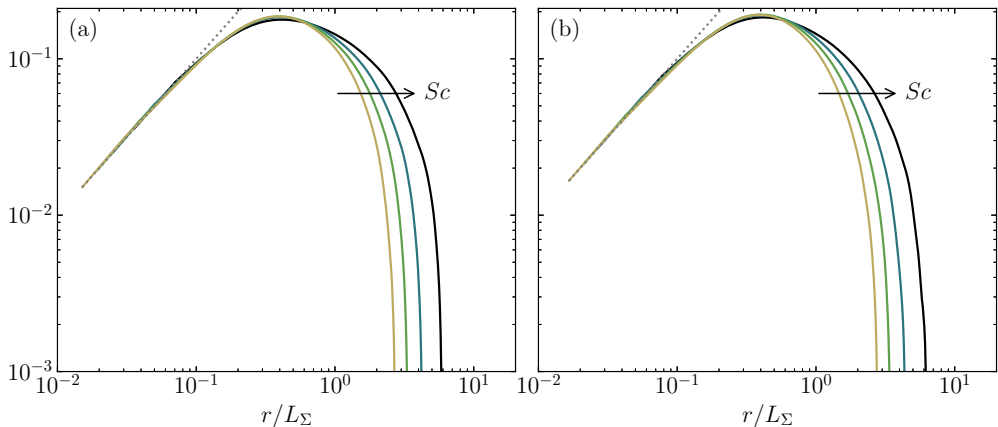


Figure 10: Evolution of the transfer term $-\langle \nabla_{\mathbf{r}} \cdot \langle (\delta \mathbf{u})(\delta \phi)^2 \rangle_{\mathbb{E}, \mathbb{R}} \rangle_{\Omega}$ normalized by $2\mathbb{K}_T \langle \phi \rangle_{\mathbb{E}, \mathbb{R}} (1 - \langle \phi \rangle_{\mathbb{E}, \mathbb{R}})$ with increasing Sc . The separation r is normalized by L_{Σ} . The dotted gray lines represent the asymptotic theoretical limits at small scales. (a) $\xi_0 = 0$, (b) $\xi_0 = \xi_{\text{rms}}$. The color legend is the same as in Fig. 8.

797 the transfer term of iso-volumes while a fractal dimension of $7/3$ results in a r^0
798 scaling.

799 The effect of Schmidt number on the transfer term is displayed in Fig. 10(a) for
800 $\xi_0 = 0$ and Fig. 10(b) for $\xi_0 = \xi_{\text{rms}}$. In both cases, $R_{\lambda} = 88$. When Sc increases
801 from 0.1 to 1.0, all curves collapse well at small scales thereby complying with
802 the $\{L_{\Sigma}, 2\mathbb{K}_T \langle \phi \rangle_{\mathbb{E}, \mathbb{R}} (1 - \langle \phi \rangle_{\mathbb{E}, \mathbb{R}})\}$ scaling. It is further observed that decreasing the
803 diffusivity of the scalar field (i.e. increasing the Schmidt number) acts in widening
804 the range of scales over which the transfer term operates. The same trend was
805 observed for increasing Reynolds numbers. This suggests that the appropriate
806 non-dimensional number for characterizing the phase indicator scale distribution
807 and its transfer is likely to be the Péclet number. This assertion will be discussed
808 in more details later in this paper.

809

4.4. Two-point budget

810 The different terms of the angularly averaged budget Eq. (2.15) for $Sc = 1.0$,
811 $88 \leq R_{\lambda} \leq 530$ and for two values for the iso-scalar $\xi_0 = 0$ and $\xi_0 = \xi_{\text{rms}}$
812 are presented in Fig. 11. Here again, the different terms are normalized by
813 $2\mathbb{K}_T \langle \phi \rangle_{\mathbb{E}, \mathbb{R}} (1 - \langle \phi \rangle_{\mathbb{E}, \mathbb{R}})$ while the separation is divided by L_{Σ} . The normalization
814 by the large-scale quantities R_g and $\sqrt{\langle k \rangle} / R_g$ is reported in Fig. 22 of Appendix
815 D while the one based on \mathcal{H}_{rms} and $\mathbb{K}_T \Sigma / \mathcal{H}_{\text{rms}}$ is plotted in Fig. 26 of Appendix
816 E.

817 Fig. 11 reveals that the transfer term is positive which means that, as expected,
818 the action of turbulence stirs, stretches and folds the scalar field thereby increas-
819 ing its tortuousness and its morphological content. The diffusive component of the
820 interface propagation term, i.e. the term due to S_d^d , is negative and thus acts in
821 smoothing the interface. Peters (1992) used to refer to the process associated
822 with S_d as a *kinematic restoration* effect which appears indeed aptly named
823 as it tends to counteract the influence of turbulent strain by smoothing the
824 interface. The term in the two-point budget associated with the imposed mean
825 gradient, i.e. the term due to S_d^s , is negative for an iso-scalar value $\xi_0 = 0$ and
826 positive for $\xi_0 = \xi_{\text{rms}}$. This indicates that the imposed mean gradient decreases

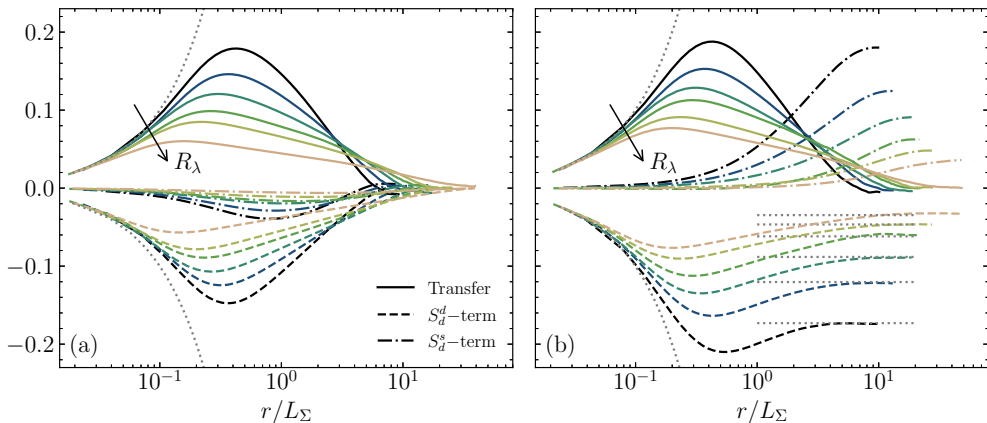


Figure 11: Budget of $\langle(\delta\phi)^2\rangle_{\mathbb{E},\mathbb{R},\Omega}$ with increasing R_λ . Full lines: transfer term, dashed lines: S_d^d -term, dash-dotted lines: S_d^s -term. All contributions are normalized by $2\mathbb{K}_T\langle\phi\rangle_{\mathbb{E},\mathbb{R}}(1-\langle\phi\rangle_{\mathbb{E},\mathbb{R}})$ while the separation r is normalized by L_Σ . (a) $\xi_0 = 0$, (b) $\xi_0 = \xi_{\text{rms}}$. The color legend is the same as in Fig. 7.

827 the morphological content of the iso-scalar close to the $\xi_0 = 0$ iso-value and
828 redistributes it to the scalar iso-values away from the mean.

829 The influence of R_λ is also visible in Fig. 11. When normalized by $2\mathbb{K}_T\langle\phi\rangle_{\mathbb{E},\mathbb{R}}(1-$
830 $\langle\phi\rangle_{\mathbb{E},\mathbb{R}})$, the different terms collapse at small scales and decrease in amplitude in
831 the intermediate range of scales. When R_λ increases, the range of scales over which
832 the different terms of the budget are contributing, increases. Using the large-scale
833 normalization (see Fig. 22 in appendix D), the terms collapse at large scales and
834 their respective amplitude increases with R_λ . The evolution of the different terms
835 of the budget using the small-scale similarity variables is presented in Fig. 26 of
836 Appendix E. It is also worth noting that, at small, up to intermediate scales,
837 the relative influence of the S_d^s -term compared to e.g. the transfer term decreases
838 when R_λ increases. This suggests that in the limit of very large R_λ , the strain rate
839 and the diffusion terms balance while the source term due to the imposed mean
840 gradient remains concentrated only at the large scales. In other words, at large
841 R_λ , the strain rate \mathbb{K}_T and the curvature component of the stretch rate due to
842 S_d^d , i.e. $\mathbb{K}_C^d = -2\langle S_d^d \mathcal{H} \rangle_s$ balance, whilst the curvature component of the stretch
843 rate due to S_d^s , i.e. $\mathbb{K}_C^s = -2\langle S_d^s \mathcal{H} \rangle_s$ tends to zero. For $\xi_0 = 0$, the area weighted
844 averaged displacement speed is zero. Fig. 11(a) confirms that all terms tend to
845 zero at large scales in agreement with Eq. (2.22). For $\xi_0 = \xi_{\text{rms}}$, only the transfer
846 term approaches zero when $r \rightarrow \infty$ while the S_d^d - and S_d^s -terms balance. The
847 limit of the S_d^d -term at large scales is also in agreement with Eq. (2.22) which is
848 displayed by the horizontal gray dotted lines in Fig. 11(b). The balance between
849 the S_d^d - and S_d^s -terms at large scales suggests that the volume of the excursion
850 set which naturally decreases due to diffusion effect is exactly compensated by
851 the imposed mean gradient.

852 The effect of Schmidt number on the different terms of the budget at constant
853 $R_\lambda = 88$ is displayed in Fig. 12(a) for $\xi_0 = 0$ and Fig. 12(b) for $\xi_0 = \xi_{\text{rms}}$. Here
854 again, the normalization using L_Σ and \mathbb{K}_T yields a good collapse of all curves
855 in the limit of small separations. For $\xi_0 = 0$, decreasing the Schmidt number
856 from 1.0 to 0.1, i.e. increasing the scalar diffusivity by a factor of 10, leads to
857 a smaller amplitude of the diffusion term in the intermediate range of scales. In

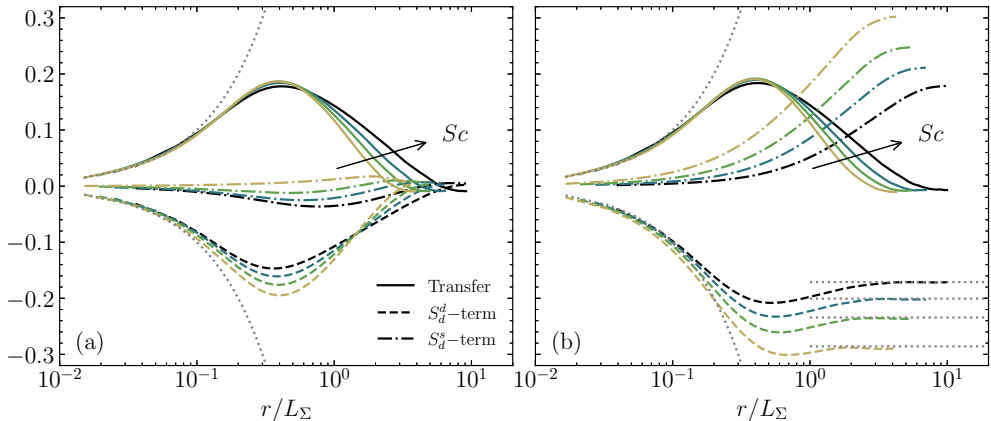


Figure 12: Budget of $\langle(\delta\phi)^2\rangle_{\mathbb{E},\mathbb{R},\Omega}$ with increasing Sc . Full lines: transfer term, dashed lines: S_d^d -term, dash-dotted lines: S_d^s -term, dotted lines: $-S_d^d$ -term. All contributions are normalized by $2\mathbb{K}_T\langle\phi\rangle_{\mathbb{E},\mathbb{R}}(1 - \langle\phi\rangle_{\mathbb{E},\mathbb{R}})$ while the separation r is normalized by L_Σ . (a) $\xi_0 = 0$, (b) $\xi_0 = \xi_{\text{rms}}$. The color legend is the same as in Fig. 8.

858 the same range of scales (i.e. up to $r \approx L_\Sigma$), the transfer term normalized by \mathbb{K}_T
859 appears rather insensitive to Schmidt number variations. The influence of Sc on
860 the transfer term is perceptible only at large scales where it is observed that the
861 scale at which the transfer term approaches zero decreases with increasing scalar
862 diffusivity. The third term in the budget due to the imposed mean gradient is
863 plotted as dash-dotted lines. When $\xi_0 = 0$, the latter is negative, progressively
864 tends to zero when Sc decreases, and becomes even slightly positive for $Sc = 0.1$.
865 This means that when $Sc = 0.1$, the scalar is so diffusive that the imposed
866 mean gradient becomes a gain in the budget for this particular iso-value. For
867 $\xi_0 = \xi_{\text{rms}}$, the term due to the imposed mean gradient acts at rather large scales,
868 is positive and increases in amplitude when Sc decreases. At large scales the
869 budget is composed of only the diffusion and imposed mean gradient terms, while
870 the transfer term is zero.

871 4.5. Strain and curvature components of the stretch rate

872 We now investigate the evolution of the different normalizing quantities with
873 respect to R_λ and Sc . When both R_λ and Sc vary, it may be more appropriate
874 to define the turbulent Péclet number:

$$875 \quad Pe_{\lambda_\xi} = \frac{\sqrt{2\langle k \rangle / 3} \lambda_\xi}{D} \quad (4.6)$$

876 With this definition, the Péclet number is related to the Schmidt and Reynolds
877 number by

$$878 \quad Pe_{\lambda_\xi} = \left(\frac{6R}{10}\right)^{1/2} R_\lambda Sc^{1/2} \quad (4.7)$$

879 where R is the scalar to mechanical time-scale ratio, i.e.

$$880 \quad R = \frac{\langle \xi^2 \rangle \langle \epsilon \rangle}{\langle \epsilon_\xi \rangle \langle k \rangle} \quad (4.8)$$

881 which may also vary with R_λ and Sc .

882 We first characterize the influence of the Péclet number on \mathbb{K}_T , \mathbb{K}_C^d and \mathbb{K}_C^s .
 883 \mathbb{K}_T is inferred from Eq. (2.24), i.e. from the slope of the transfer term in the limit
 884 of small scales. Similarly, Eq. (2.25) reveals that \mathbb{K}_C^d and \mathbb{K}_C^s can be obtained
 885 from the slope of the S_d^d and S_d^s terms, respectively, when r approaches zero.
 886 Results are portrayed in Fig. 13 where all quantities are made non-dimensional
 887 by multiplying by the Kolmogorov time scale $\tau_\eta = (\nu/\langle\epsilon\rangle)^{1/2}$.

888 For $Pe_{\lambda_\xi} > 50$, the normalized strain rate $\mathbb{K}_T\tau_\eta$ is nearly constant around a
 889 value of about 0.25. Since this observation holds for both $\xi_0 = 0$ and $\xi_0 = \xi_{\text{rms}}$,
 890 this means that the different iso-scalars experience nearly the same turbulent
 891 straining. The value of $0.25\tau_\eta$ is in agreement with the finding of Yeung *et al.*
 892 (1990) who report a value of 0.28 for material surfaces. It is also consistent
 893 with the phenomenological model of Thiesset *et al.* (2016b) which gives roughly
 894 the same value of 0.28. It is argued by Girimaji & Pope (1992) that the strain
 895 rate experienced by propagating surfaces is smaller than that acting on material
 896 surfaces since there will be less time for the iso-surface to align with strain. Our
 897 value of 0.25 for $\mathbb{K}_T\tau_\eta$ instead of 0.28 is thus consistent with this argument. In
 898 addition, when the scalar diffusivity is increased so that $Pe_{\lambda_\xi} < 50$, we note a
 899 substantial decrease of $\mathbb{K}_T\tau_\eta$ which drops down to 0.2. This indicates that the
 900 higher the diffusivity, the larger is the displacement speed, and the smaller the
 901 time for the iso-surface to align with strain. The constancy of $\mathbb{K}_T\tau_\eta$ at large Péclet
 902 numbers is also predicted by the closure of de Divitiis (2014, 2016, 2020) given
 903 by Eq. (4.5). Indeed, Kolmogorov's first similarity hypothesis implies for $r \rightarrow 0$:

$$904 \quad \langle(\delta u_{||})^2\rangle_{\mathbb{E},\mathbb{R},\Omega} \sim \frac{\langle\epsilon\rangle}{\nu} r^2, \quad (4.9)$$

905 which by virtue of Eqs. (2.17) and (2.24) gives $\mathbb{K}_T\tau_\eta = \text{const.}$.

906 A careful analysis of Fig. 13 further shows that $K_C^d\tau_\eta$ is always negative and
 907 thus counteracts the effect of turbulent straining. It also approaches a constant
 908 value when Péclet increases, but at a smaller rate than \mathbb{K}_T . The influence of
 909 the imposed mean gradient on the source component of the stretch rate $K_C^s\tau_\eta$ is
 910 perceptible at finite Péclet number and it is observed to be negative for $\xi_0 = 0$ and
 911 positive for $\xi_0 = \xi_{\text{rms}}$. Here again, this suggests that the imposed mean gradient
 912 acts in redistributing the surface density from the mean iso-value $\xi_0 = 0$ to iso-
 913 values away from the mean. $K_C^s\tau_\eta$ approaches zero at the highest Péclet number.
 914 This indicates that in the limit of very high Pe_{λ_ξ} , the imposed mean gradient
 915 does not influence the evolution of the iso-scalar surface density, the latter being
 916 driven only by diffusion and straining effects.

917 4.6. Characteristic length-scales

918 The previous analysis of two-point statistics highlighted the existence of three
 919 characteristic length-scales for the excursion set ϕ . The first one, L_Σ , is relevant
 920 for normalizing the two-point statistics at both small and large scales. The second
 921 R_g applies in the large scale limit while the third $\mathcal{H}_{\text{rms}}^{-1}$ is relevant at small up to
 922 intermediate scales. Some speculations about the connection between L_Σ ($\mathcal{H}_{\text{rms}}^{-1}$)
 923 and the Corrsin (Batchelor) microscales have already been stated earlier in this
 924 paper. We now provide more rigorous evidence for this.

925 First, it is worth recalling that, for isotropic media, the surface density Σ
 926 is related to the number of zero-crossings of the field $\xi(\mathbf{x}) - \xi_0$ (Torquato
 927 2002). On the other hand, there exist numerous studies that highlight a close

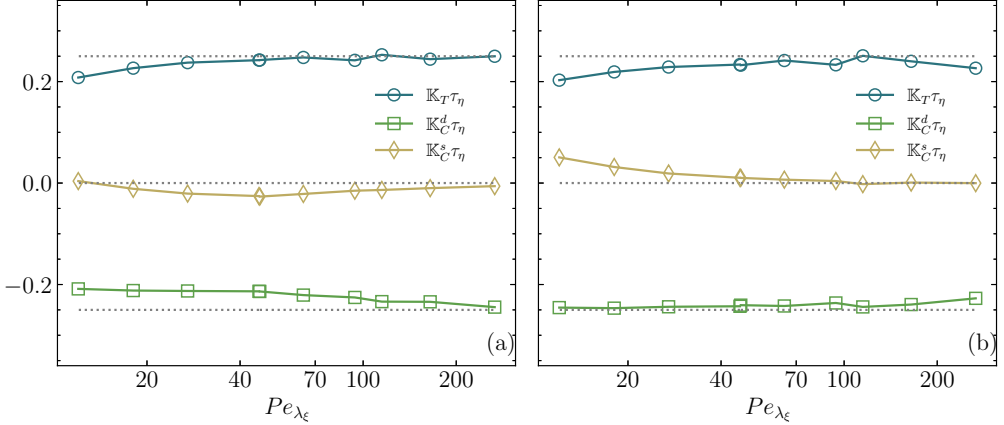


Figure 13: Scaling of the different components of the stretch rate $\mathbb{K} = \mathbb{K}_T + \mathbb{K}_C$ with respect to R_λ . (a) $\xi_0 = 0$, (b) $\xi_0 = \xi_{\text{rms}}$.

928 relation between the Taylor microscale and the number of zero-crossings of
 929 turbulent signals (see e.g. [Liepmann 1949](#); [Sreenivasan et al. 1983](#); [Mazellier &](#)
 930 [Vassilicos 2008](#), among others). Hence, there are reasons to expect that L_Σ and
 931 the Corrsin microscale λ_ξ are intimately linked. Recall that the Corrsin microscale
 932 is here defined by $\lambda_\xi^2 = 6D\langle\xi^2\rangle_{\mathbb{E},\mathbb{R}}/\langle\epsilon_\xi\rangle_{\mathbb{E},\mathbb{R}}$. Second, given that R_g is the relevant
 933 normalizing scale in the large scale limit, it seems natural to associate R_g with
 934 the integral length-scale of the scalar field noted L_ξ . Here, L_ξ is computed from
 935 the scalar fluctuations spectrum $E_\xi(\kappa)$, i.e.

$$936 \quad L_\xi = \frac{\pi \int_0^\infty \kappa^{-1} E_\xi(\kappa) d\kappa}{2 \int_0^\infty E_\xi(\kappa) d\kappa} \quad (4.10)$$

937 These arguments are tested against numerical data in Fig 14(a). While Pe_{λ_ξ} is
 938 multiplied by roughly 20, the ratio R_g/L_ξ and λ_ξ/L_Σ remain close to 0.5 with some
 939 small departures which do not exceed $\pm 20\%$. Hence, it appears that $L_\Sigma \sim \lambda_\xi$ and
 940 $R_g \sim L_\xi$ are good approximations. The small departures in the scaling between R_g
 941 and L_ξ can be due to several effects. First, some confinement due to the finite ratio
 942 between L_ξ and the simulation box size can be at play. Second, the scaling between
 943 R_g and L_ξ can also be altered by some finite Péclet numbers effects. The latter
 944 are likely to reveal themselves in the evolution of R_g/L_ξ which is first decreasing
 945 before reaching a plateau for Péclet numbers above 50. Such finite Péclet number
 946 effects were also noticed by [Shete & de Bruyn Kops \(2020\)](#). As far as the scaling
 947 between L_Σ and λ_ξ is concerned, it is first worth recalling that the Rice's theorem
 948 is valid only if both ξ and $\nabla\xi$ have Gaussian probability density functions and are
 949 statistically uncorrelated. While ξ is normally distributed, internal intermittency
 950 leads to significant departure from Gaussian distributions for the scalar gradient.
 951 At finite Reynolds or Péclet numbers, the assumption of statistical independence
 952 between ξ and its derivatives is not likely to hold. As a consequence, all data
 953 from the literature (e.g. [Sreenivasan et al. 1983](#)) indicate that the Rice theorem
 954 is a good approximation for turbulent signals verified within 20%. Departures are
 955 thus of same magnitude here. Finally, we explored here only two scalar iso-values.
 956 It is not excluded that the proportionality between L_Σ and λ_ξ ceases to apply
 957 for some higher iso-values of ξ_0 .

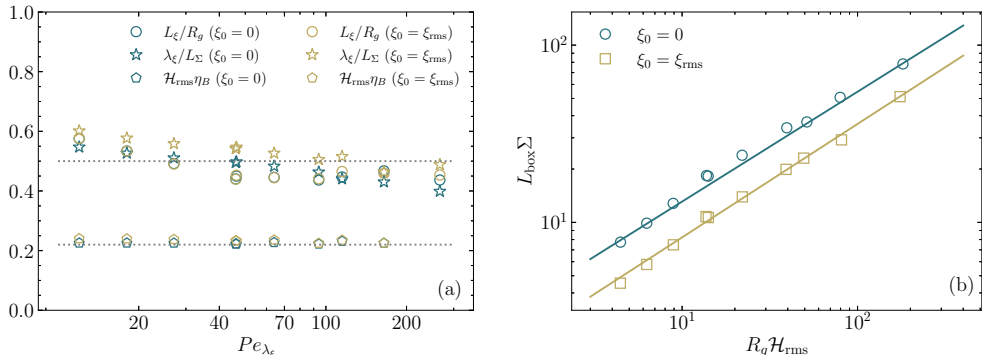


Figure 14: (a) Ratio of the length-scales L_ξ/R_g , λ_ξ/L_Σ and $\mathcal{H}_{\text{rms}}\eta_B$, with respect to Pe_{λ_ξ} for both $\xi_0 = 0$ and $\xi_0 = \xi_{\text{rms}}$. The dotted lines represent a ratio of 0.5 and 0.22. (b) Surface density Σ versus $R_g\mathcal{H}_{\text{rms}}$. The lines represent the expectations using a fractal dimension $D_f = 2.62$.

958 Let us now focus on the scaling of \mathcal{H}_{rms} . It is first worth recalling that the
 959 relation $\mathbb{K}_T \approx \mathbb{K}_C^d \sim \tau_\eta$ holds relatively well, except maybe at the smallest Péclet
 960 numbers (Fig. 13). On the other hand, the analysis performed in section 4.1
 961 indicates that $S_d \approx 2D\mathcal{H}$ is a rather safe approximation. With these relations,
 962 one can easily conclude that the standard deviation of the mean curvature
 963 is proportional to the inverse of the Batchelor length-scale η_B . This result is
 964 tested with success in Fig. 14(a) which proves that the standard deviation
 965 of mean curvature is indeed proportional to the Batchelor length-scale (Due
 966 to computational limitations, we were unable to estimate \mathcal{H}_{rms} for case F5.
 967 Hereafter, we will assume $\mathcal{H}_{\text{rms}} = 0.22/\eta_B$ for this case). It is worth noting
 968 that DNS data give $\eta_B\mathcal{H}_{\text{rms}} = \text{const.}$ even at low Péclet numbers where the
 969 approximation $\mathbb{K}_T \approx \mathbb{K}_C^d \sim \tau_\eta$ does not hold anymore. We thus believe that
 970 the relation between the Batchelor length-scale and the standard deviation of
 971 mean curvature is likely to be a general result which does not necessarily requires
 972 $\mathbb{K}_T \approx \mathbb{K}_C^d \sim \tau_\eta$. We have also tested the scaling of \mathcal{H}_{rms} with the Obukhov-Corrsin
 973 length-scale $\eta_{OC} = (D^3/\langle\epsilon\rangle)^{1/4} = \eta/Sc^{3/4}$ (not shown), but the latter was found to
 974 be inappropriate. This conclusion is consistent with the findings of e.g. [Antonia & Orlandi \(2003\)](#);
 975 [Donzis et al. \(2005\)](#) which prove that the Batchelor length-scale is the appropriate
 976 normalizing the scalar fluctuations scale distributions
 977 irrespective of the Schmidt number.

978 To conclude, for the values of ξ_0 investigated here, the geometrical characteris-
 979 tics scales R_g , L_Σ and $\mathcal{H}_{\text{rms}}^{-1}$ of the iso-scalar fields can be related to the somehow
 980 more 'usual' characteristic scales of the scalar field: the integral, Corrsin and
 981 Batchelor length-scales, respectively. There thus exists an intimate connection
 982 between the geometrical and hydrodynamic characteristic scales.

983 In the appendix, we plot the local scaling exponent of $\langle(\delta\phi)^2\rangle_{\mathbb{R},\mathbb{E},\Omega}$ when the
 984 separation is made non-dimensional using either R_g (Fig. 20) or $\mathcal{H}_{\text{rms}}^{-1}$ (Fig. 24).
 985 We observe in Fig. 24 that the onset of the fractal scaling range starts at a scale
 986 proportional to $\mathcal{H}_{\text{rms}}^{-1}$. On the other side (Fig. 20), the end of the scaling range
 987 appears at a scale proportional to R_g . Therefore, the inner cutoff of the fractal
 988 range is related to $\mathcal{H}_{\text{rms}}^{-1}$ (and hence η_B) while the outer cutoff is given by R_g (and
 989 hence L_ξ). Note that [Sreenivasan et al. \(1989\)](#) conjectured that for small Schmidt
 990 number, the inner cutoff should be related to the Obukhov-Corrsin length-scale

991 η_{OC} . Our findings indicate that the inner cutoff should better be scaled with the
 992 Batchelor length-scale.

993 A fractal scaling should result in (Sreenivasan *et al.* 1989),

$$994 \quad L_{\text{box}} \Sigma = k_f \left(\frac{R_g}{\mathcal{H}_{\text{rms}}^{-1}} \right)^{D_f - 2}, \quad (4.11)$$

995 where k_f is the fractal prefactor and $L_{\text{box}} = 2\pi$ is used for normalization
 996 as in Shete & de Bruyn Kops (2020). Figure 14(b) portrays the evolution of
 997 surface density Σ with respect to $R_g \mathcal{H}_{\text{rms}}$ for all Péclet numbers. The log-log
 998 representation clearly indicates that a power-law is at play with an exponent in
 999 very close agreement with $D_f = 2.62$ and $D_f = 2.64$ for $\xi_0 = 0$ and $\xi_0 = \xi_{\text{rms}}$
 1000 respectively. Surprisingly, Eq. (4.11) holds even at the lowest Péclet numbers,
 1001 although there is no clear scaling range for $\langle (\delta\phi)^2 \rangle_{\mathbb{R}, \mathbb{E}, \Omega}$. We also note that the
 1002 fractal prefactor k_f in Eq. (4.11) depends on particular the choice of the iso-scalar
 1003 but not on the Péclet number.

1004 Expressing R_g and \mathcal{H}_{rms} in terms of L_ξ and η_B in Eq. (4.11) yields:

$$1005 \quad \Sigma \sim \left(C_\epsilon \frac{L_\xi}{L_t} Pe_{\lambda_\xi}^{\frac{3}{2}} Sc^{-1} \right)^{D_f - 2} \quad (4.12)$$

1006 where C_ϵ is the kinetic energy dissipation constant and Pe_λ is the Taylor based
 1007 Péclet number $Pe_\lambda = R_\lambda Sc$. When expressed in terms of Pe_{λ_ξ} , Eq. (4.12) writes:

$$1008 \quad \Sigma \sim \left(C_\epsilon \frac{L_\xi}{L_t} R^{-3/4} Pe_{\lambda_\xi}^{\frac{3}{2}} Sc^{-1/4} \right)^{D_f - 2} \quad (4.13)$$

1009 Eq. (4.12) indicates that for $Sc = 1$, and further omitting the dependence of C_ϵ
 1010 and L_ξ/L_t to R_λ , the surface density of iso-scalars Σ should grow as $Pe_{\lambda_\xi}^{\frac{3}{2}(D_f - 2)} =$
 1011 $Pe_{\lambda_\xi}^{\frac{3}{2}(D_f - 2)} = R_\lambda^{\frac{3}{2}(D_f - 2)}$. If $D_f = 8/3$, we have $\Sigma \sim Pe_\lambda \sim Pe_{\lambda_\xi} \sim R_\lambda$ while
 1012 $D_f = 7/3$ leads to $\Sigma \sim Pe_\lambda^{1/2} \sim Pe_{\lambda_\xi}^{1/2} \sim R_\lambda^{1/2}$. The Pe_λ scaling derived in
 1013 Eq. (4.12) is different from the one observed by Shete & de Bruyn Kops (2020)
 1014 in a configuration similar to the present one (although the velocity forcing and
 1015 dealiasing procedures were different). They obtained that $\Sigma \sim Pe_\lambda^{1/2}$ over an
 1016 impressive range of Péclet numbers. This result was obtained by averaging the
 1017 surface areas over 20 different iso-levels covering the range of scalar fluctuations.
 1018 Since the fractal dimension D_f is known to vary for different iso-levels (Iyer *et al.*
 1019 2020), lumping together the values for 20 iso-surface areas could have resulted in
 1020 a different scaling with respect to the Péclet number. Further investigations are
 1021 required to confirm whether or not Eq. (4.12) holds true for the data of Shete &
 1022 de Bruyn Kops (2020).

1023

4.7. Decaying turbulence

1024 We now proceed to the analysis of the scale-by-scale budgets in decaying turbu-
 1025 lence. In this situation, the time derivative term in Eq. (2.15) contributes to the
 1026 budget. We consider two cases where the production term associated with the
 1027 imposed mean scalar gradient is either retained or deactivated. For each situation,
 1028 a Schmidt number of 1.0 and 0.2 is analyzed.

1029 We start with the case where the kinetic energy is freely decaying but the
 1030 imposed mean scalar gradient is maintained. Therefore, the time derivative term

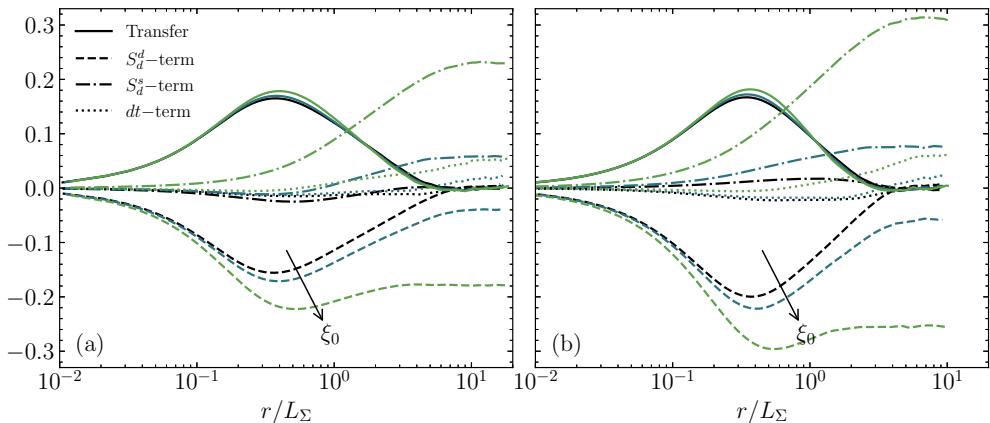


Figure 15: Budget of $\langle(\delta\phi)^2\rangle_{\mathbb{E},\mathbb{R},\Omega}$ with increasing ξ_0 in decaying turbulence with imposed mean scalar gradient. Full lines: transfer term, dashed lines: S_d^d -term, dash-dotted lines: S_d^s -term, dotted lines: dt -term. All contributions are normalized by $2\mathbb{K}_T\langle\phi\rangle_{\mathbb{E},\mathbb{R}}(1 - \langle\phi\rangle_{\mathbb{E},\mathbb{R}})$ while the separation r is normalized by L_Σ . (a) $Sc = 1$, (b) $Sc = 0.2$. Three values of $\xi_0 = 0, 0.5\xi_{rms}, \xi_{rms}$ are displayed from dark to light.

1031 in Eq. (2.15) is not zero but the displacement speed S_d has a source term
 1032 contribution S_d^s . The different terms of the scale-by-scale budgets are presented
 1033 in Fig. 15 for the two Schmidt number values and for three different values of ξ_0
 1034 from 0 to ξ_{rms} . We observe that when normalized by $2\mathbb{K}_T\langle\phi\rangle_{\mathbb{E},\mathbb{R}}(1 - \langle\phi\rangle_{\mathbb{E},\mathbb{R}})$ and
 1035 L_Σ , the transfer term is almost independent of the choice of the iso-scalar value.
 1036 This means that the different iso-surfaces experience the same scale dependent
 1037 turbulent straining. The Schmidt number variations are similar to the one already
 1038 documented in the previous section. The contribution due to scalar diffusion is
 1039 always negative which means that the restoration effect acts in counteracting the
 1040 turbulent straining. At large scales, increasing ξ_0 and decreasing Sc is followed by
 1041 a increasing amplitude of the S_d^d -term which is consistent with an increase of S_d
 1042 and D . The term associated with the imposed mean scalar gradient, is positive,
 1043 acts at larger scales and its amplitude increases with ξ_0 . The balance between all
 1044 these terms yields the time variations of $\langle(\delta\phi)^2\rangle_{\mathbb{E},\mathbb{R},\Omega}$. This term has a rather small
 1045 amplitude compared to the three others. We note however that at large scales
 1046 and for $\xi_0 > 0$, the time variations of $\langle(\delta\phi)^2\rangle_{\mathbb{E},\mathbb{R},\Omega}$ are positive meaning that the
 1047 volume $\langle\phi\rangle_{\mathbb{E},\mathbb{R}}$ tends to increase with time. This is consistent with the observation
 1048 that in decaying turbulence in presence of an imposed mean scalar gradient, the
 1049 variance of ξ grows in time. We also note that at large scales, all terms of the
 1050 budget tend to zero when $\xi_0 = 0$ meaning that the volume $\langle\phi\rangle_{\mathbb{E},\mathbb{R}}$ for $\xi_0 = 0$ is
 1051 conserved.

1052 Deactivating the source term leads to $S_d^s = 0$. In this situation, the time
 1053 variations of $\langle(\delta\phi)^2\rangle_{\mathbb{E},\mathbb{R},\Omega}$ is due to the unbalance between the transfer term and
 1054 diffusion term. Results for $Sc = 1.0$ and 0.2 and for $\xi_0 = 0, 0.5\xi_{rms}$ and ξ_{rms} are
 1055 presented in Fig. 16. Here again, we observe that the particular choice of ξ_0 does
 1056 not change drastically the transfer term when the latter is scaled in terms of
 1057 $2\mathbb{K}_T\langle\phi\rangle_{\mathbb{E},\mathbb{R}}(1 - \langle\phi\rangle_{\mathbb{E},\mathbb{R}})$. Influence of ξ_0 and Sc are much more perceptible on the
 1058 diffusion term and consequently the time derivative term. There is a systematic
 1059 decrease of the S_d^d -term at both intermediate and large scales when ξ_0 increases

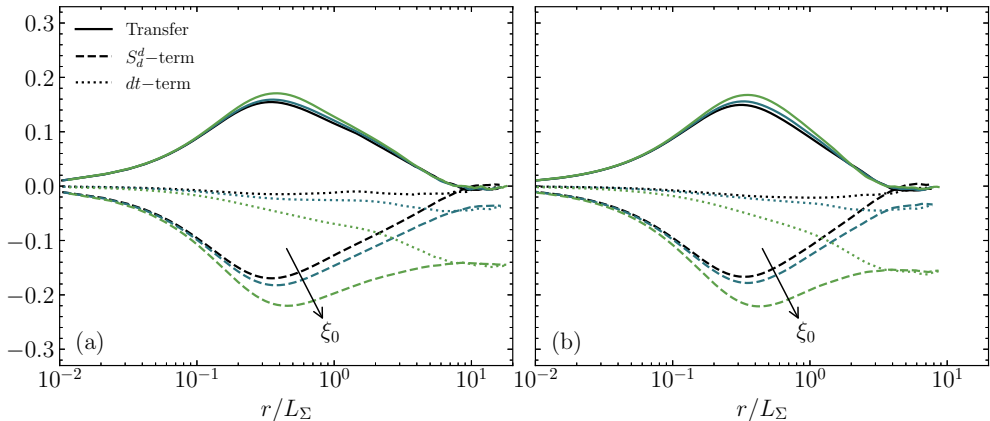


Figure 16: Budget of $\langle(\delta\phi)^2\rangle_{\mathbb{E},\mathbb{R},\Omega}$ with increasing ξ_0 in decaying turbulence without imposed mean scalar gradient. Full lines: transfer term, dashed lines: S_d^d -term, dash-dotted lines: S_d^s -term, dotted lines: dt -term. All contributions are normalized by $2\mathbb{K}_T\langle\phi\rangle_{\mathbb{E},\mathbb{R}}(1 - \langle\phi\rangle_{\mathbb{E},\mathbb{R}})$ while the separation r is normalized by L_Σ . (a) $Sc = 1$, (b) $Sc = 0.2$. Three values of $\xi_0 = 0, 0.5\xi_{\text{rms}}, \xi_{\text{rms}}$ are displayed from dark to light.

1060 from 0 to ξ_{rms} . We also observe that the slope of the time derivative term at
 1061 small scales is negative meaning that the surface density is decreasing in time.
 1062 At large scales, the unsteady term is negative, asymptotes the diffusion term and
 1063 increases in amplitude with ξ_0 and Sc .

1064 In summary, forced and decaying turbulence share some common behaviors:

- 1065 • The transfer term is positive in both case, meaning that turbulent straining
 1066 acts in increasing the morphological content of iso-scalar sets.
- 1067 • The contribution due to diffusion (the S_d^d -term) is always negative. It thus
 1068 plays a restoration effect that counteracts the effect of turbulent straining.
- 1069 • Increasing scalar diffusivity (decreasing Sc) always leads to a decrease of
 1070 the iso-scalar morphological content. This is mainly due to the above-mentioned
 1071 restoration effect, where the latter increases with D , which is consistent with the
 1072 assumption $S_d^d \approx 2D\mathcal{H}$.

1073 In contrast, there are key differences between forced and isotropic turbulence
 1074 which are summarized below:

- 1075 • In forced stationary turbulence, the time derivative term in Eq. (2.15) is by
 1076 definition zero for all scales.
- 1077 • In decaying situations, depending on the iso-scalar value and the presence or
 1078 absence of mean scalar gradient, the time derivative term can be either positive
 1079 or negative as detailed below:
 - 1080 ◦ In decaying turbulence, in absence of mean scalar gradient, the time deriva-
 1081 tive term is systematically negative, meaning that both the surface density
 1082 and iso-scalar volume are decreasing.
 - 1083 ◦ In presence of mean scalar gradient, the time derivative term can be either
 1084 positive or negative depending on the iso-scalar value.

1085 **5. Conclusion**

1086 A new theory is proposed to characterize the time evolution of iso-scalar volumes.
 1087 It is based on the two-point transport equation of the phase indicator field.
 1088 The main analytical tools that are convoked emanate from two, apparently
 1089 disconnected, fields of physics. On the one hand, using known analytical results
 1090 from the field of heterogeneous media and fractal aggregates, we have shown that
 1091 two-point statistics of the phase indicator allow some integral geometric quantities
 1092 (volume, surface area and curvatures) and some morphological characteristics
 1093 (reach, inner/outer cutoff, fractal dimension) to be measured. On the other hand,
 1094 we invoked the machinery of the scale-by-scale budgets which is adapted to
 1095 the kinematic equation of iso-volumes. Combining such two approaches allows
 1096 not only the geometry, morphology and topology of the fluid structures to be
 1097 assessed; it also embeds their scale/space/time evolution. As a consequence, we
 1098 like referring to this framework as a morphodynamical theory. It also naturally
 1099 degenerates to the transport equations for the volume and surface density in the
 1100 limit of large and small scales, respectively, thereby offering promising perspec-
 1101 tives for modelling either scalar mixing (Catrakis & Dimotakis 1996), two-phase
 1102 flows (Lebas *et al.* 2009) or combustive flows (Trouvé & Poinso 1994) using a
 1103 volume-surface density approach. The new set of equations derived in the present
 1104 work generalizes some previous analysis by Thiesset *et al.* (2020, 2021). It is now
 1105 possible to cope with diffusive and/or reactive scalars, in presence or absence of
 1106 source terms. All these processes are embedded in the interface displacement
 1107 speed that may possess different contributions and different physical origins
 1108 depending on the flow situation. It is an exact framework and has the potential
 1109 of being applied to different flow variables in different flow situations. Hence, it
 1110 is believed to offer promising perspective to probe the physics of interfaces in a
 1111 broad sense.

1112 In the present work, light is shed on scalar mixing in either forced or decaying
 1113 turbulence using state-of-the-art DNS data covering a large range of Reynolds
 1114 and Schmidt numbers. We paid attention to the correlation between the different
 1115 components of the displacement speed and the mean curvature of the interface.
 1116 It is shown that the tangential diffusion contribution dominates, meaning that,
 1117 as a first approximation, S_d is proportional to the scalar diffusivity D and the
 1118 mean curvature \mathcal{H} . This is a result of major importance which proves that there
 1119 exists an intimate relation between the geometry of interface and some dynamical
 1120 processes such as diffusion. Further, the geometry of the interface at a microscale
 1121 (i.e. at a scale r) has an influence on some macroscopic (i.e. when $r \rightarrow \infty$)
 1122 processes such as the conservation of scalar iso-volumes.

1123 The search for the appropriate similarity variables have shown that there
 1124 exists three important characteristic length-scales for the second-order structure
 1125 function of the phase indicator field.

1126 • The first one corresponds to the inverse of the mean curvature standard
 1127 deviation $\mathcal{H}_{\text{rms}}^{-1}$. This scale together with $\Sigma\mathbb{K}_T$ are the similarity variables at small
 1128 scales up to intermediate scales. The existence of this normalizing scale is justified
 1129 by the small-scale expansion of $\langle(\delta\phi)^2\rangle_{\mathbb{E},\mathbb{R},\Omega}$ (Eq. (2.17)). We also discovered that
 1130 the scale beyond which a fractal scaling range starts to appear is proportional
 1131 to $\mathcal{H}_{\text{rms}}^{-1}$ suggesting that the inner cutoff is related $\mathcal{H}_{\text{rms}}^{-1}$. It was also observed
 1132 that $\mathcal{H}_{\text{rms}}\eta_B = \text{const.}$ over the range of Péclet numbers investigated here. An
 1133 explanation for this observation when $\mathbb{K}_T \sim \mathbb{K}_C \sim \tau_\eta^{-1}$ is provided. However, the

1134 proportionality between $\mathcal{H}_{\text{rms}}^{-1}$ and η_B is a likely more general result which holds
 1135 even at low Péclet numbers. This means that the assumption $\mathbb{K}_T \sim \mathbb{K}_C \sim \tau_\eta^{-1}$ is
 1136 not likely to be a necessary condition.

1137 • The second set of normalizing scales can be expressed in terms of surface
 1138 density Σ and volume $\langle \phi \rangle_{\mathbb{R}, \mathbb{E}}$. They arise very naturally from the small-scale
 1139 expansion (Eq. (2.17)) and the large scale limit of $\langle (\delta\phi)^2 \rangle_{\mathbb{E}, \mathbb{R}, \Omega}$, respectively. It was
 1140 previously identified by Thiesset *et al.* (2020). These quantities are appropriate
 1141 for normalizing two-point statistics in the limit of either small and large scale.
 1142 It was found that, for the range of ξ_0 investigated here, L_Σ is proportional to
 1143 the Corrsin length-scale, in agreement with previous analysis based on the Rice's
 1144 theorem.

1145 • The last set of normalizing scales is provided by R_g , the radius of gyration
 1146 and the strain felt at scale R_g , viz. $\langle k \rangle^{1/2}/R_g$. These are the characteristic
 1147 quantities of the large scale processes. It is found that R_g is proportional to the
 1148 integral length-scale of the scalar field L_ξ . The local scaling exponent of $\langle \phi \rangle_{\mathbb{R}, \mathbb{E}}$
 1149 was further shown to depart from a constant scaling exponent at a scale similar
 1150 to R_g . Hence, the outer cutoff is related to R_g and thus L_ξ .

1151 At sufficiently large R_λ , the distribution $\langle (\delta\phi)^2 \rangle_{\mathbb{E}, \mathbb{R}, \Omega}$ was shown to behave
 1152 according to a power law in the intermediate range of scales. The corresponding
 1153 scaling exponent is related to the fractal dimension that is found to be close
 1154 to 8/3 in agreement with the theoretical analysis of Constantin *et al.* (1991);
 1155 Mandelbrot (1975); Grossmann & Lohse (1994). The fractal dimension together
 1156 with the inner and outer cutoff allows the surface area of the iso-scalars to be
 1157 estimated. Surprisingly, it was observed that this applies even at low Péclet where
 1158 a fractal scaling range is not likely to hold. The transfer term was also shown to
 1159 possess a scaling range, and we provided the value for the scaling exponent by
 1160 resorting to the closure proposed by de Divitiis (2014, 2016, 2020).

1161 The effect of Reynolds and Schmidt number on the different contributions of the
 1162 stretch rate, viz. the strain rate \mathbb{K}_T , the curvature term associated with diffusive
 1163 effect \mathbb{K}_C^d and the curvature term associated with the forcing \mathbb{K}_C^s is explored. It
 1164 is shown that in forced turbulence with an imposed mean scalar gradient, \mathbb{K}_T is
 1165 positive and compensated by both \mathbb{K}_C^d , which is systematically negative, and \mathbb{K}_C^s
 1166 whose sign depends on the iso-scalar value ξ_0 . In the limit of large R_λ , $\mathbb{K}_C^s \rightarrow 0$
 1167 which proves that the geometry of the interface at the smallest scales tends to be
 1168 independent of the type of forcing. The closure of de Divitiis (2014, 2016, 2020)
 1169 was also invoked to prove that \mathbb{K}_T is proportional to τ_η^{-1} .

1170 Finally, we examined the scale distribution of the different terms of the scale-
 1171 by-scale budget, see Eq. (2.15), for different values of R_λ and Sc , in either forced
 1172 or decaying turbulence. It was shown that the transfer term, which measures the
 1173 interaction between the interface and velocity field at scale r , is systematically
 1174 positive. This means that turbulence acts in increasing the morphological content
 1175 of the interface. On the other hand, the term associated with the diffusive
 1176 component of the displacement speed is always negative, meaning that diffusion
 1177 acts in counteracting turbulent straining through a so-called kinematic restoration
 1178 effect. Although this conclusion appears rather intuitive, it is here significantly
 1179 strengthened by a quantitative and analytical framework based on two-point
 1180 statistical equations. The last term is due to the forcing imposed by a mean
 1181 scalar gradient. The latter can be either positive or negative depending on the
 1182 iso-scalar value. This term tends to zero in the small and intermediate range of

1183 scales when R_λ increases and its contribution is progressively pushed towards the
 1184 largest scales. This proves again that the geometry of the interface tends to be
 1185 independent of the type of forcing at sufficiently large R_λ . We also explored the
 1186 case of decaying turbulence, with and without the imposed scalar gradient. We
 1187 showed that the transfer term remains roughly independent to the iso-scalar value
 1188 meaning that the different iso-scalars experience the same turbulent straining.
 1189 The time-evolution of the phase indicator structure function is thus given by
 1190 the balance between the S_d^d and S_d^s terms. Without the imposed mean gradient,
 1191 the unsteady term was found negative meaning that both the surface density,
 1192 morphological content and volume are decreasing during the decay.

1193 The present work opens up attractive perspectives. First, given the amount
 1194 of computational time needed to post-process this database, we have restricted
 1195 ourselves to a limited range of iso-scalar values. A more systematic study of the
 1196 evolution of $\langle(\delta\phi)^2\rangle_{\mathbb{E},\mathbb{R},\Omega}$ and the different terms of the budget with respect to ξ_0
 1197 is now needed. Second, we have explored the effect of Reynolds and Schmidt
 1198 numbers independently. However, our database does not address the case of
 1199 varying Sc and R_λ while keeping the Péclet number $Pe_{\lambda\xi}$ constant. This would
 1200 allow one to conclude about the similarity of two-point statistics with respect
 1201 to the Péclet number. Third, the flow configuration explored here is statistically
 1202 homogeneous and hence, the scale-by-scale budgets are independent on the flow
 1203 position. The next step for addressing some complex flow configurations will thus
 1204 consist in better characterizing the effect of inhomogeneities and anisotropy.

1205 We have focused here only on Schmidt numbers $Sc \leq 1$. For very high Schmidt
 1206 numbers, we expect results to be quite different. Indeed, for $Sc \gg 1$ and $R_\lambda \gg 1$,
 1207 scalar spectra are expected to reveal two distinct scaling ranges: the inertial-
 1208 convective scaling range with an exponent close to $-5/3$ which extends up to the
 1209 Kolmogorov scale followed by a viscous-convective scaling range with an exponent
 1210 of -1 which ends at the Batchelor scale. Consequently, for high Schmidt numbers,
 1211 we expect the structure function of ϕ to reveal two distinct scaling ranges: the
 1212 first with an exponent of $3 - D_{f,1}$ which corresponds to the inertial-convective
 1213 range, preceded by a scaling range with an exponent $3 - D_{f,2}$ corresponding to
 1214 the viscous-convective range. At very small-scales, the local scaling exponent of
 1215 $\langle(\delta\phi)^2\rangle_{\mathbb{R},\Omega}$ should approach 1 as shown by Eq. (2.17). Therefore, it would be of
 1216 great interest in this context to measure the values for $D_{f,1}$ and $D_{f,2}$ together with
 1217 their respective inner and outer cutoff length-scales using the present framework.
 1218 However, numerical data at high Schmidt numbers are particularly challenging
 1219 to obtain since one faces numerical issues to achieve both high Reynolds (for
 1220 the inertial-convective range to establish) and high Schmidt numbers (for the
 1221 diffusive-convective range to be sufficiently large). We hope that in the future,
 1222 such a dataset will be available so that to test the ability of the present framework
 1223 to infer the scaling and the terms of the transport equation of $\langle(\delta\phi)^2\rangle_{\mathbb{R},\mathbb{E}}$.

1224 Finally, besides turbulent mixing, the present mathematical framework should
 1225 now be harnessed for giving insights into the physics of other type of interfaces
 1226 such as reacting fronts, turbulent/non-turbulent layers, or two-phase flows in
 1227 presence of evaporation.

1228 Acknowledgements

1229 We are thankful to A. Poux, research engineer at CORIA laboratory for his
 1230 contribution to the pyarcher project. We are also grateful to Marc Massot for

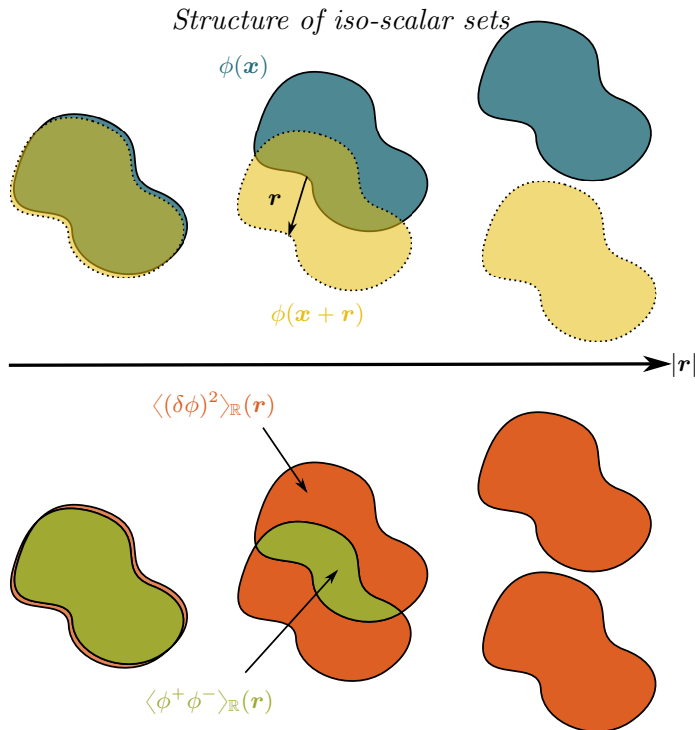


Figure 17: Graphical representation of the spatially averaged phase indicator correlation function (green) and structure function (orange) given $\phi(\mathbf{x})$ (blue) and $\phi(\mathbf{x} + \mathbf{r})$ (yellow).

1231 sharing the routines allowing us to compute the surface area and curvatures
 1232 of iso-level-set surfaces. These are now available through the project [Mercur\(v\)e](#).
 1233 The authors gratefully acknowledge computing time granted by the Gauss-Center
 1234 for Supercomputing (GCS) and the Juelich-Aachen Research Alliance (JARA) on
 1235 the supercomputers JUQUEEN and JURECA at Juelich Supercomputing Center
 1236 (Germany). We are thankful to the CRIANN (Centre Régional Informatique
 1237 et d'Applications Numériques de Normandie) and the GENCI TGCC Joliot
 1238 Curie/Irene systems (projects 2018002, 2016003 and A0092A12065) for providing
 1239 us additional computation time. FT also benefited from the financial support
 1240 from the INSIS institute of the CNRS and the CORIA laboratory. MG received
 1241 financial support within the project EMCO2RE.

1242 Declaration of Interests

1243 The authors report no conflict of interest.

1244 Appendix A. Interpretation of $\langle (\delta\phi)^2 \rangle_{\mathbb{R}}$ in terms of boolean operations

1245 We here reproduce the reasoning of [Thiesset et al. \(2021\)](#) which allows interpret-
 1246 ing $\langle (\delta\phi)^2 \rangle_{\mathbb{R}}$ in terms of boolean operations.

1247 Consider the set of points $\{\mathbf{x} \in \mathbb{R} \mid \phi(\mathbf{x}) = 1\}$ and its translated version at a
 1248 distance \mathbf{r} , $\{\mathbf{x} \in \mathbb{R} \mid \phi(\mathbf{x} + \mathbf{r}) = 1\}$. These are displayed as the blue and yellow
 1249 sets in Fig. 17. The spatially averaged correlation function $\langle \phi^+ \phi^- \rangle_{\mathbb{R}}$ then writes
 1250 as the intersection (the convolution) of the sets ϕ^- and ϕ^+ , as represented by

1251 green sets in Fig. 17. Given Eq. (2.10), the spatially averaged structure function
 1252 $\langle(\delta\phi)^2\rangle_{\mathbb{R}}$ is thus given by the volume of $\phi(\mathbf{x})$, plus the volume of $\phi(\mathbf{x} + \mathbf{r})$, minus
 1253 two times the intersection. It thus reads as the disjunctive union (or symmetric
 1254 difference) of ϕ^- and ϕ^+ which is graphically represented by the orange sets in
 1255 Fig. 17.

1256 For small values of the separation vector, one sees that the orange set in Fig. 17
 1257 delineates the contours of the excursion set while for large scales, the disjunctive
 1258 union writes as twice its volume. For intermediate scales, the correlation and
 1259 structure function might depend on the morphology of the structures under hand.
 1260 Therefore, the graphical representation of $\langle(\delta\phi)^2\rangle_{\mathbb{R}}$ in Fig. 17 allows one to easily
 1261 grasp that for small values of the separation $|\mathbf{r}|$, $\langle(\delta\phi)^2\rangle_{\mathbb{R}}$ is proportional to the
 1262 area of the ξ_0 iso-surface, while for large scales, $\langle(\delta\phi)^2\rangle_{\mathbb{R}}$ depends on the volume
 1263 of the excursion set. For intermediate scales, $\langle(\delta\phi)^2\rangle_{\mathbb{R}}$ becomes a morphological
 1264 descriptor where the scale r plays the role of a morphological parameter.

1265 Appendix B. Numerical method for computing $\langle\phi^- S_d^+ |\nabla_{\mathbf{x}}\phi|^+\rangle_{\mathbb{R}}$

1266 The additional source term in Eq. (2.12) highlights the correlation of ϕ with
 1267 $S_d |\nabla_{\mathbf{x}}\phi|$. Before describing the procedure we employed for computing this term,
 1268 we first recall available methods to infer numerically the surface-bulk correlation
 1269 $\langle\phi^- |\nabla_{\mathbf{x}}\phi|^+\rangle_{\mathbb{R}}$. One method is presented in Seaton & Glandt (1986) which is
 1270 also briefly described in Ma & Torquato (2018). It consists in computing the
 1271 correlation function $\langle\phi_{\epsilon}^+ \phi_{\epsilon}^-\rangle_{\mathbb{R}}(r, \epsilon)$ of the fields $\phi_{\epsilon}(\mathbf{x})$ which denotes either the
 1272 dilated (when the scale $\epsilon > 0$) or eroded (when the scale $\epsilon < 0$) version of $\phi(\mathbf{x})$.
 1273 Here the eroded/dilated objects can simply be defined from the excursion set, i.e.
 1274 $\phi(\mathbf{x}, \epsilon) = H(\Upsilon(\mathbf{x}) - \epsilon)$, where $\Upsilon(\mathbf{x})$ is the level-set field of the iso-scalar under
 1275 consideration. Then, the surface-bulk correlation function can be proven to be
 1276 equal to

$$1277 \quad \langle\phi^- |\nabla_{\mathbf{x}}\phi|^+\rangle_{\mathbb{R}} = \lim_{\epsilon \rightarrow 0} \frac{1}{2} \frac{\langle\phi_{\epsilon}^+ \phi_{\epsilon}^-\rangle_{\mathbb{R}}(r, \epsilon)}{\epsilon} \quad (\text{B } 1)$$

1278 Numerically, this translates into

$$1279 \quad \langle\phi^- |\nabla_{\mathbf{x}}\phi|^+\rangle_{\mathbb{R}} = \frac{\langle\phi_{\epsilon}^+ \phi_{\epsilon}^-\rangle_{\mathbb{R}}(r, \epsilon) - \langle\phi_{\epsilon}^+ \phi_{\epsilon}^-\rangle_{\mathbb{R}}(r, -\epsilon)}{4\epsilon}, \quad (\text{B } 2)$$

1280 where ϵ should be chosen sufficiently small for the eroded/dilated sets remain
 1281 topologically equivalent to the actual set. In practice, we found that when ϵ
 1282 remains in the range $2dx \leq \epsilon \leq 4dx$, results are very similar and the surface-bulk
 1283 correlation function is in very good agreement with the theoretical limits at large
 1284 and small scales.

1285 The method for computing $\langle\phi^- S_d^+ |\nabla_{\mathbf{x}}\phi|^+\rangle_{\mathbb{R}}$ is somehow similar. It relies on
 1286 the idea that one can define a local dilatation/erosion scale that depends on local
 1287 values of S_d . At a fictive time $t + \tau$, the level-set field will be given by $\Upsilon(\mathbf{x}, \tau) + S_d \tau$
 1288 while the one obtained at time $t - \tau$ is $\Upsilon(\mathbf{x}, -\tau) - S_d \tau$. $S_d \tau$ plays here the same
 1289 role as ϵ which thus corresponds to the special case where $S_d = \text{const}$. Then, one
 1290 can compute $\langle\phi^- S_d^+ |\nabla_{\mathbf{x}}\phi|^+\rangle_{\mathbb{R}}$ as

$$1291 \quad \langle\phi^- S_d^+ |\nabla_{\mathbf{x}}\phi|^+\rangle_{\mathbb{R}} = \lim_{\tau \rightarrow 0} \frac{1}{2} \frac{\langle\phi_{\tau}^+ \phi_{\tau}^-\rangle_{\mathbb{R}}(r, \tau)}{\tau} \quad (\text{B } 3)$$

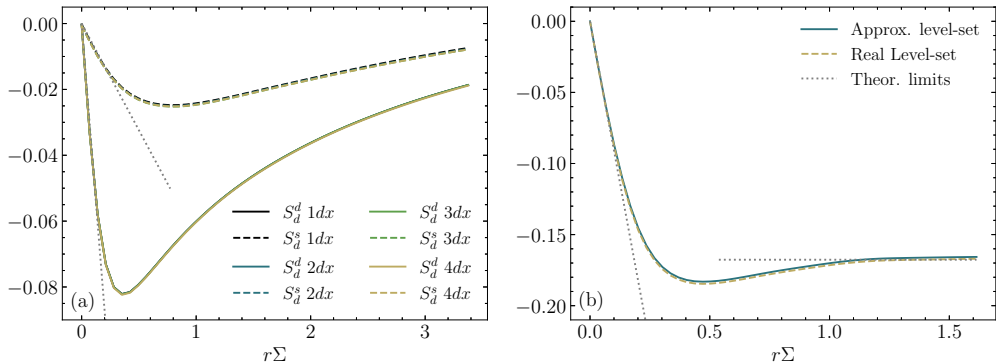


Figure 18: (a) Comparison of the spatially and angularly averaged S_d^i -terms for different values of τ , from $\max|S_d|\tau = 1$ to $\max|S_d|\tau = 4dx$. Case F0 $S_c = 1.0, \xi_0 = 0$. (b) Spatially and angularly averaged S_d^i -term as estimated from the level-set or its approximation using Eq. (B 5). Case T0 $S_c = 1.0, \xi_0 = \xi_{rms}$. In (a) and (b), the S_d^i -terms are normalized by \mathbb{K}_T and the grey dotted lines represent the theoretical asymptotic limits at large and small scales.

1292 or numerically

$$1293 \quad \langle \phi^- S_d^+ |\nabla_{\mathbf{x}} \phi|^+ \rangle_{\mathbb{R}} = \frac{\langle \phi_{\tau}^+ \phi_{\tau}^- \rangle_{\mathbb{R}}(r, \tau) - \langle \phi_{\tau}^+ \phi_{\tau}^- \rangle_{\mathbb{R}}(r, -\tau)}{4\tau} \quad (\text{B } 4)$$

1294 where $\phi_{\tau}(\mathbf{x}) = H(\Upsilon(\mathbf{x}) - S_d\tau)$. Here again, τ should be chosen sufficiently small
 1295 for the dilated/eroded system to remain topologically equivalent to the original
 1296 set. Elaborating on the same reasoning as for ϵ , we have chosen τ in such a way
 1297 that $\max(|S_d|\tau)$ remains of few dx . Fig. 18(a) displays the S_d -term for different
 1298 values of $\max(|S_d|\tau)$ ranging from 1 to $4dx$. We considered the forced turbulence,
 1299 forced scalar case (F0- $S_c = 1.0$) for which S_d is constituted of both a diffusion
 1300 component S_d^d and a source component S_d^s . Results show that the computed
 1301 S_d -term is identical irrespective of the chosen value for τ . They also follow the
 1302 expected asymptotic limit at small scales. Throughout the present study, we have
 1303 chosen $\max(|S_d|\tau) = 3dx$.

1304 Instead of the level-set function Υ , whose computation from our data might be
 1305 particularly expensive, we have used the following approximation of the level-set
 1306 in the vicinity of ξ_0 :

$$1307 \quad \Upsilon(\mathbf{x}) = \frac{\xi(\mathbf{x}) - \xi_0}{|\nabla_{\mathbf{x}} \xi|(\mathbf{x})} \quad (\text{B } 5)$$

1308 We have compared the results obtained for the S_d -term by using a level-set field
 1309 or the ansatz given by Eq. (B 5). The level-set field is computed from the scalar
 1310 field ξ by use of the reinitialization procedure of Sussman *et al.* (1994). We start
 1311 with Eq. (B 5) as an initial condition and the algorithm was run over a sufficiently
 1312 large number of iterations for the level-set to be a signed distance over the whole
 1313 domain. The reinitialization procedure was solved using the two-phase flow solver
 1314 **archer** (Ménard *et al.* 2007).

1315 Results are presented in Fig. 18(b) where the S_d -term estimated either from
 1316 the level-set or its approximation (Eq. (B 5)) are compared. Here we consider
 1317 the T0 dataset where there is no forcing for either the dynamical or scalar field.

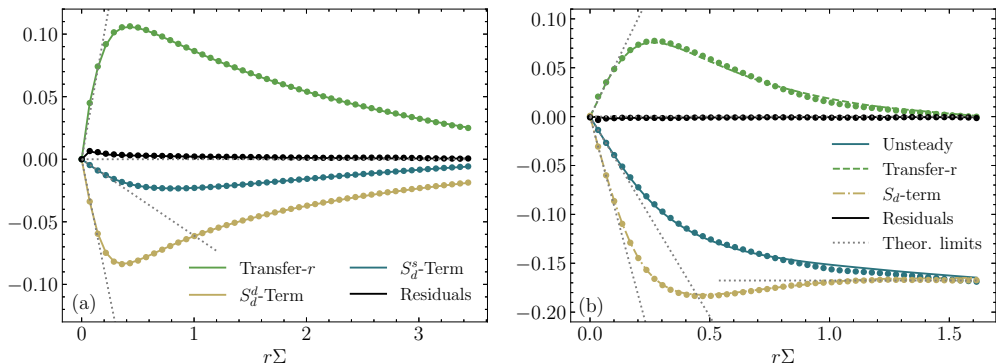


Figure 19: Comparison of the different terms of Eq. (2.15) using either a full (lines) or partial angular average (symbols). (a) F0 $Sc = 1.0$, $\xi_0 = 0$. (b) T0.

1318 No noticeable differences are observed, and both curves compare well with the
 1319 asymptotic theoretical limits at either large and small scales. This proves that
 1320 our method for computing $\langle \phi^- S_d^+ |\nabla_{\mathbf{x}} \phi|^+ \rangle_{\mathbb{R}}$ either from the real or approximated
 1321 level-set is accurate.

1322 Appendix C. Validation of the partial angular average

1323 We checked that results obtained by operating a partial angular average over
 1324 only the three directions r_x, r_y, r_z were similar to the ones issued from the full 3D
 1325 angular average. We considered here the case F0, $Sc = 1.0$, $\xi_0 = 0$ (Fig. 19(a))
 1326 and the T0 case (Fig. 19(b)).

1327 A careful analysis of Fig. 19 reveals that the budget is accurately closed even
 1328 if one employs the partial angular average. Some very slight differences are
 1329 perceptible which are due to a small anisotropy. Note that, in absence of mean
 1330 scalar gradient, the anisotropy should be interpreted as a statistical effect. Indeed,
 1331 the number of structures formed by the scalar excursion set $\xi(\mathbf{x}) > \xi_0$ is typically
 1332 around 50-100 which might not be enough for the two-point statistics of iso-
 1333 volumes to be fully converged. Increasing the number of independent simulations
 1334 will very likely improve the statistical convergence and the degree of isotropy (a
 1335 similar situation was encountered in Thiesset *et al.* (2020)). This effect is however
 1336 considered to be marginal in the present analysis. The small values of the budget
 1337 residuals shown in Fig. 19 is a further evidence of the appropriateness of our post-
 1338 processing procedure for computing the triple correlation $\langle \phi^- S_d^+ |\nabla_{\mathbf{x}} \phi|^+ \rangle_{\mathbb{R}}$. The
 1339 transfer and unsteady term also compare favorably well with their asymptotic
 1340 theoretical expressions at small and large scales. To conclude Fig. 19 provides
 1341 the validation of altogether the theory (Eq. (2.15)), the DNS data and the post-
 1342 processing procedures.

1343 Appendix D. Large-scale similarity

1344 Here, we present the appropriate normalization of two-point statistics in the
 1345 large-scale limit.

1346 In Fig. 20, the second-order structure function $\langle (\delta\phi)^2 \rangle_{\mathbb{E}, \mathbb{R}, \Omega}$ is normalized by
 1347 its asymptotic large-scale value $2\langle \phi \rangle_{\mathbb{E}, \mathbb{R}}(1 - \langle \phi \rangle_{\mathbb{E}, \mathbb{R}})$ while the separation r is
 1348 normalized using the radius of gyration R_g . We observe that the different curves

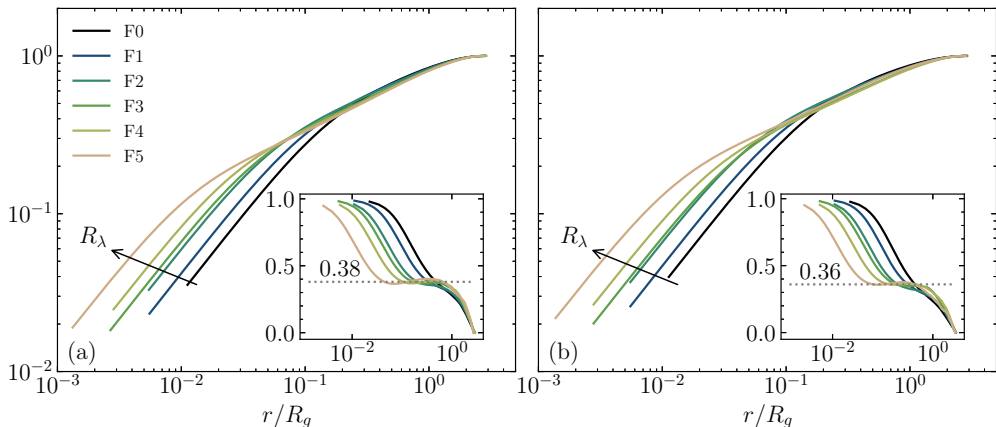


Figure 20: Evolution of $\langle(\delta\phi)^2\rangle_{\mathbb{E},\mathbb{R},\Omega}/2\langle\phi\rangle_{\mathbb{E},\mathbb{R}}(1-\langle\phi\rangle_{\mathbb{E},\mathbb{R}})$ with increasing R_λ . The scale r is normalized by R_g . The local scaling exponent is also plotted in the inset. (a) $\xi_0 = 0$, (b) $\xi_0 = \xi_{\text{rms}}$.

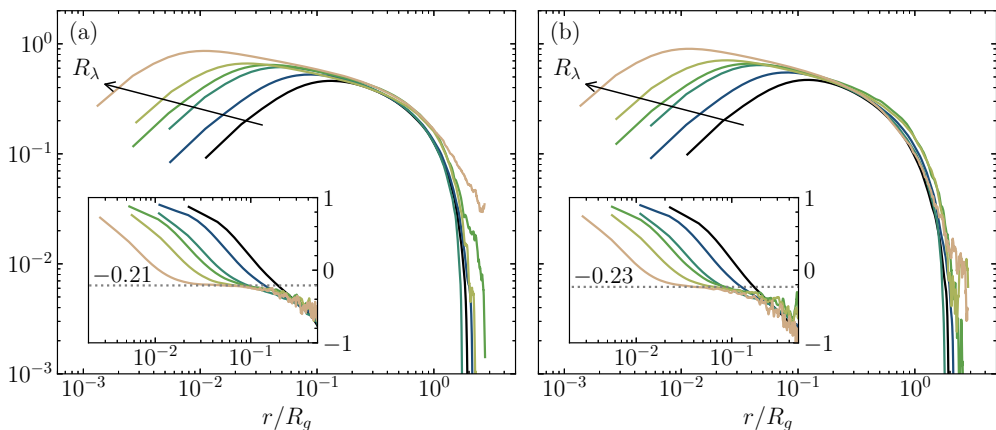


Figure 21: Evolution of the transfer term $-\langle\nabla_r \cdot \langle(\delta\mathbf{u})(\delta\phi)^2\rangle_{\mathbb{E},\mathbb{R}}\rangle_\Omega$ normalized by $2\langle\phi\rangle_{\mathbb{E},\mathbb{R}}(1-\langle\phi\rangle_{\mathbb{E},\mathbb{R}})\langle k\rangle_{\mathbb{E},\mathbb{R}}^{1/2}/R_g$ with increasing R_λ . The local scaling exponent is also plotted in the inset. (a) $\xi_0 = 0$, (b) $\xi_0 = \xi_{\text{rms}}$.

1349 corresponding to the different R_λ collapse well for scales above $r = 0.1R_g$. When
 1350 R_λ increases, the scale distributions widen when R_λ increases and moves towards
 1351 the small scales. It is further worth noting that the fractal scaling ends at a scale
 1352 $r \approx R_g$ which means that R_g plays the role of the outer cutoff of the fractal
 1353 scaling.

1354 We also carried out the same analysis for the transfer term $-\langle\nabla_r \cdot$
 1355 $\langle(\delta\mathbf{u})(\delta\phi)^2\rangle_{\mathbb{E},\mathbb{R}}\rangle_\Omega$ which is normalized using $2\langle\phi\rangle_{\mathbb{E},\mathbb{R}}(1-\langle\phi\rangle_{\mathbb{E},\mathbb{R}})\langle k\rangle_{\mathbb{E},\mathbb{R}}^{1/2}/R_g$. This
 1356 quantity can be understood as the strain acting at a scale R_g . In Fig. 21, we
 1357 observe that this normalization leads to a good collapse of the different curves
 1358 in the large scales $r > 0.1R_g$. For smaller scales, the different curves depart from
 1359 each other and as R_λ increases, the transfer rate term acts over a wider range of
 1360 scales while its peak value moves towards smaller scales.

1361 The different terms of the budget Eq. (2.15), normalized by the same quantities

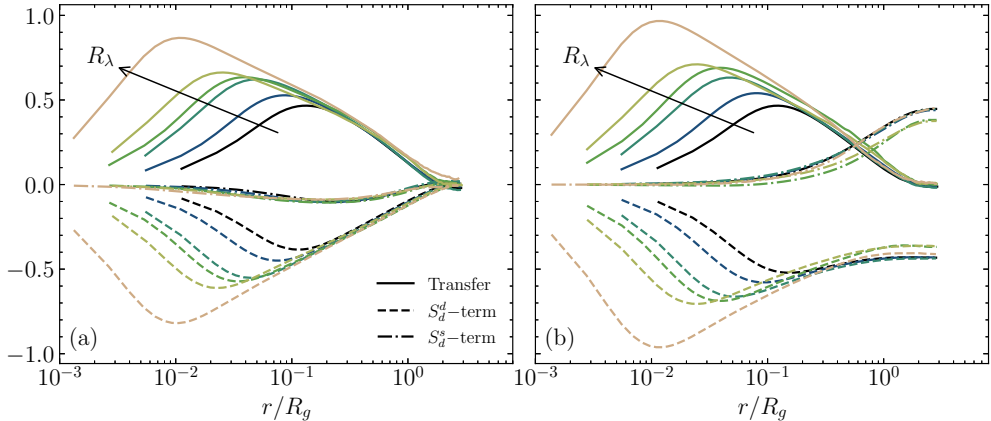


Figure 22: Budget of $\langle(\delta\phi)^2\rangle_{\mathbb{E},\mathbb{R},\Omega}$ with increasing R_λ . Full lines: transfer term, dashed lines: S_d^d -term, dash-dotted lines: S_d^s -term. All contributions are normalized by $2\langle\phi\rangle_{\mathbb{E},\mathbb{R}}(1 - \langle\phi\rangle_{\mathbb{E},\mathbb{R}})\langle k\rangle_{\mathbb{E},\mathbb{R}}^{1/2}/R_g$. (a) $\xi_0 = 0$, (b) $\xi_0 = \xi_{\text{rms}}$.

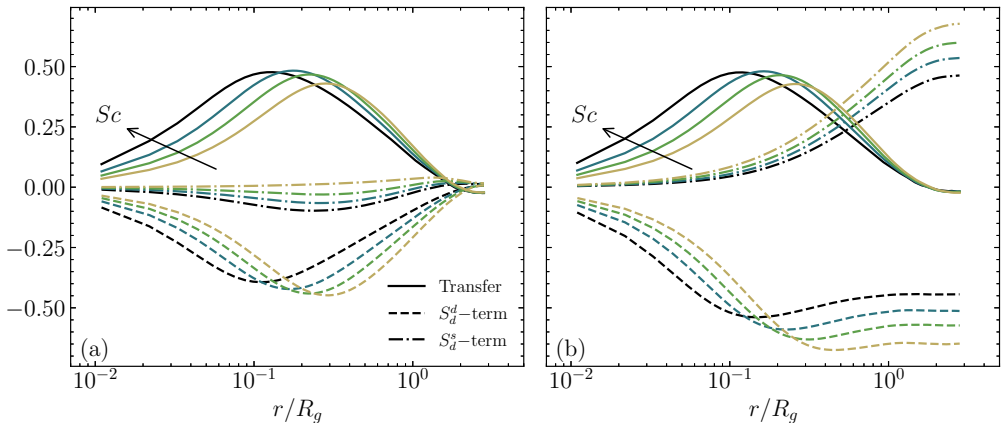


Figure 23: Budget of $\langle(\delta\phi)^2\rangle_{\mathbb{E},\mathbb{R},\Omega}$ with varying Sc . Full lines: transfer term, dashed lines: S_d^d -term, dash-dotted lines: S_d^s -term. All contributions are normalized by $2\langle\phi\rangle_{\mathbb{E},\mathbb{R}}(1 - \langle\phi\rangle_{\mathbb{E},\mathbb{R}})\langle k\rangle_{\mathbb{E},\mathbb{R}}^{1/2}/R_g$. (a) $\xi_0 = 0$, (b) $\xi_0 = \xi_{\text{rms}}$.

1362 obey the same trend, i.e. the different curves collapse relatively well for scales
1363 larger than $0.1R_g$ and move towards smaller scales when R_λ is increased.

1364 We also plot the budget for different Schmidt numbers in Fig. 23 using the
1365 large-scale similarity variables. Noticeable is the shift of the transfer term towards
1366 smaller r/R_g when the Schmidt number increases from 0.1 to 1.0. In contrast,
1367 the diffusive term moves towards larger scales and increases in amplitude. A final
1368 observation of Fig. 23 is that, for $\xi_0 = \xi_{\text{rms}}$, the forcing term due to the mean
1369 scalar gradient increases when Sc decreases from 1.0 to 0.1. For $\xi_0 = 0$, the budget
1370 for $Sc = 0.1$ is composed of the transfer term and diffusive term while the forcing
1371 term is almost negligible.

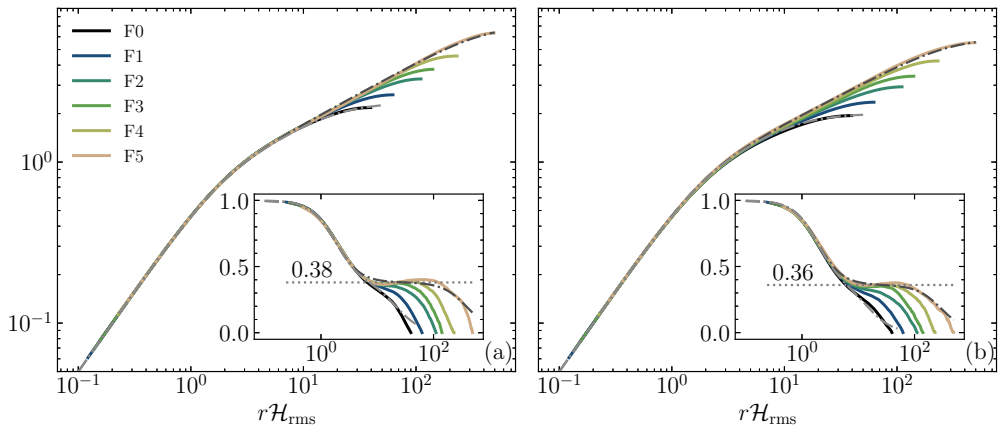


Figure 24: Evolution of $\langle(\delta\phi)^2\rangle_{\mathbb{E},\mathbb{R},\Omega}/\Sigma\mathcal{H}_{\text{rms}}^{-1}$ with increasing R_λ . The scale r is normalized by $\mathcal{H}_{\text{rms}}^{-1}$. The local scaling exponent is also plotted in the inset. (a) $\xi_0 = 0$, (b) $\xi_0 = \xi_{\text{rms}}$. The gray dash-dotted lines denote the Batchelor type parametrization given by Eq. (E1)

1372 Appendix E. Small-scale similarity

1373 We here report the evolution of $\langle(\delta\phi)^2\rangle_{\mathbb{E},\mathbb{R},\Omega}/\Sigma\mathcal{H}_{\text{rms}}^{-1}$ with increasing R_λ while the
 1374 separation r is normalized by $\mathcal{H}_{\text{rms}}^{-1}$. This scenario is tested in Fig. 24, where one
 1375 observes a remarkable degree of similarity for both $\xi_0 = 0$ and $\xi_0 = \xi_{\text{rms}}$. The
 1376 range of scales over which this small scale similarity applies tends to increase with
 1377 increasing R_λ . It is further worth noting that the fractal scaling starts at a scale
 1378 $r \approx 20\mathcal{H}_{\text{rms}}^{-1}$ (see the inset in Fig. 24). Hence, $\mathcal{H}_{\text{rms}}^{-1}$ appears to be proportional the
 1379 inner cutoff of the fractal scaling.

1380 We have observed that $\langle(\delta\phi)^2\rangle_{\mathbb{E},\mathbb{R},\Omega}$ can be well represented by the following
 1381 parametric expression

$$1382 \quad \frac{\langle(\delta\phi)^2\rangle_{\mathbb{E},\mathbb{R},\Omega}}{\Sigma\mathcal{H}_{\text{rms}}^{-1}} = \frac{\tilde{r}}{2} \frac{\left[1 + \left(\frac{\tilde{r}}{\eta_i}\right)^2\right]^{(\zeta-1)/2}}{\left[1 + \left(\frac{\tilde{r}}{\eta_o}\right)^2\right]^{\zeta/2}} \quad (\text{E1})$$

1383 where $\tilde{\bullet} = \bullet/\mathcal{H}_{\text{rms}}^{-1}$. This parametrization is inspired by the one proposed by
 1384 Batchelor (1951) for representing the two-point statistics of the velocity field.
 1385 The main interest in deriving Eq. (E1) is that it allows the fractal exponent ζ ,
 1386 the outer and inner cutoff η_o and η_i to be estimated using non-linear least-square
 1387 curve fitting. By doing so, these parameters are gathered in an unambiguous way
 1388 which does not imply any degree of arbitrariness, notably in the estimation of the
 1389 best range of scaling. This is even more relevant for low to moderate Reynolds
 1390 numbers. A similar approach was employed by Thiesset *et al.* (2016a); Krug *et al.*
 1391 (2017). The appropriateness of this parametric expression is demonstrated in Fig.
 1392 24 at the largest and smallest Reynolds numbers. We obtain $\eta_i \approx 10\eta_B$ which is
 1393 in close agreement with the prediction of Thiesset *et al.* (2016b).

1394 The small-scale similarity is now tested for the transfer term $\langle\nabla_r \cdot$
 1395 $\langle(\delta\mathbf{u})(\delta\phi)^2\rangle_{\mathbb{E},\mathbb{R}}\rangle_\Omega$ which is normalized by $\mathbb{K}_T\Sigma\mathcal{H}_{\text{rms}}^{-1}$ while r is divided by $\mathcal{H}_{\text{rms}}^{-1}$.
 1396 Results are presented in Fig. 25 confirming this small-scale similarity for both

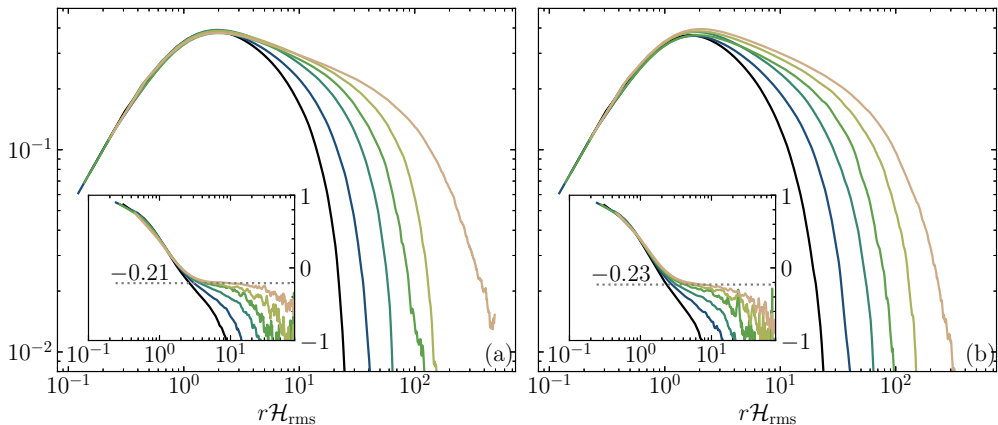


Figure 25: Evolution of the transfer term $-\langle \nabla_r \cdot \langle (\delta \mathbf{u})(\delta \phi)^2 \rangle_{\mathbb{E}, \mathbb{R}} \rangle_{\Omega}$ normalized by $\mathbb{K}_T \Sigma \mathcal{H}_{\text{rms}}^{-1}$ while r is divided by $\mathcal{H}_{\text{rms}}^{-1}$. Dark to light represent F0 to F5. The local scaling exponent is also plotted in the inset. (a) $\xi_0 = 0$, (b) $\xi_0 = \xi_{\text{rms}}$.

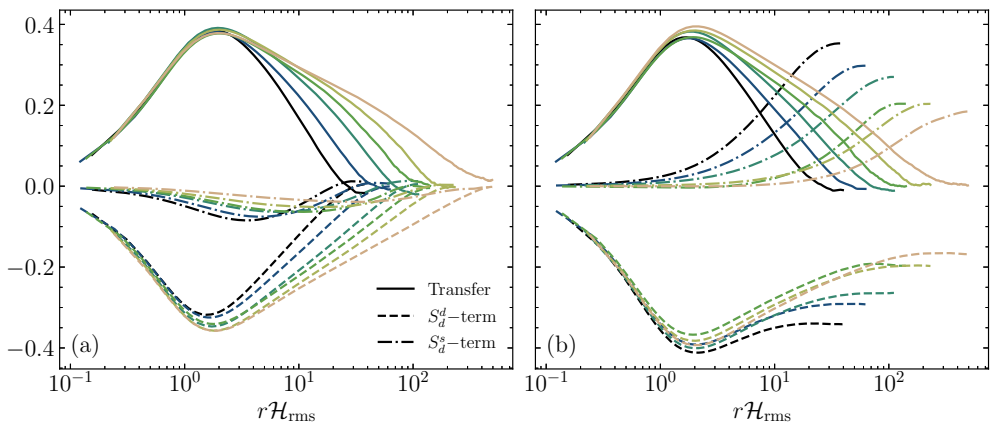


Figure 26: Budget of $\langle (\delta \phi)^2 \rangle_{\mathbb{E}, \mathbb{R}, \Omega}$ with increasing R_λ . Full lines: transfer term, dashed lines: S_d^d -term, dash-dotted lines: S_d^s -term. All contributions are normalized by $\mathbb{K}_T \Sigma \mathcal{H}_{\text{rms}}^{-1}$ while r is divided by $\mathcal{H}_{\text{rms}}^{-1}$. (a) $\xi_0 = 0$, (b) $\xi_0 = \xi_{\text{rms}}$.

1397 $\xi_0 = 0$ and $\xi_0 = \xi_{\text{rms}}$. In particular, we note that it applies, at least up to the
 1398 scale where the transfer term is maximum, and the range of scales over which
 1399 the small scale similarity applies widens with increasing R_λ . The maximum of
 1400 the transfer term given in terms of $\mathbb{K}_T \Sigma \mathcal{H}_{\text{rms}}^{-1}$ is roughly constant and equals to
 1401 0.38.

1402 The different terms of the budget Eq. (2.15) normalized using the small-
 1403 similarity variables are presented in Fig. 26. Here again, we see that the transfer
 1404 term complies well with a small-scale similarity when plotted using $\mathbb{K}_T \Sigma \mathcal{H}_{\text{rms}}^{-1}$ and
 1405 $\mathcal{H}_{\text{rms}}^{-1}$ as similarity variables. However, the similarity holds only at the smallest
 1406 scales for the S_d^d -term, where the term associated with S_d^s is negligible. When R_λ
 1407 increases, this term progressively tends to zero thereby leading to a closer degree
 1408 of similarity for the S_d^d -term.

1409 In conclusion, $\mathcal{H}_{\text{rms}}^{-1}$ and $\mathbb{K}_T \Sigma / \mathcal{H}_{\text{rms}}$ play the same role as the Kolmogorov (or

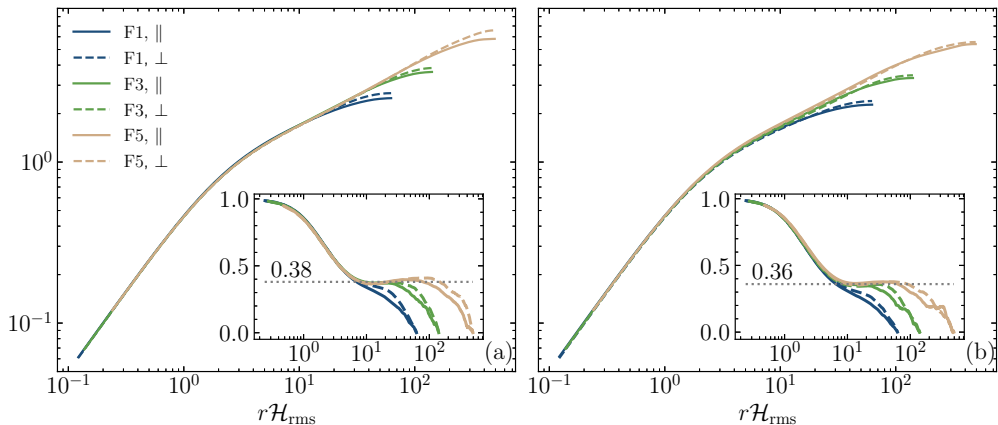


Figure 27: Anisotropy of $\langle(\delta\phi)^2\rangle_{\mathbb{R},\mathbb{E}}$ between the direction parallel (full lines) and perpendicular (dashed lines) to the mean scalar gradient. The insets represent the local scaling exponent. For the sake of clarity only case F1, F3 and F5 are presented. (a) $\xi_0 = 0$, (b) $\xi_0 = \xi_{\text{rms}}$. The small scale similarity variables have been used for normalization.

1410 Batchelor) scales for normalizing the two-point statistics of the velocity (scalar)
 1411 field.

1412 Appendix F. Anisotropy effects due to the mean scalar gradient

1413 The present numerical configuration leads to statistical anisotropy due to the
 1414 presence of a mean scalar gradient G_ξ . Since the latter is active in the y direction,
 1415 two-point statistics are invariant by rotation around the r_y axis. Here, we infer
 1416 anisotropy from the variations of $\langle(\delta\phi)^2\rangle_{\mathbb{R},\mathbb{E}}$ along the different orientations of the
 1417 separation vector \mathbf{r} .

1418 In Fig. 27, we plot $\langle(\delta\phi)^2\rangle_{\mathbb{R},\mathbb{E}}$ along the direction parallel and perpendicular
 1419 to the mean scalar gradient. The parallel direction corresponds to r_y while the
 1420 contributions along r_x and r_z were averaged because of axisymmetry. We observe
 1421 that the curves corresponding to the parallel and perpendicular directions collapse
 1422 at small up to intermediate scales, meaning that the second-order statistics of ϕ
 1423 are locally isotropic. The previously discussed scaling with respect to \mathcal{H}_{rms} (and
 1424 Σ) holds. The scaling exponent remains the same irrespective of the orientation of
 1425 the separation vector \mathbf{r} . This means that the estimation of the fractal dimension
 1426 of the present iso-scalar surfaces is quite robust and is not affected by the mean
 1427 scalar gradient. Differences between parallel and perpendicular directions (viz.
 1428 anisotropy) are perceptible only at the end of the scaling range and at large
 1429 scales. It is seen that the scaling range is systematically wider in the direction
 1430 perpendicular to the mean scalar gradient.

1431 Appendix G. Estimation of statistical errors

1432 We here address the question of statistical errors. We attribute such errors to a
 1433 lack of statistical convergence. For the forced turbulence cases explored here, any
 1434 spatially averaged quantity $\langle\bullet\rangle_{\mathbb{R}}$ is also averaged over M independent snapshots
 1435 which constitute our ensemble \mathbb{E} .

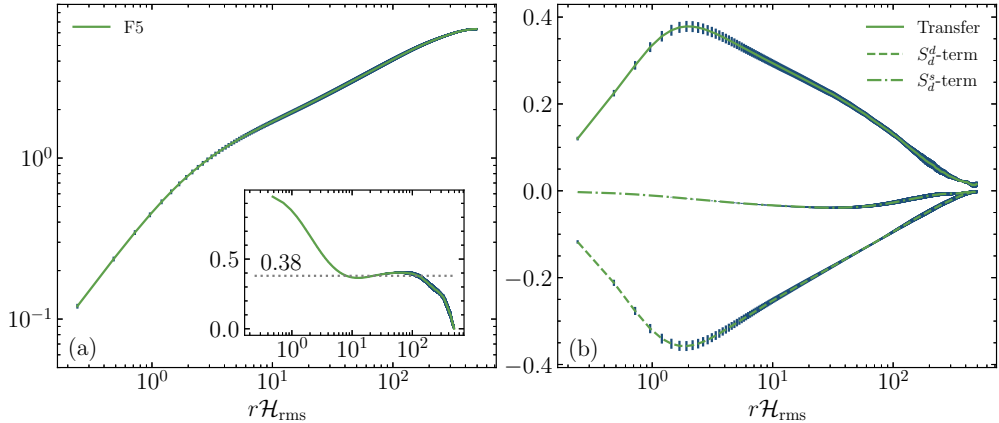


Figure 28: Statistical errors for case F5. Error bars for each quantity $\langle \bullet \rangle_{\mathbb{R},\mathbb{E}}$ correspond to $\bullet_{\text{rms}}/\sqrt{M}$. (a) $\langle(\delta\phi)^2\rangle_{\mathbb{R},\mathbb{E}}$ and its local scaling exponent (inset), (b) the different terms of the budget.

1436 The statistical error on the calculation of the mean $\langle \bullet \rangle_{\mathbb{R},\mathbb{E}}$ is then computed
 1437 from $\bullet_{\text{rms}}/\sqrt{M}$ where \bullet_{rms} is the standard deviation computed from M snapshots.
 1438 We repeated this for $\langle(\delta\phi^2)\rangle_{\mathbb{R}}$, its scaling exponent, and the different terms of its
 1439 transport equation.

1440 Case F5 is the most prone to numerical errors since it is the one for which we
 1441 dispose of the smallest number of snapshots ($M = 6$, see Table 1). Hence, we
 1442 infer errors for this particular case only.

1443 Statistical errors are displayed in Fig. 28 as the blue error-bars while the mean
 1444 value $\langle \bullet \rangle_{\mathbb{E},\mathbb{R}}$ is plotted as the green curves. We observe that these errors are
 1445 particularly small. The typical statistical errors on each of the plotted quantities
 1446 are 1-2% for $\langle(\delta\phi)^2\rangle_{\mathbb{R},\mathbb{E}}$ and its scaling exponent, and 3-4% for the terms of
 1447 its transport equation. For the other forced cases (F0-F4), statistical errors are
 1448 expected to be smaller. It is thus rather safe to conclude that statistical errors
 1449 are marginal in our study.

REFERENCES

- 1450 ADLER, P. M., JACQUIN, C. G. & QUIBLIER, J. A. 1990 Flow in simulated porous media. *Int.*
 1451 *J. Multiphase Flow* **16** (4), 691–712.
- 1452 ANTONIA, R. A. & ORLANDI, P. 2003 Effect of Schmidt number on small-scale passive scalar
 1453 turbulence. *Appl. Mech. Rev.* **56** (6), 615–632.
- 1454 ARNS, C. H., KNACKSTEDT, M. A. & MECKE, K. R. 2004 Characterisation of irregular spatial
 1455 structures by parallel sets and integral geometric measures. *Colloids and Surfaces A:*
 1456 *Physicochemical and Engineering Aspects* **241** (1-3), 351–372.
- 1457 ASHGRIZ, N. 2011 *Handbook of atomization and sprays: theory and applications*. Springer Science
 1458 & Business Media.
- 1459 BATCHELOR, G. K. 1951 Pressure fluctuations in isotropic turbulence. In *Mathematical*
 1460 *Proceedings of the Cambridge Philosophical Society*, , vol. 47, pp. 359–374. Cambridge
 1461 University Press.
- 1462 BERRYMAN, J. G. 1987 Relationship between specific surface area and spatial correlation
 1463 functions for anisotropic porous media. *J Math Phys* **28** (1), 244–245.
- 1464 BLAKELEY, B. C., WANG, W. & RILEY, J. J. 2019 On the kinematics of scalar iso-surfaces in
 1465 decaying homogeneous, isotropic turbulence. *Journal of Turbulence* **20** (10), 661–680.

- 1466 BRAY, K. N. C. & MOSS, J. B. 1977 A unified statistical model of the premixed turbulent
1467 flame. *Acta Astronautica* **4** (3-4), 291–319.
- 1468 CANDEL, S. & POINSOT, T. 1990 Flame stretch and the balance equation for the flame area.
1469 *Combust. Sci. Technol.* **70** (1-3), 1–15.
- 1470 CATRAKIS, H. J. & DIMOTAKIS, P. E. 1996 Mixing in turbulent jets: scalar measures and
1471 isosurface geometry. *Journal of Fluid Mechanics* **317**, 369–406.
- 1472 CONSTANTIN, P. 1994a Geometric and analytic studies in turbulence. In *Trends and perspectives*
1473 *in applied mathematics*, pp. 21–54. Springer.
- 1474 CONSTANTIN, P. 1994b Geometric statistics in turbulence. *Siam Review* **36** (1), 73–98.
- 1475 CONSTANTIN, P., PROCACCIA, I. & SREENIVASAN, K. R. 1991 Fractal geometry of isoscalar
1476 surfaces in turbulence: theory and experiments. *Phys Rev Lett* **67** (13), 1739.
- 1477 DANAILA, L., ANTONIA, R. A. & BURATTINI, P. 2004 Progress in studying small-scale
1478 turbulence using exact two-point equations. *New J. Phys.* **6** (1), 128.
- 1479 DE GENNES, P.-G., BROCHARD-WYART, F. & QUÉRÉ, D. 2013 *Capillarity and wetting*
1480 *phenomena: drops, bubbles, pearls, waves*. Springer Science & Business Media.
- 1481 DI BATTISTA, R., BERMEJO-MORENO, I., MÉNARD, T., DE CHAISEMARTIN, S. & MASSOT, M.
1482 2019 Post-processing of two-phase DNS simulations exploiting geometrical features and
1483 topological invariants to extract flow statistics: application to canonical objects and the
1484 collision of two droplets. In *10th International Conference on Multiphase Flow, Rio de*
1485 *Janeiro, Brazil*.
- 1486 DIMOTAKIS, P. E. & CATRAKIS, H. J. 1999 Turbulence, fractals, and mixing. In *Mixing*, pp.
1487 59–143. Springer.
- 1488 DE DIVITIIS, N. 2014 Finite scale Lyapunov analysis of temperature fluctuations in homogeneous
1489 isotropic turbulence. *Applied Mathematical Modelling* **38** (21-22), 5279–5297.
- 1490 DE DIVITIIS, N. 2016 von Kármán–Howarth and Corrsin equations closure based on Lagrangian
1491 description of the fluid motion. *Annals of Physics* **368**, 296–309.
- 1492 DE DIVITIIS, N. 2020 von Kármán–Howarth and Corrsin equations closures through Liouville
1493 theorem. *Results in Physics* **16**, 102979.
- 1494 DONZIS, D. A., SREENIVASAN, K. R. & YEUNG, P. K. 2005 Scalar dissipation rate and
1495 dissipative anomaly in isotropic turbulence. *J. Fluid Mech.* **532**, 199–216.
- 1496 DREW, D. A. 1990 Evolution of geometric statistics. *SIAM Journal on Applied Mathematics*
1497 **50** (3), 649–666.
- 1498 DUMOUCHEL, C. 2008 On the experimental investigation on primary atomization of liquid
1499 streams. *Experiments in fluids* **45** (3), 371–422.
- 1500 DUMOUCHEL, C. & GROUT, S. 2009 Application of the scale entropy diffusion model to describe
1501 a liquid atomization process. *International journal of multiphase flow* **35** (10), 952–962.
- 1502 DUMOUCHEL, C., THIESSET, F. & MÉNARD, T. 2022 Morphology of contorted liquid structures.
1503 *International Journal of Multiphase flows* **152**, 104055.
- 1504 ELSAS, J. H., SZALAY, A. S. & MENEVEAU, C. 2018 Geometry and scaling laws of excursion
1505 and iso-sets of enstrophy and dissipation in isotropic turbulence. *Journal of Turbulence*
1506 **19** (4), 297–321.
- 1507 ESSADKI, M., DRUI, F., LARAT, A., MÉNARD, T. & MASSOT, M. 2019 Statistical modeling of
1508 the gas–liquid interface using geometrical variables: Toward a unified description of the
1509 disperse and separated phase flows. *Int. J. Multiphase Flow* **120**, 103084.
- 1510 ESWARAN, V. & POPE, S. B. 1988 An examination of forcing in direct numerical simulations
1511 of turbulence. *Computers & Fluids* **16** (3), 257–278.
- 1512 FEDERER, H. 1959 Curvature measures. *Transactions of the American Mathematical Society*
1513 **93** (3), 418–491.
- 1514 FRISCH, H. L. & STILLINGER, F. H. 1963 Contribution to the statistical geometric basis of
1515 radiation scattering. *J. Chem. Phys.* **38** (9), 2200–2207.
- 1516 GARCIA-RUIZ, J.-M., LOUIS, E., MEAKIN, P. & SANDER, L. M. 2012 *Growth patterns in*
1517 *physical sciences and biology*, vol. 304. Springer Science & Business Media.
- 1518 GAUDING, M., DANAILA, L. & VAREA, E. 2017 High-order structure functions for passive scalar
1519 fed by a mean gradient. *International Journal of Heat and Fluid Flow* **67**, 86–93.
- 1520 GAUDING, M., GOEBBERT, J. H., HASSE, C. & PETERS, N. 2015 Line segments in homogeneous
1521 scalar turbulence. *Physics of Fluids* **27** (9), 095102.
- 1522 GAUDING, M., WANG, L., GOEBBERT, J. H., BODE, M., DANAILA, L. & VAREA, E. 2019 On the

- 1523 self-similarity of line segments in decaying homogeneous isotropic turbulence. *Computers*
1524 *& Fluids* **180**, 206–217.
- 1525 GIANNAKOPOULOS, G. K., FROUZAKIS, C. E., MOHAN, S., TOMBOULIDES, A. G. & MATALON,
1526 M. 2019 Consumption and displacement speeds of stretched premixed flames-theory and
1527 simulations. *Combust. Flame* **208**, 164–181.
- 1528 GIBSON, C. H. 1968 Fine structure of scalar fields mixed by turbulence. i. zero-gradient points
1529 and minimal gradient. *The Physics of Fluids* **11** (11), 2305–2315.
- 1530 GIRIMAJI, S. S. & POPE, S. B. 1992 Propagating surfaces in isotropic turbulence. *Journal of*
1531 *Fluid Mechanics* **234**, 247–277.
- 1532 GOULDIN, F. C. 1987 An application of fractals to modeling premixed turbulent flames. *Combust*
1533 *Flame* **68** (3), 249–266.
- 1534 GOULDIN, F. C., HILTON, S. M. & LAMB, T. 1989 Experimental evaluation of the fractal
1535 geometry of flamelets. In *Symposium (International) on Combustion*, , vol. 22, pp. 541–
1536 550. Elsevier.
- 1537 GRAN, I. R., ECHEKKI, T. & CHEN, J. H. 1996 Negative flame speed in an unsteady 2-D
1538 premixed flame: A computational study. In *Symposium (International) on Combustion*,
1539 , vol. 26, pp. 323–329. Elsevier.
- 1540 GROSSMANN, S. & LOHSE, D. 1994 Fractal-dimension crossovers in turbulent passive scalar
1541 signals. *EPL (Europhysics Letters)* **27** (5), 347.
- 1542 GROUT, S., DUMOUCHEL, C., COUSIN, J. & NUGLISCH, H. 2007 Fractal analysis of atomizing
1543 liquid flows. *International Journal of Multiphase Flow* **33** (9), 1023–1044.
- 1544 HAWKES, E. R., CHATAKONDA, O., KOLLA, H., KERSTEIN, A. R. & CHEN, J. H. 2012 A
1545 petascale direct numerical simulation study of the modelling of flame wrinkling for large-
1546 eddy simulations in intense turbulence. *Combustion and flame* **159** (8), 2690–2703.
- 1547 HENTSCHEL, H. G. E. & PROCACCIA, I. 1984 Relative diffusion in turbulent media: the fractal
1548 dimension of clouds. *Physical Review A* **29** (3), 1461.
- 1549 HILL, R. J. 2002 Exact second-order structure-function relationships. *J. Fluid Mech.* **468**, 317–
1550 326.
- 1551 HIRT, C. W. & NICHOLS, B. D. 1981 Volume of fluid (VOF) method for the dynamics of free
1552 boundaries. *J Comput Phys* **39** (1), 201–225.
- 1553 HOU, T. Y. & LI, R. 2007 Computing nearly singular solutions using pseudo-spectral methods.
1554 *Journal of Computational Physics* **226** (1), 379–397.
- 1555 IYER, K. P., SCHUMACHER, J., SREENIVASAN, K. R. & YEUNG, P. K. 2020 Fractal iso-level
1556 sets in high-Reynolds-number scalar turbulence. *Physical Review Fluids* **5** (4), 044501.
- 1557 JAY, S., LACAS, F. & CANDEL, S. 2006 Combined surface density concepts for dense spray
1558 combustion. *Combustion and Flame* **144** (3), 558–577.
- 1559 KIRSTE, R. & POROD, G. 1962 Röntgenkleinwinkelstreuung an kolloiden systemen
1560 asymptotisches verhalten der streukurven. *Kolloid-Zeitschrift und Zeitschrift für*
1561 *Polymere* **184** (1), 1–7.
- 1562 KRUG, D., HOLZNER, M., LÜTHI, B., WOLF, M., KINZELBACH, W. & TSINOBER, A. 2015 The
1563 turbulent/non-turbulent interface in an inclined dense gravity current. *J. Fluid Mech.*
1564 **765**, 303–324.
- 1565 KRUG, D., HOLZNER, M., MARUSIC, I. & VAN REEUWIJK, M. 2017 Fractal scaling of the
1566 turbulence interface in gravity currents. *Journal of Fluid Mechanics* **820**.
- 1567 KULKARNI, T., BUTTAY, R., KASBAOUI, M. H., ATILI, A. & BISETTI, F. 2021 Reynolds
1568 number scaling of burning rates in spherical turbulent premixed flames. *J. Fluid Mech.*
1569 **906**.
- 1570 LE MOYNE, L., FREIRE, V. & QUEIROS-CONDÉ, D. 2008 Fractal dimension and scale entropy
1571 applications in a spray. *Chaos, Solitons & Fractals* **38** (3), 696–704.
- 1572 LEBAS, R., MENARD, T., BEAU, P-A., BERLEMONT, A. & DEMOULIN, F-X. 2009 Numerical
1573 simulation of primary break-up and atomization: Dns and modelling study. *International*
1574 *Journal of Multiphase Flow* **35** (3), 247–260.
- 1575 LIBBY, P. A. & BRAY, K. N. C. 1980 Implications of the laminar flamelet model in premixed
1576 turbulent combustion. *Combustion and Flame* **39** (1), 33–41.
- 1577 LIEPMANN, H. W. 1949 Die Anwendung eines Satzes über die Nullstellen stochastischer
1578 Funktionen auf Turbulenzmessungen. *Helvetica Physica Acta* **22** (2), 119–126.

- 1579 LISS, P. S. & JOHNSON, M. T. 2014 *Ocean-atmosphere interactions of gases and particles*.
1580 Springer Nature.
- 1581 LOVEJOY, S. 1982 Area-perimeter relation for rain and cloud areas. *Science* **216** (4542), 185–187.
- 1582 LU, J. & TRYGGVASON, G. 2018 Direct numerical simulations of multifluid flows in a vertical
1583 channel undergoing topology changes. *Physical Review Fluids* **3** (8), 084401.
- 1584 LU, J. & TRYGGVASON, G. 2019 Multifluid flows in a vertical channel undergoing topology
1585 changes: Effect of void fraction. *Physical Review Fluids* **4** (8), 084301.
- 1586 MA, Z. & TORQUATO, S. 2018 Precise algorithms to compute surface correlation functions of
1587 two-phase heterogeneous media and their applications. *Physical Review E* **98** (1), 013307.
- 1588 MANDELBROT, B. B. 1975 On the geometry of homogeneous turbulence, with stress on the
1589 fractal dimension of the iso-surfaces of scalars. *Journal of Fluid Mechanics* **72** (3), 401–
1590 416.
- 1591 MAZELLIER, N. & VASSILICOS, J. C. 2008 The turbulence dissipation constant is not universal
1592 because of its universal dependence on large-scale flow topology. *Phys. Fluids* **20** (1),
1593 015101.
- 1594 MÉNARD, T., TANGUY, S. & BERLEMONT, A. 2007 Coupling level set/VOF/ghost fluid
1595 methods: Validation and application to 3D simulation of the primary break-up of a liquid
1596 jet. *Int. J. Multiphase Flow* **33** (5), 510–524.
- 1597 MORÁN, J., FUENTES, A., LIU, F. & YON, J. 2019 FracVAL: An improved tunable algorithm
1598 of cluster-cluster aggregation for generation of fractal structures formed by polydisperse
1599 primary particles. *Computer Physics Communications* **239**, 225–237.
- 1600 PETERS, N. 1988 Laminar flamelet concepts in turbulent combustion. In *Symposium*
1601 *(International) on Combustion*, , vol. 21, pp. 1231–1250. Elsevier.
- 1602 PETERS, N. 1992 A spectral closure for premixed turbulent combustion in the flamelet regime.
1603 *Journal of Fluid Mechanics* **242**, 611–629.
- 1604 PETERS, N., TERHOEVEN, P., CHEN, J. H. & ECHEKKI, T. 1998 Statistics of flame
1605 displacement speeds from computations of 2-D unsteady methane-air flames. In
1606 *Symposium (International) on Combustion*, , vol. 27, pp. 833–839. Elsevier.
- 1607 POPE, S. B. 1988 The evolution of surfaces in turbulence. *Int J Eng Sci* **26** (5), 445–469.
- 1608 POPE, S. B., YEUNG, P. K. & GIRIMAJI, S. S. 1989 The curvature of material surfaces in
1609 isotropic turbulence. *Physics of Fluids* **1** (12), 2010–2018.
- 1610 SEATON, N. A. & GLANDT, E. D. 1986 Spatial correlation functions from computer simulations.
1611 *The Journal of chemical physics* **85** (9), 5262–5268.
- 1612 SHETE, K. P. & DE BRUYN KOPS, S. M. 2020 Area of scalar isosurfaces in homogeneous
1613 isotropic turbulence as a function of reynolds and schmidt numbers. *J. Fluid Mech.* **883**.
- 1614 DA SILVA, C. B., HUNT, J. C. R., EAMES, I. & WESTERWEEL, J. 2014 Interfacial layers between
1615 regions of different turbulence intensity. *Annu Rev Fluid Mech* **46**, 567–590.
- 1616 DE SILVA, C. M., PHILIP, J., CHAUHAN, K., MENEVEAU, C. & MARUSIC, I. 2013 Multiscale
1617 geometry and scaling of the turbulent-nonturbulent interface in high Reynolds number
1618 boundary layers. *Phys Rev Lett* **111** (4), 044501.
- 1619 SORENSEN, C. M. 2001 Light scattering by fractal aggregates: a review. *Aerosol Science &*
1620 *Technology* **35** (2), 648–687.
- 1621 SREENIVASAN, K. R. & MENEVEAU, C. 1986 The fractal facets of turbulence. *J. Fluid Mech.*
1622 **173**, 357–386.
- 1623 SREENIVASAN, K. R., PRABHU, A. & NARASIMHA, R. 1983 Zero-crossings in turbulent signals.
1624 *J. Fluid Mech.* **137**, 251–272.
- 1625 SREENIVASAN, K. R., RAMSHANKAR, R. & MENEVEAU, C. 1989 Mixing, entrainment and fractal
1626 dimensions of surfaces in turbulent flows. *Proceedings of the Royal Society of London. A.*
1627 *Mathematical and Physical Sciences* **421** (1860), 79–108.
- 1628 SUSSMAN, M., SMERKA, P. & OSHER, S. 1994 A level set approach for computing solutions
1629 to incompressible two-phase flow. *Journal of Computational physics* **114** (1), 146–159.
- 1630 TEUBNER, M. 1990 Scattering from two-phase random media. *The Journal of chemical physics*
1631 **92** (7), 4501 – 4507.
- 1632 THIESSET, F., DURET, B., MÉNARD, T., DUMOUCHEL, C., REVEILLON, J. & DEMOULIN, F.-X.
1633 2020 Liquid transport in scale space. *J. Fluid Mech.* **886**, A4.
- 1634 THIESSET, F., MAURICE, G., HALTER, F., MAZELLIER, N., CHAUVEAU, C. & GÖKALP, I. 2016a

- 1635 Geometrical properties of turbulent premixed flames and other corrugated interfaces.
1636 *Physical Review E* **93** (1), 013116.
- 1637 THIESSET, F., MAURICE, G., HALTER, F., MAZELLIER, N., CHAUVEAU, C. & GÖKALP, I. 2016b
1638 Modelling of the subgrid scale wrinkling factor for large eddy simulation of turbulent
1639 premixed combustion. *Combust. Theor. Model.* **20** (3), 393–409.
- 1640 THIESSET, F., MÉNARD, T. & DUMOUCHEL, C. 2021 Space-scale-time dynamics of liquidgas
1641 shear flow. *J. Fluid Mech.* **912**, A39.
- 1642 THIESSET, F. & POUX, A. 2020 Numerical assessment of the two-point statistical equations
1643 in liquid/gas flows. *Tech. Rep.*. CNRS, Normandy Univ., UNIROUEN, INSA Rouen,
1644 CORIA. Available at <https://hal.archives-ouvertes.fr/hal-02614565>.
- 1645 THIESSET, F., SCHAEFFER, V., DJENIDI, L. & ANTONIA, R. A. 2014 On self-preservation and
1646 log-similarity in a slightly heated axisymmetric mixing layer. *Physics of Fluids* **26** (7),
1647 075106.
- 1648 TORQUATO, S. 2002 *Random Heterogeneous Materials. Microstructure and Macroscopic*
1649 *Properties*. Springer-Verlag New York.
- 1650 TROUVÉ, A. & POINSOT, T. 1994 The evolution equation for the flame surface density in
1651 turbulent premixed combustion. *J. Fluid Mech.* **278**, 1–31.
- 1652 VASSILICOS, J. C. 1992 The multispiral model of turbulence and intermittency. In *Topological*
1653 *aspects of the dynamics of fluids and plasmas* (ed. H. K. Moffatt, G. M. Zaslavsky,
1654 P. Comte & M. Tabor), pp. 427–442. Springer.
- 1655 VASSILICOS, J. C. & HUNT, J. C. R. 1991 Fractal dimensions and spectra of interfaces
1656 with application to turbulence. *Proceedings of the Royal Society of London. Series A:*
1657 *Mathematical and Physical Sciences* **435** (1895), 505–534.
- 1658 VASSILICOS, J. C. & HUNT, J. C. R. 1996 Moving surfaces in turbulent flows. In *INSTITUTE*
1659 *OF MATHEMATICS AND ITS APPLICATIONS CONFERENCE SERIES*, , vol. 56,
1660 pp. 127–154. Oxford University Press.
- 1661 VILLERMAUX, E. & GAGNE, Y. 1994 Line dispersion in homogeneous turbulence: stretching,
1662 fractal dimensions, and micromixing. *Phys Rev Lett* **73** (2), 252.
- 1663 YEUNG, P. K., GIRIMAJI, S. S. & POPE, S. B. 1990 Straining and scalar dissipation on material
1664 surfaces in turbulence: implications for flamelets. *Combustion and flame* **79** (3-4), 340–
1665 365.
- 1666 YON, J., MORÁN, J., OUF, F-X., MAZUR, M. & MITCHELL, J. B. 2021 From monomers
1667 to agglomerates: A generalized model for characterizing the morphology of fractal-like
1668 clusters. *Journal of Aerosol Science* **151**, 105628.
- 1669 YU, R., NILSSON, T., FUREBY, C. & LIPATNIKOV, A. N. 2021 Evolution equations for the
1670 decomposed components of displacement speed in a reactive scalar field. *J. Fluid Mech.*
1671 **911**.